The Wave Function of the Nucleon and its Excited States

THE UNIVERSITY
of ADELAIDE

Dale S. Roberts

School of Chemistry and Physics

The University of Adelaide

A thesis submitted for the degree of

Doctor of Philosophy

May 2014

To Mark

Acknowledgements

I sit here staring at a blank page, struggling to find the words to condense the incredible amount of support I've received from friends and family over the last 5 years into a reasonable amount of space. To say 'I couldn't have done it without you all' is an understatement, I wouldn't have thought getting this far was even possible.

Thanks go to my parents for encouraging me into science, making education a priority from very early on, and instilling a drive to succeed, and thanks to Louise for being a generally awesome little sister. Derek and Waseem, you've been the best, most patient supervisors I could have asked for, your guidance, as well as everything you've taught me has been invaluable.

I had a wonderful group of friends supporting me throughout the last few years. Cael, thanks for our many hours of discussions about anything and everything, I'm entirely convinced that you and I could solve all the world's problems over a couple of beers. Lewis, I tried very hard to keep up with you when we discussed your work, but most of the time, I'll admit, it was going over my head, but when it wasn't, I learned a lot. Andrew, your off-beat yet razor-sharp sense of humour kept me guessing, and provided some useful tips on new ways to interact with my couch. Ben, I wish more of your programming tips sunk in, they'd come in handy nowadays. And Thom, thanks for many productive Lattice QCD discussions and for not murdering me. Thanks also to everyone else for being pretty great people to work around.

Thanks to everyone at the NCI National Facility, firstly for providing the compute systems that I could not have done this work without, and then hiring me before I was even finished. Thanks to Leaf, Grant,

Ben and Andrey for constantly pestering me to get my thesis done and to Margaret and Roger for giving me the incentive and time during business hours to actually finish it off. Special thanks to Muhammad for reminding me whenever possible, with my unofficial title of 'Not-Dr.' Roberts.

And last but by no means least, Samantha, your unshakable faith that I was able to do this, and your unending support made this all possible. Without you I wouldn't have made it this far, I love you more than any words I know can express it.

So, Belgian at 5, anyone?

Abstract

In this thesis, we detail the techniques required to perform general lattice QCD calculations. Specifically, we introduce the method by which the continuum theory of quarks and gluons, Quantum Chromodynamics is discretised in order to be solved numerically. We describe the distinct methods by which the discrete actions for the gauge and fermion fields given by naively applying a finite-difference approximation to the continuum theory can be improved, going some way to remove the systematic errors of discretisation. The background field method for placing electromagnetic fields onto a discrete lattice is also introduced.

Techniques required for the calculation of wave functions are then introduced, beginning with the two-point function, which is fundamental in extracting properties of hadrons from the lattice. The variational method, which allows access to the excited states of particles is then introduced. The wave function is then constructed from the two-point function, which forms the basis of the most significant results of this thesis. We also introduce gauge fixing, made necessary by the gauge dependent nature of wave function operators.

The smeared operators used in the construction of these two-point functions are evaluated, by way of two measures designed to measure the coupling strength of these operators to states with a variety of momenta. Of particular interest is the extent to which strong overlap can be obtained with individual high-momentum states. This is vital to exploring hadronic structure at high momentum transfers on the lattice and addressing interesting phenomena observed experimentally. We consider a novel idea of altering the shape of the smeared operator to match the Lorentz contraction of the probability distribution of the high-momentum state, and show a reduction in the relative error of

the two-point function by employing this technique. Our most important finding is that the overlap of the states becomes very sharp in the smearing parameters at high momenta and fine tuning is required to ensure strong overlap with these states.

Making use of the background field methods and the wave functions constructed from the two-point functions, we calculate the probability distributions of quarks in the ground state of the proton, and how they are affected in the presence of a constant background magnetic field. We focus on wave functions in the Landau and Coulomb gauges using the quenched approximation of QCD. We observe the formation of a scalar $u - d$ diquark clustering. The overall distortion of the quark probability distribution under a very large magnetic field, as demanded by the quantisation conditions on the field, is quite small. The effect is to elongate the distributions along the external field axis while localizing the remainder of the distribution. Using optimised smearing parameters calculated from the methods detailed in this thesis, we construct wave functions of high-momentum states, and are able to qualitatively observe high momentum states. We find that, at very high momenta, artefacts are present caused by the poor overlap of these states to the interpolating operators. Careful tuning of the smearing parameters is shown to reduce these artefacts, reinforcing results presented earlier in the thesis.

The culmination of the techniques introduced and the results obtained in this thesis is the application of the eigenvectors from a variational analysis to successfully extract the wave functions of even-parity excited states of the nucleon, including the Roper, in full QCD. We explore the first four states in the spectrum excited by the standard nucleon interpolating field. We find that the states exhibit a structure qualitatively consistent with a constituent quark model, where the ground, first-, second- and third-excited states have 0, 1, 2, and 3 nodes in the radial wave function of the d-quark about two u quarks at the origin. Moreover the radial amplitude of the probability distribution is similar to that predicted by constituent quark models. We present a detailed examination of the quark-mass dependence of

the probability distributions for these states, searching for a nontrivial role for the multi-particle components mixed in the finite-volume QCD eigenstates. Finally we examine the dependence of the d-quark probability distribution on the positions of the two u quarks. The results are fascinating, with the underlying S-wave orbitals governing the distributions even at rather large u-quark separations.

Statement of Originality

This work contains no material which has been accepted for the award of any other degree or diploma in any university or other tertiary institution to Dale Roberts and, to the best of my knowledge and belief, contains no material previously published or written by another person, except where due reference has been made in the text.

I give consent to this copy of my thesis, when deposited in the University Library, being made available for loan and photocopying, subject to the provisions of the Copyright Act 1968. I also give permission for the digital version of my thesis to be made available on the web, via the University's digital research repository, the Library catalogue, and also through web search engines, unless permission has been granted by the University to restrict access for a period of time.

Contents

List of Figures

LIST OF FIGURES

Chapter 1

Introduction

The standard model of particle physics has enjoyed vast success as a theory that describes three of the four fundamental forces of Nature. The most accurate quantity known is the anomalous magnetic moment of the electron, with theoretical calculations matching experimental data to 11 significant figures. Further success came with the unification of the electromagnetic and weak forces, predicting a weak neutral current mediated by the (at the time) undiscovered Z boson and bringing spontaneous symmetry breaking through the recently discovered Higgs boson to generate its mass.

Not all aspects of the standard model enjoy the same level of precision. Quantum Chromodynamics (QCD) remains as a notoriously difficult theory to analyse, due to its resistance to perturbative techniques. Though effective models have been considered in the past, no single model has been able to encapsulate all of the aspects.

Lattice QCD provides a first principles approach to QCD and is complementary to perturbative techniques. For decades, Lattice QCD has provided a robust framework for the calculations of a variety of hadron phenomena, including, but certainly not limited to spectra, transitional and electromagnetic form factors and electric and magnetic moments and polarisabilities, to name a few highlights of local interest. In the last few years, techniques have been developed and refined to allow access to higher energy hadron excitations, such as the Roper resonance, for the first time. Accurate calculation of resonance properties is an active area of Lattice QCD.

In the past, Lattice QCD has been limited to quarks with a much heavier

mass than the known up and down quark masses, as well as being limited to small lattice sizes due to the inherit computational complexity of the theory. However, with the exceptional advances in the capabilities of modern supercomputers, combined with algorithms of ever increasing efficiency, these limitations are on the verge of being removed.

An examination of the wave function of a quark bound within a hadron provides deep insights into the underlying dynamics of the many-body theory of QCD. It enables a few-body projection of the underlying physics that can be connected with models, shedding light on the essential effective phenomena emerging from the complex dynamics of QCD.

In spite of the great success of Lattice QCD to this date, there remain aspects of the approach that cause systematic errors in the calculations. First and foremost, the restriction of a particle to a small, finite region of spacetime, can, if the region is not sufficiently large, cause unphysical aberrations to the result. Finite volume effects can be studied directly using multiple lattice volumes, which may be computationally prohibitive, or inferred indirectly from data, which may be inconclusive. Another way to study finite volume effects is a direct visualisation of the state, which is relatively computationally inexpensive and presents these effects clearly.

The ability to analyse high momentum states on the lattice is quite limited, as these states tend to decay quickly in Euclidean time, thus limiting any potential calculations that could be performed. We present new methods to determine how effectively a high momentum state can be created on the lattice, and propose a method of operator selection to ensure maximal overlap with the created state. Wave function techniques can be employed in conjunction with these techniques to observe Lorentz contraction on the lattice and assess the efficacy of the chosen operators.

The electromagnetic properties of hadrons can be investigated on the lattice by directly implementing a Lattice version of an external magnetic field in conjunction with the QCD fields. Though a seemingly ideal method of determining quantities such as magnetic moments and polarisabilities, the formulation of the theory in a finite volume leads to a quantisation of the magnetic field strength resulting in very strong magnetic fields. The induced fields are so strong that the energy imparted to the particle can be as high as a third again the particles

mass. The key concern is that a field of such magnitude could so drastically effect a particle that it would bear little resemblance to its zero field form. In this regard, wave function techniques serve as an ideal tool to investigate the distortion of a hadron due to large magnetic fields.

Many models of QCD attempt to calculate the wave function of the excited states of hadrons, though none can claim to offer a true description. Though excited state spectroscopy in Lattice QCD is a well studied field, success in obtaining low-lying excited states has only been achieved recently. As such, the techniques and technology required to calculate the wave function of the Roper resonance have just been developed. For the first time, it is possible to calculate, from first principles, the wave functions of both the ground state and excited states of the proton at the physical quark mass.

In this thesis, we will explore each of these issues related to the wave functions describing the distribution of quarks within hadrons. In Chapter 2, we discuss the general aspects of lattice QCD common to most studies performed today, and the background magnetic field method, both essential to this study. In Chapter 3 we discuss the techniques of lattice QCD that are required specifically to investigate two point functions, excited states of the nucleon and wave functions. Chapter 5 addresses the wave functions of the nucleon in strong magnetic fields, and at high momentum using the methods developed in Chapter 4. Finally, in Chapter 6, we investigate the wave functions of excited states of the nucleon.

Chapter 2

Lattice QCD

In the late 1940's and early 1950's, detailed analysis of cosmic ray data provided theorists a wealth of previously undiscovered particles whose decay properties could not be explained by current theory. The kaon was the first of these particles discovered, it had a lifetime on the order of 10^{-10} seconds, which is significantly longer than other decay products of pion-nucleon reactions. Furthermore, this particle appeared to conserve parity on creation only to violate parity on decay. Since the cause of both of these irregularities was unknown, the kaon was declared to have 'strangeness'.

The first particle heavier than the nucleon discovered with an unusually long lifetime was the Lambda particle, observed in cosmic rays and dubbed to also have this strangeness property. A second long lived particle that decayed in two stages, first to a Lambda, emitting a pion, and then to a nucleon, also emitting a pion, was discovered five years later and dubbed the Cascade, due to its multi-stage decay.

The discovery of these particles prompted the formulation of a classification system, based around the idea that these new mesons and baryons were not fundamental particles, but composed of three kinds of hitherto undiscovered elementary particles. These particles, known as quarks, were arranged according to irreducible representations of an $SU(3)$ flavour symmetry, with the spin-$\frac{1}{2}$ baryons forming the members of an 8 dimensional representation, known as the octet, and the spin-$\frac{3}{2}$ baryons forming a 10 dimensional representation, known as the decuplet. Strangeness was accounted for by the one of these quarks, known as the strange quark, which decayed via the weak interaction to either an up or a

down quark. At the time of this formulation, early particle accelerators, as well as further analysis of cosmic ray data, all but one member of the decuplet had been observed. This missing particle, named the Ω^- particle, was predicted to be composed composed of three strange quarks. On the discovery of this particle, the $SU(3)$ flavour symmetry model became the most popular description of hadron structure.

Other particles with unusual properties were beginning to be discovered in early particle accelerator experiments. A P_{11} resonance of the Proton was discovered with a mass of 1440 MeV, as well as the lowest S_{11} resonance, with a mass some 95 MeV higher. Furthermore, the Δ^{++}, a spin $\frac{3}{2}$ particle composed of three up quarks with aligned spins and zero orbital angular momentum seemed to violate the Pauli Exclusion principle. This was provided as evidence for new underlying symmetry with at least three degrees of freedom. A second $SU(3)$ symmetry was proposed, this time in analogy with the formulation of invariance to a local phase in electrodynamics. The quarks were placed in the fundamental representation of $SU(3)$, and thus demanded to be invariant under local $SU(3)$ transformations. This analogous new charge, known as 'colour', gives rise to the notion of eight species of gluons, the gauge boson of the strong force, in the adjoint representation of $SU(3)$. These are the underpinnings of the strong sector of the Standard Model, known as Quantum Chromodynamics (QCD).

Much like Quantum Electrodynamics, QCD is defined in terms of the action of interacting fermion (quark) and gauge boson (gluon) fields. This action is given by

$$S_{QCD} = \int d^4x \Big(-\frac{1}{4} F^a_{\mu\nu}(x) F^{a\mu\nu} + \sum_q \bar{\psi}^i_q(x)(i\gamma^\mu D_\mu(x) - m_q)_{ij}\psi^j_q(x) \Big), \quad (2.1)$$

where i, j are indices in the fundamental representation of $SU(3)$, and a is an index in the adjoint representation. The sum over q denotes a sum over quark flavours. The $SU(3)$ field-strength tensor and covariant derivative are given by,

$$\begin{aligned} F^a_{\mu\nu}(x) &= \partial_\mu A^a_\nu(x) - \partial_\nu A^a_\mu(x) + g_s f_{abc} A^b_\mu(x) A^c_\nu(x), \\ (D_\mu(x))_{ij} &= \delta_{ij}\partial_\mu - i g_s \sum_a \frac{\lambda^a_{ij}}{2} A^a_\mu(x), \end{aligned} \quad (2.2)$$

where g_s is the QCD coupling constant, f_{abc} are the fully antisymmetric structure

constants of the $SU(3)$ group and the λ_{ij}^a are the Gell-Mann matricies. From this, we can see that the $F_{\mu\nu}F^{\mu\nu}$ term will lead to three and four gluon vertices, *i.e.* the gluons interact with themselves. It is this that gives rise to asymptotic freedom, where, at short distance, the effective coupling reduces and the theory can be calculated perturbatively. At low energy, however one must resort to non-perturbative methods to obtain meaningful results.

Lattice QCD is the pre-eminent method of solving low energy QCD non-perturbitavely. The key principle behind constructing a field theory on the lattice is the reformulation of the theory on to a discrete spacetime. In order to accomplish this, we begin by allowing fermions to occupy the sites on a four dimensional hypercubic grid. The choice of a hypercubic lattice means that the theory will no longer be completely rotationally symmetric. Only hypercubic rotational symmetry remains; that is, symmetry under rotations of $\frac{\pi}{2}$ around any axis. The spacing between each site, a, is a product of the choice of gluon coupling strength, and therefore is not chosen directly. The lattice spacing acts as a regulator and thus provides a cut off to the physical momentum allowed. This cut off is

$$p_{\max} = \frac{\pi}{a}. \tag{2.3}$$

Since our intent is to evaluate the theory computationally, we can process only a finite amount of sites. Conventionally, the number of sites in each spatial dimension, N_S will be the same[1], and the number of sites in the time dimension, N_T, will be greater than or equal to N_S[2], thus giving a physical lattice size of $a^3 N_S^3 \times a N_T \equiv L^3 \times T$.[3]

It is important to consider the boundaries of the lattice. The best finite approximation to an infinite region is to employ periodic boundary conditions, *i.e.*

$$\psi(N_S + 1) = \psi(1) \tag{2.4}$$

This means that a particle on the lattice sees an infinite set of copies a distance N_S apart. Should the wave function of the particle be compact enough, this

[1] Older studies considered a single larger spatial dimension to compensate for an inability to compute 3 large spatial dimensions. Such techniques are largely obsolete

[2] In the case of finite temperature Lattice QCD, $N_T \ll N_S$, though that is not relevant to this thesis.

[3] Some recent studies have considered a different lattice spacing in the time dimension than the spatial dimensions, we, however, do not.

is not a problem. However, should the wave function have non-trivial weight at large distances, the particle will affect itself through the periodic boundary. The general guideline is $m_\pi L > 3$, though this does not guarantee a state free of finite volume effects. This condition also gives a lower limit on the lattice spacing, as if a is too small, there are a number of numerical issues that arise, such as auto-correlation times and computational cost. This gives rise to a set of $N_S + 1$ allowable vibrational modes in each spatial dimension, thus giving rise to discretised momentum given by

$$p_i = \frac{2\pi n_i}{L}, \tag{2.5}$$

where[1] $n_i \in \mathbb{Z}^3$ and $-\frac{N_S}{2} < n_i \leq \frac{N_S}{2}$.

In the time direction, periodic boundary conditions are employed for the gauge links and fixed boundaries are generally employed for quarks, that is quarks are not allowed to cross the boundary, which avoids the problem of backward propagating states. Due to there generally being more lattice sites in the time direction, the solution to avoiding finite size problems in the time dimension is to simply examine away from the boundary.

As the fermion fields carry colour degrees of freedom, we must define some way to parallel transport the colour information between the lattice sites. For this reason, we reformulate the gauge degrees of freedom from the 4-vector potential, $A^{ab}_\mu(x)$, to the Wilson lines defined along each axis between two nearest neighbour lattice sites, called gauge links and given by

$$U^{ab}_\mu(x) = \exp\big(ig \int_0^1 dt A^{ab}_\mu(x + ta\hat{\mu})\big), \tag{2.6}$$

and shown in Fig. 2.1. Due to the gauge transformation properties of the fermion fields and the gauge links,

[1] By introducing a phase on the boundary, it is possible to add a small constant to the momentum, at the cost of the zero momentum state. This technique, known as 'twisting' the boundary conditions, is generally used to study hadrons at low momentum transfer. In this thesis, we will only be considering large momentum transfer and thus will not be making use of this technique.

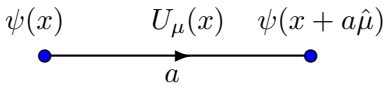

Figure 2.1: The gauge link between two lattice sites.

$$\begin{aligned}
\psi(x) &\to G(x)\psi(x) \\
\bar{\psi}(x) &\to \bar{\psi}(x)G^\dagger(x) \\
U_\mu(x) &\to G(x)U_\mu(x)G^\dagger(x+\mu),
\end{aligned} \tag{2.7}$$

we can see that gauge covariant quantities will be generally be composed of an ordered path of gauge links terminated by a fermion and anti fermion pair.

Since we are no longer working with a continuous spacetime, we must fall back to finite difference approximations to the derivative. We first define the forward and backward derivatives.

$$\begin{aligned}
\overrightarrow{\partial_\mu} F(x) &= \frac{F(x+\hat{\mu}) - F(x)}{a} \\
\overleftarrow{\partial_\mu} F(x) &= \frac{F(x) - F(x-\hat{\mu})}{a},
\end{aligned} \tag{2.8}$$

and their equivalent covariant derivatives

$$\begin{aligned}
\overrightarrow{D_\mu} F(x) &= \frac{1}{a}\big(U_\mu(x)F(x+\hat{\mu}) - F(x)\big) \\
\overleftarrow{D_\mu} F(x) &= \frac{1}{a}\big(F(x) - U_\mu^\dagger(x-\hat{\mu})F(x-\hat{\mu})\big),
\end{aligned} \tag{2.9}$$

Since we require gauge invariance and hermiticity, we need to define a symmetric, covariant derivative

$$\begin{aligned}
\nabla_\mu F(x) &= (\overrightarrow{D_\mu} - \overleftarrow{D_\mu})F(x) \\
&= \frac{1}{2a}\big(U_\mu(x)F(x+\hat{\mu}) - U_\mu^\dagger(x-\hat{\mu})F(x-\hat{\mu})\big).
\end{aligned} \tag{2.10}$$

Integration must also be approximated by a sum

$$\int_V d^4x F(x) = a^4 \sum_x F(x), \tag{2.11}$$

Since the lattice is blind to its own spacing, all quantities calculated are scaled to dimensionless lattice variables by powers of the lattice spacing

$$\begin{aligned} m &\to ma \\ \psi &\to a^{\frac{3}{2}}\psi \\ p_\mu &\to p_\mu a. \end{aligned} \tag{2.12}$$

Quantities on the lattice are calculated by first constructing configurations of gauge links through a Markov-chain process using a discrete version of the full QCD Yang-Mills and fermion actions, or, in the case of the quenched approximation, the Yang-Mills action alone. One then generates valence quark propagators on each configuration and these propagators are then combined via interpolating operators to construct the two-point Greens functions of the particle of interest. An excellent review of these details can be found in the textbook [1].

2.1 Gauge Fields

Wilson originally considered a formulation for the gauge action that satisfied lattice versions of the continuum symmetries that the Yang-Mills action respects, namely

- The action must be translationally invariant, and therefore must contain a sum over all lattice sites.
- The action must be gauge invariant, and therefore must be constructed from closed loops.
- The action must be rotationally symmetric, so must be invariant under rotations of $\frac{\pi}{2}$.
- The action must be local, therefore the action for each gauge link must be constructed from loops containing that link.

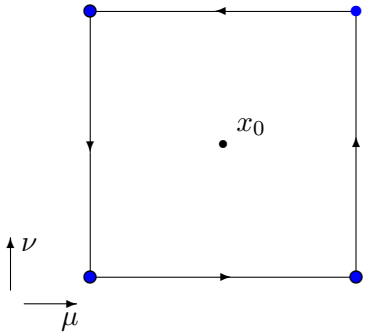

Figure 2.2: The plaquette defined about its centre

A further condition specific to lattice actions is that the action must reduce to its continuum form as $a \to 0$.

Wilson [2] initially constructed the gluon action from the smallest possible loop able to be constructed on the lattice, the 1×1 plaquette. When calculating the action, one writes the gauge links used to construct the plaquette relative to its centre, then sums the plaquettes in each plane containing that point. The plaquette in the $\mu\nu$ plane, shown in Fig. 2.2 is given by

$$\begin{aligned} P_{\mu\nu} = \exp\big(ig \int_{-a/2}^{a/2} dt A_\mu(x_0 - \frac{a\hat{\nu}}{2} + t\hat{\mu})\big)\exp\big(ig \int_{-a/2}^{a/2} dt A_\nu(x_0 + \frac{a\hat{\mu}}{2} + t\hat{\nu})\big) \\ \times \exp\big(-ig \int_{-a/2}^{a/2} dt A_\mu(x_0 + \frac{a\hat{\nu}}{2} + t\hat{\mu})\big)\exp\big(-ig \int_{-a/2}^{a/2} dt A_\nu(x_0 - \frac{a\hat{\mu}}{2} + t\hat{\nu})\big). \end{aligned} \tag{2.13}$$

Assuming sufficiently smooth gauge fields, one can approximate the integral in the exponential as

$$\exp\big(ig \int_{-a/2}^{a/2} dt A_\alpha(x + t\hat{\alpha})\big) \approx \exp\big(igaA_\alpha(x)\big) \tag{2.14}$$

Rewriting the plaquette in terms of these smooth fields gives,

$$\begin{aligned} P_{\mu\nu} = \exp\big(igaA_\mu(x_0 - \frac{a\hat{\nu}}{2})\big)\exp\big(igaA_\nu(x_0 + \frac{a\hat{\mu}}{2})\big) \\ \times \exp\big(-igaA_\mu(x_0 + \frac{a\hat{\nu}}{2})\big)\exp\big(-igaA_\nu(x_0 - \frac{a\hat{\mu}}{2})\big). \end{aligned} \tag{2.15}$$

Taylor expanding each of the A_α in Eq. (2.15) around x_0 to $\mathcal{O}(a^2)$, then collating the four exponentials into a single exponential using the Baker-Campbell-

Hausdorff identity gives,

$$\begin{aligned} P_{\mu\nu} &= \exp\big(iga^2(\partial_\mu A_\nu(x_0) - \partial_\nu A_\mu(x_0) + ig[A_\mu(x_0), A_\nu(x_0)]\big) \\ &= \exp\big(iga^2 F_{\mu\nu} + \mathcal{O}(a^4 g^2) + \mathcal{O}(a^3 g^3)\big), \end{aligned} \tag{2.16}$$

where the $\mathcal{O}(a^4 g^2)$ terms come from the higher order terms of the Taylor expansion of the gauge links, and the $\mathcal{O}(a^3 g^3)$ terms arise from higher order Baker-Campbell-Hausdorff terms. Taylor expanding this to second order gives.

$$P_{\mu\nu} = \mathbb{I} + iga^2 F_{\mu\nu} - \frac{g^2 a^4}{2} F_{\mu\nu} F^{\mu\nu} + \dots \tag{2.17}$$

Therefore, the discrete action that matches the continuum action to $\mathcal{O}(a^4 g^2)$, known as the Wilson gauge action, is given by

$$S_W = \beta \sum_x \sum_{\mu,\nu} \big(1 - \frac{1}{3} \mathrm{Re}\,\mathrm{tr} P_{\mu\nu}(x)\big), \tag{2.18}$$

where $\beta = \frac{6}{g^2}$. As β is a function of the coupling, g, it is this parameter that is responsible for determining the lattice spacing. The most common method used to determine the lattice spacing, outlined by Sommer [3], involves determining the force between two static (*i.e.* infinitely heavy) valence quarks, $F(r)$ at a particular value $r_0(c)$, such that

$$r_0(c)^2 F(r_0(c)) = c, \tag{2.19}$$

where $c = 1.65$, which gives a physical distance of $r_0 = 0.49\,\mathrm{fm}$ and determines the lattice spacing.

We can see that attempting to account for terms to higher powers of a or g quickly leads to a prohibitive amount of terms to compute by hand. Several techniques, apart from employing a symbolic manipulation program, can be used to deal with this problem. Lepage [4] proposed working in co-ordinate gauge, that is $x \cdot A_\mu(x) = 0$, thus causing the covariant derivative to become abelian when multiplied by x, then employing Stokes' theorem for the loops. Luscher and Weisz [5] proposed a gauge such that, in the $\mu\nu$ plane, $A_\mu(x) = 0$ for all x and $A_\nu(x) = 0$ for all x with $x_\mu = 0$, and considering $P_{\mu\nu}(0)$. Both methods arrive at the same result for the $\mathcal{O}(a^4 g^2)$ term in the exponential expansion of

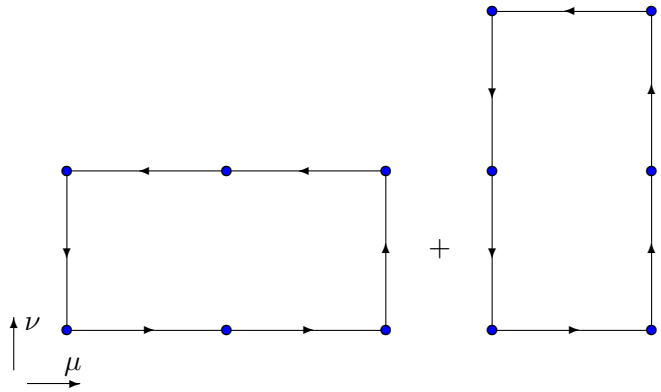

Figure 2.3: $R_{\mu\nu}$ from Eq. (2.21) (left) and $R_{\nu\mu}$ From Eq. (2.22) (right) used to construct the improved actions.

the plaquette.

$$P_{\mu\nu} = \exp\big(ig(a^2 F_{\mu\nu} + \frac{a^4}{24}(D_\mu^2 + D_\nu^2)F_{\mu\nu})\big). \tag{2.20}$$

Symanzik [6, 7] outlined a method to remove tree-level $\mathcal{O}(a^n)$ corrections to a discrete action by including $(4+n)$ link operators to the action. Weisz and Wohlert [8, 9] employed this method to improve the Wilson gauge action to $\mathcal{O}(a^4)$ by considering 6 link rectangular loops in the $\mu\nu$ plane, shown in Fig. 2.3. Following a similar procedure to that outlined earlier, we find that

$$R_{\mu\nu} = \exp\big(ig(2a^2 F_{\mu\nu} + \frac{a^4}{6}(4D_\mu + D_\nu)F_{\mu\nu})\big), \tag{2.21}$$

and similarly for $R_{\nu\mu}$,

$$R_{\nu\mu} = \exp\big(ig(2a^2 F_{\mu\nu} + \frac{a^4}{6}(D_\mu + 4D_\nu)F_{\mu\nu})\big). \tag{2.22}$$

The contribution of these rectangular loops to the action will take the form,

$$\delta_{xy} = 2 - \frac{1}{3}\mathrm{Re\,tr}\,(R_{\mu\nu} + R_{\nu\mu}) = \frac{g^2}{6}\big(8a^4 F_{\mu\nu}F^{\mu\nu} + \frac{5a^6}{12}F_{\mu\nu}(D_\mu + D_\nu)F_{\mu\nu}\big), \tag{2.23}$$

and the Symanzik improved action then becomes,

$$S_S = \sum_x \sum_{\mu,\nu} \frac{5\beta}{3}\Big(1 - \frac{1}{3}\mathrm{Re\,tr}(P_{\mu\nu}(x)) - \frac{1}{20}\big(2 - \frac{1}{3}\mathrm{Re\,tr}\,(R_{\mu\nu}(x) + R_{\nu\mu}(x))\big)\Big). \tag{2.24}$$

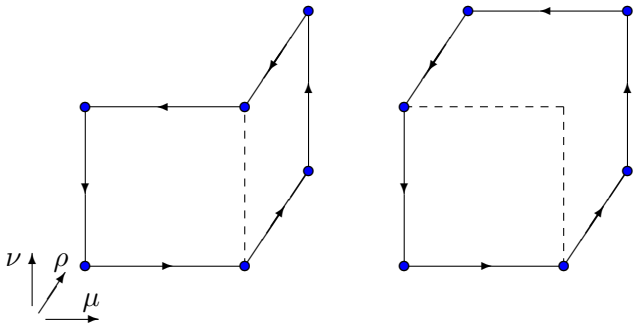

Figure 2.4: The remaining 6-link objects considered by Luscher and Weisz

Luscher and Weisz [5] proposed further improvements to this action by considering the two remaining kinds of 6 link loops shown in Fig. 2.4. They proposed removal of higher loop order artefacts by considering improvement of any general on shell quantity to higher gluon loop orders, and showed that the action calculated by Weisz following Symanzik's improvement program was a member of a larger set of actions. However, they also showed that the contribution from any of the non-planar loops to these on-shell quantities was small enough that Weisz's action is a sufficiently good approximation to the one-loop result.

Further improvement can be made to the gauge action by considering the Taylor expansion of the links themselves,

$$U_\mu(x) = 1 + igaA_\mu(x) - \frac{g^2a^2}{2}A_\mu^2(x) - \frac{ig^3a^3}{6}A_\mu^3(x) + \mathcal{O}(a^4). \tag{2.25}$$

The term proportional to $A_\mu^2(x)$ gives rise to unphysical tadpole contributions, which, though appearing to be suppressed by a^2, are suppressed only by the coupling, g^2. This is due to the fact that the integral around the loop constructed by the tadpole diagram is divergent, and, due to the momentum cut off on the lattice, will cancel the a^2 from the Taylor expansion. Lepage [10] proposed that these contributions exist primarily in the high energy, short distance, regime. The gauge link can be considered to be composed of high energy (UV) and low energy (IR) parts,

$$U_\mu(x) = \exp\big(ig\int dtA_\mu^{UV}(x+t\mu) + ig\int dtA_\mu^{IR}(x+t\mu)\big). \tag{2.26}$$

The integral over the high energy part can then be approximated across the entire lattice by the average value of the link determined in a gauge invariant way, the mean link, given by,

$$u_0 = \big(\sum_x \frac{1}{3}\mathrm{tr}P_{\mu\nu}(x)\big)^{\frac{1}{4}}. \tag{2.27}$$

By making the substitution,

$$U_\mu(x) \to \tilde{U}_\mu(x) = \frac{U_\mu(x)}{u_0}, \tag{2.28}$$

the majority of the tadpole contributions are removed from the gauge fields and the Mean Field Improved Symanzik action becomes,

$$\begin{aligned} S_{MFI} = &\frac{5\tilde{\beta}}{3}\sum_x\sum_{\mu,\nu}\Big(1 - \frac{1}{3}\mathrm{Re\,tr}\big(P_{\mu\nu}(x)\big)\Big) \\ &- \frac{\tilde{\beta}}{12u_0^2}\sum_x\sum_{\mu,\nu}\Big(2 - \frac{1}{3}\mathrm{Re\,tr}\left(R_{\mu\nu}(x) + R_{\nu\mu}(x)\right)\Big), \end{aligned} \tag{2.29}$$

where,

$$\tilde{\beta} = \frac{6}{g^2u_0^4}. \tag{2.30}$$

We note that, as $u_0 < 1$, this leads to an increase in the coefficient of the rectangle term, indicating that, to remove short distance fluctuations, contributions from more distant links should be considered. Iwasaki [11, 12] proposed using the renormalisation group approach to formulate a similar improvement to Wilson's action by considering the form

$$S_I = \beta\sum_x\sum_{\mu,\nu}(1 - 8c_0P_{\mu\nu}) + c_0(R_{\mu\nu} + R_{\mu\nu}), \tag{2.31}$$

where the coefficient c_0 was determined to be $c_0 = -0.331$. In this action, β has been rescaled by a factor of $\frac{1}{3.648}$ from the Wilson action. We note that, in this action, the contribution from the rectangular terms is also enhanced relative to the Symanzik action.

In an ideal world, we would be able to sample every possible vacuum configuration, however, since there will never be an infinite amount of computational resources, some concessions must be made. Gauge configurations are generated

stochastically using the Hybrid Monte Carlo algorithm [13]. The algorithm introduces a ficticious simulation time and momentum, and evolves the configuration using Hamilton's equations of motion. Since we demand that the gauge fields be sufficiently different from each other, the algorithm proceeds through a number of iterations between each time a configuration is output. After the desired number of configurations has been generated, called an ensemble, valence quark propagators can then be calculated on each configuration.

The calculation of the fermion part of the path integral is computationally very expensive, due to the requirement of performing many fermion matrix inversions for each Hybrid Monte Carlo step [13]. One can ameliorate this somewhat by making use of the quenched approximation. This has the effect of blocking the production of quark-antiquark pairs in the vacuum, by setting the fermion determinant to 1, thereby giving sea quarks an infinite mass.

2.2 Fermion Fields

In order to calculate fermion fields on the lattice, we seek a discrete version of the Dirac action. Naively, one can approach this simply by replacing the continuum derivative by the symmetric discrete covariant derivative from Eq. (2.10). Employing mean field improvement on the gauge links as before, this gives,

$$\begin{aligned} S_N &= \bar{\psi}(x)(i\gamma_\mu \nabla_\mu + m_q)\psi(x) \\ &= \bar{\psi}(x)\frac{i}{2a}\sum_\mu \gamma_\mu\big(\tilde{U}_\mu(x)\psi(x+a\hat{\mu}) - \tilde{U}^\dagger_\mu(x-a\hat{\mu})\psi(x-a\hat{\mu})\big) + m\bar{\psi}(x)\psi(x). \end{aligned} \tag{2.32}$$

We can rewrite this in matrix form, in which we represent the spatial coordinates as indices,

$$M^N_{xy} = m_q\delta_{xy} + \frac{i}{2a}\sum_\mu \gamma_\mu\big(\tilde{U}_{x,\mu}\delta_{x,y-\mu} - \tilde{U}^\dagger_{x-\mu,\mu}\delta_{x,y+\mu}\big). \tag{2.33}$$

We can now rewrite the naive action as,

$$S_N = \sum_{x,y}\bar{\psi}_x M^N_{xy}\bar{\psi}_y. \tag{2.34}$$

This action is not acceptable however, as the Nielsen Ninomiya no-go theorem [14] states that a fermion action that respects the same set of symmetries as the gauge action, as well as respecting chiral symmetry, will always give rise to the fermion doubling problem. We can demonstrate this problem by explicitly solving for the quark two point function in the case of a trivial gauge field, that is $U_\mu(x) = \mathbb{I}$ for all x, μ. We begin by considering,

$$M_{xz} S_{zy} = \delta_{xy}, \tag{2.35}$$

where S_{zy} is the position space representation of the two point propagator in momentum space, given by,

$$S_{zy} = \frac{1}{V} \sum_k e^{-ik(z-y)} S(k). \tag{2.36}$$

We seek a form for $S(p)$ that resembles the continuum form of the two point function, except that p_μ will now be some function of the input momentum, k. Inserting the definition of the position space two point function into Eq. (2.35), and making use of the Fourier transform of the discrete δ function,

$$\begin{aligned} \frac{1}{V} \sum_k e^{-ika(x-y)} &= \frac{1}{V} \sum_{z,k} \Big(m_q \delta_{xz} + \frac{i}{2a} \sum_\mu \gamma_\mu \big(\delta_{x,z-\hat{\mu}} - \delta_{x,z+\hat{\mu}} \big) \Big) S(k) e^{-ika(z-y)} \\ &= \frac{1}{V} \sum_k \Big(m_q + \frac{1}{a} \sum_\mu \gamma_\mu \sin(ka) \Big) S(k) e^{-ika(x-y)}. \end{aligned} \tag{2.37}$$

If we set $p_\mu(k) = \frac{1}{a} \sin(k_\mu a)$, we see that the discrete momentum space two point function becomes,

$$S(p) = \frac{1}{\gamma_\mu p_\mu(k) + m_q}. \tag{2.38}$$

We can see that, in the limit that $k_\mu \to 0$, the continuum two point function is reproduced as required. When $k_\mu = n_\mu \frac{\pi}{a}$, where the components of n_μ are either 0 or 1, these 16 different values of k_μ have $p_\mu(k) = 0$. This gives rise to an additional 15 species of quark, known as doublers, that are not present in the continuum theory, and must be removed.

The most common way to resolve this problem is to introduce a mass dimension 5 operator to the fermion action. This term will scale proportional to the lattice spacing, and hence will be removed in the continuum limit. Wilson's

original choice for this dimension 5 operator [2] was the discrete version of the second covariant derivative, D^2, of the fermion fields, given by,

$$\begin{aligned}\bar{\psi}(x)\Delta_\mu\psi(x) &= \bar{\psi}(x)\overrightarrow{D_\mu}\overleftarrow{D_\mu}\psi(x) \\ &= \bar{\psi}(x)\frac{1}{a^2}\big(U_\mu(x)\psi(x+a\hat{\mu}) + U_\mu(x-a\hat{\psi})\psi(x-a\hat{\mu}) - 2\psi(x)\big).\end{aligned} \tag{2.39}$$

The Wilson fermion action is given by

$$S_W = \bar{\psi}(x)\sum_\mu \big(i\gamma_\mu\nabla_\mu + m_q + a\frac{r}{2}\Delta_\mu\big)\psi(x), \tag{2.40}$$

where r has been introduced as the Wilson parameter. Following the same procedure as above by writing the two point function with $p_\mu = p_\mu(k)$, the new effective lattice momentum is given by,

$$p_\mu(k) = \frac{1}{a}\sin(k_\mu a) + \frac{2r}{a}\sin^2(\frac{k_\mu a}{2}). \tag{2.41}$$

It is clear that, for all allowable values of $k_\mu \neq 0$, there will be no case where $p_\mu = 0$, the doublers will all have a mass proportional to the Wilson parameter, r and inversely proportional to a, thus removed in the continuum limit. In general, r is set to 1, as this allows the γ_μ matrices to act as projection operators. Because the momentum input to a lattice calculation is not the momentum generated, there are further limits placed on accessible momenta. Since we are restricted to the region $p_\mu(k) \approx k$, it is only reasonable to consider momentum

$$-\frac{N_S}{4} \lesssim p_\mu \lesssim \frac{N_S}{4}. \tag{2.42}$$

We can again write the action in matrix form

$$M^W_{xy} = (m_q + \frac{4r}{a})\delta_{xy} + \sum_\mu \big(\frac{\gamma_\mu + r}{2a}\tilde{U}_{x,\mu}\delta_{x,y-1} + \frac{\gamma_\mu - r}{2a}U_{\mu,x-1}\delta_{x,y+1}\big). \tag{2.43}$$

It is immediately evident that $\mathcal{O}(a)$ chiral symmetry is explicitly broken by the addition of the second derivative operator, as per the Nielson Ninomiya theorem.

At this stage, we introduce a new parameterisation for the quark mass,

$$\kappa = \frac{1}{2m_q a + 8r}. \tag{2.44}$$

This parameterisation allows us to rescale the action in such a way that all of the diagonal terms are 1, the matrix becomes

$$M^W_{xy} = \delta_{xy} + \kappa \sum_{\mu} \big((\gamma_\mu + r)\tilde{U}_{x,\mu}\delta_{x,y-1} + (\gamma_\mu - r)U_{\mu,x-1}\delta_{x,y+1} \big), \tag{2.45}$$

To accommodate the rescaling of the action, the quark fields must also be scaled,

$$\psi(x) \to \frac{\psi(x)}{2\kappa}. \tag{2.46}$$

This reformulation of the action gives rise to a redefinition of the quark mass,

$$2m_q = \frac{1}{\kappa} - \frac{1}{\kappa_c}, \tag{2.47}$$

where κ_c is the value of κ for which $m_q = 0$, known as the critical value. For the Wilson action, it is clear that $\kappa_c = 0.125$ in the non-interacting case. When interactions are introduced, the quark mass is additively renormalized and the critical value is not as clear. In order to determine κ_c, one must calculate the square of the pion mass at a variety of κ values. The leading order term in the chiral expansion of the pion mass gives $m_q \propto m_\pi^2$, therefore, the value of κ when m_π^2 is extrapolated to zero is the critical value.

Ideally, all lattice calculations would be done at the κ value corresponding to the physical pion mass, however, as the pion mass decreases, the fermion matrix becomes ill conditioned, and the iterative procedure used to calculate the inverse matrix, generally some variant of the conjugate gradient algorithm, takes longer to converge. This is particularly problematic for the generation of full QCD gauge configurations, where many matrix inversions have to be performed for each Hybrid Monte Carlo step.

Only recently has it become possible to perform large scale simulations near the physical pion mass, however, most calculations are performed at some heavier than physical pion mass. Quantities of any importance are usually calculated at multiple pion masses to give a basic assessment of the scaling, then an extrapo-

lation may be performed to the physical point.

Further improvements can be made to the fermion action by employing Symanzik's improvement program. Order a errors may be removed from on shell quantities by considering all possible dimension 5 operators allowed by lattice symmetries [15] that can be applied to the action. The first of these five operators was already considered by Wilson,

$$\mathcal{O}_1 = a\frac{r}{2}\bar{\psi}(x)(D^2)\psi(x). \tag{2.48}$$

The next operator we can consider,

$$\mathcal{O}_2 = b_g a m_q \mathrm{tr}(F_{\mu\nu}F^{\mu\nu}), \tag{2.49}$$

has the effect of renormalising the gauge coupling, such that $g^2 \to g^2(1 + b_g a m_q)$. Our scale setting procedure accounts for this.

Two more of these operators affect a renormalisation to the quark mass, these operators are,

$$\begin{aligned}\mathcal{O}_3 &= a b_m m_q^2 \bar{\psi}(x)\psi(x) \\ \mathcal{O}_4 &= a c_4 m_q \bar{\psi}(x)\big(\gamma_\mu \overleftarrow{D_\mu} - \gamma_\mu \overrightarrow{D_\mu}\big)\psi(x).\end{aligned} \tag{2.50}$$

It is possible to show that these terms are linearly dependent, thus we only include $\mathcal{O}_3$ into the action, this gives a renormalisation to the quark mass, $m_q \to m_q(1 + b_m a m_q)$. As we use the pion mass as a measure of m_q, this subtlety is not an issue. The final dimension 5 operator incorporated into the action is,

$$\mathcal{O}_5 = \frac{iagrC_{SW}}{4}\bar{\psi}(x)\sigma_{\mu\nu}F_{\mu\nu}\psi(x), \tag{2.51}$$

where $\sigma_{\mu\nu}$ are the gamma matrix commutators. Since there is no simple scaling that we can apply to incorporate this term, it is added directly into the Wilson action, forming the Sheikholeslami-Wohlert [16] action, giving

$$S_{SW} = S_N + \bar{\psi}(x)a\frac{r}{2}\Big(\Delta^2 - \frac{igC_{SW}}{2}\sigma_{\mu\nu}F_{\mu\nu}\Big)\psi(x), \tag{2.52}$$

where the parameter C_{SW} is the only parameter from all of the dimension 5 operators that needs to be tuned to remove the $\mathcal{O}(a)$ effects from the fermion

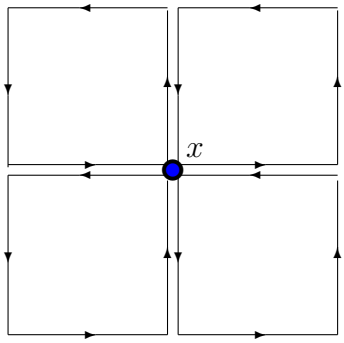

Figure 2.5: The links that compose the clover operator

action. The matrix form of this action is given by,

$$M_{xy}^{SW} = M_{xy}^{W} - \delta_{xy}\frac{\kappa i g C_{SW}}{2}\sigma_{\mu\nu}F_{\mu\nu}, \tag{2.53}$$

where r has been set to 1.

The field strength tensor must be calculated by a different method than in the gauge action, as we are now demanding symmetry around a lattice site, rather than the centre of a plaquette. This is accomplished by incorporating contributions from each plaquette in the μ, ν plane whose corner lies on x. Following a procedure similar to that considered in Sec. 2.1, we find that,

$$ga^2 F_{\mu\nu}(x) = \frac{1}{8i}\big((\mathcal{C}_{\mu\nu}(x) - \mathcal{C}_{\mu\nu}^{\dagger}(x)) - \frac{1}{3}\mathrm{Tr}(\mathcal{C}_{\mu\nu}(x) - \mathcal{C}_{\mu\nu}^{\dagger}(x))\big), \tag{2.54}$$

where $\mathcal{C}_{\mu\nu}$ is known as the 'clover' operator, so named for the shape of the links used in its construction shown in Fig. 2.5, and is given by

$$\begin{aligned}\mathcal{C}_{\mu\nu} = {} & U_\mu(x)U_\nu(x+\hat{\mu})U_\mu^\dagger(x+\hat{\mu}+\hat{\nu})U_\nu^\dagger(x+\hat{\nu}) \\ & + U_\nu(x)U_\mu^\dagger(x+\hat{\nu})U_\nu^\dagger(x-\hat{\mu}+\hat{\nu})U_\mu(x-\hat{\mu}) \\ & + U_\mu^\dagger(x-\hat{\mu})U_\nu^\dagger(x-\hat{\mu}-\hat{\nu})U_\mu(x-\hat{\mu}-\hat{\nu})U_\nu(x-\hat{\nu}) \\ & + U_\nu^\dagger(x-\hat{\nu})U_\mu(x-\hat{\nu})U_\nu(x+\hat{\mu}-\hat{\nu})U_\mu^\dagger(x)\end{aligned} \tag{2.55}$$

In order to determine the clover parameter C_{SW}, Sheikholeslami and Wohlert initially considered the energy states arising from the quark propagator as the on shell quantity to improve. They showed that, at tree level, $C_{SW} = 1$. For small momenta, it provided the best approximation to the continuum energy momen-

tum relation whilst removing an unphysical state that arises from an additional pole in the quark propagator introduced by the lattice discretisation. One can consider mean field improvement to the clover term by either setting,

$$C_{SW} = \frac{1}{u_0^3}, \tag{2.56}$$

or simply calculating the plaquettes with the mean field improved links, $\tilde{U}_\mu(x)$. It is possible to tune C_{SW} non-perturbatively, and thus remove $\mathcal{O}(a)$ effects to all powers of g for some on-shell quantity by employing the Schrödinger functional approach [17, 18]. However, the process of non-perturbatively tuning the clover parameter is extremely computationally intensive.

The issue of tuning the clover operator can be avoided entirely by implementing on shell improvement directly into the gauge configurations themselves. We can implement so-called 'fat links', described in the next section, to the dimension 5 operators in the clover action. These fat, or, smeared links have the effect of removing high energy fluctuations in the gauge fields in a much more robust manner to mean field improvement alone. This leaves only large scale, low energy structure, which is the principle requirement for on shell improvement. The Fat Link Irrelevant Clover (FLIC) action [19, 20] is given by

$$S_{FLIC} = S_N + \bar{\psi}(x) a \frac{r}{2} \big(D^{2,FL} - \frac{ig}{2} \sigma_{\mu\nu} F^{FL}_{\mu\nu} \big) \psi(x), \tag{2.57}$$

where $D^{2,FL}$ and $F^{FL}_{\mu\nu}$ are calculated as before, with the exception of the use of the smeared gauge links. Note that due to the use of smeared links, it is no longer necessary to tune the clover parameter, and we can set C_{SW} to the tree-level value of 1.

When calculating the quark propagator, one must invert M_{xy} for the selected action using some source vector, ψ, thus solving for χ,

$$M^{ab}_{xy,ij} \chi^b_j(y) = \psi^a_i(x), \tag{2.58}$$

where i, j are spinor indices and a, b are colour indices, which have been omitted until this point. Ideally, we would be able to perform this inversion for a delta

function, or point source, that is,

$$\psi_i^a(x) = \delta^{ac}\delta_{ik}\delta_{xz}, \tag{2.59}$$

for all values of c, k and z. This is impractical, however, as this would require 12 matrix inversions for every lattice site, *i.e.* millions of total inversions. When a point source is considered, periodic boundary conditions allow a choice of any lattice site for z, and a single inversion is performed for each of the colour and spin indices per configuration. A single point is an equally poor approximation for all hadron wave functions, thus, point sources are only considered when coupling to many states is demanded.

For better isolation of a single state, we require a source that better approximates the wave function of the particle we wish to consider. This is constructed by smearing a point source in a gauge covariant manner [21]. Once a source has been decided upon, M^{-1} is calculated using, in our case, the stabilized biconjugate gradient algorithm [22, 23]. After the propagator has been calculated, it is possible to apply smearing to the 'sink' indices to further improve coupling to hadron states. Sink smearing is required in the construction of a variational basis to extract excited hadron states, which will be described later.

2.3 Smearing Gauge Fields

Smearing has the effect of removing short distance fluctuations in the gauge field by averaging each link with its nearest neighbours iteratively. This is accomplished by considering the 'staples' *i.e.* 3 link objects that have the same start and end points as a single link [24, 25], shown in Fig. 2.6, and given by

$$U_\mu^{(n)}(x) \to U_\mu^{(n+1)}(x) = (1-\alpha)U_\mu^{(n)}(x) + \frac{\alpha}{6}\sum_\mu Q_\mu^{(n)}(x), \tag{2.60}$$

where (n) represents the nth iteration of the smearing procedure, α is some coefficient tuned to give the ideal contribution from the staples, usually set to

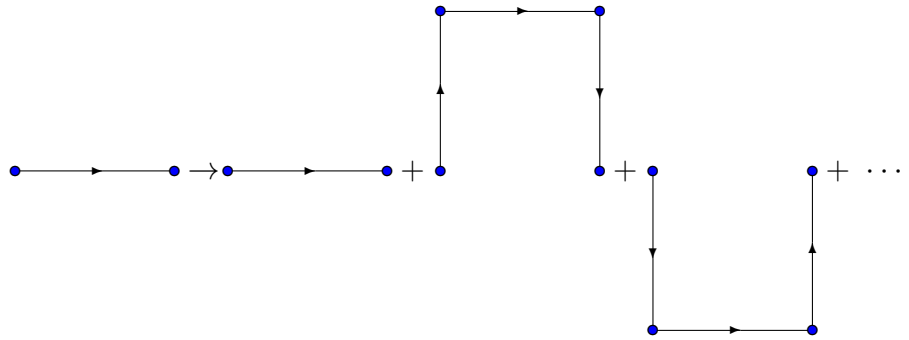

Figure 2.6: The links used to construct the smeared gauge fields

0.7, and,

$$Q_\mu^{(n)}(x) = \sum_{\mu\neq\nu} \big(U_\nu^{(n)}(x)U_\mu^{(n)}(x+\hat{\mu})U_\nu^{(n)\dagger}(x+\hat{\mu}) + U_\nu^{(n)\dagger}(x-\hat{\nu})U_\mu^{(n)}(x-\hat{\nu})U_\mu^{(n)}(x-\hat{\nu}+\hat{\mu})\big). \tag{2.61}$$

This smearing procedure, known as APE smearing, involves a sum over $SU(3)$ matrices. Therefore, the resulting $Q_\mu^{(n)}(x)$ is gauge dependent and needs to be projected back to $SU(3)$. Each iteration averages the short distance effects, therefore leaving only long distance, low energy structure. It is nonperturbative in that the problematic perturbative tadpole contributions have been removed. To that end, it facilitates on shell improvement for operators at greatly reduced cost.

Morningstar and Peardon[26] proposed an improvement to APE smearing, known as Stout smearing, which performs the same function as APE smearing multiplicatively, therefore removing the requirement to project the links back in to $SU(3)$. It is given by,

$$\begin{aligned} U_\mu^{(n+1)}(x) = \exp\big(&i\alpha(Q_\mu^{(n)}(x)U_\mu^{(n)\dagger} - U_\mu^{(n)}(x)Q_\mu^{(n)\dagger}) \\ &- \frac{1}{6}\mathrm{Tr}(Q_\mu^{(n)}(x)U_\mu^{(n)\dagger} - U_\mu^{(n)}(x)Q_\mu^{(n)\dagger})\big), \end{aligned} \tag{2.62}$$

where α is generally set to 0.1. The exponential can be evaluated exactly using the Cayley-Hamilton theorem, which, for a traceless hermitian matrix states that

$$Q^3 = \frac{1}{2}\mathrm{Tr}(Q^2)Q + \frac{1}{3}\mathrm{Tr}(Q^3)\mathbb{I}. \tag{2.63}$$

This implies that any Q^n where $n \geq 3$ can be expressed as a linear combination

of Q^2, Q and $\mathbb{I}$. Since the taylor expansion of the exponential is an infinite polynomial, coefficients can be determined such that,

$$e^{iQ} = f_0\mathbb{I} + f_1 Q + f_2 Q^2, \tag{2.64}$$

where the f_j are a function of $c_0 = \frac{1}{3}\mathrm{Tr}(Q^3)$ and $c_1 = \frac{1}{2}\mathrm{Tr}(Q^2)$. From the definition of Q, the maximum absolute value c_0 can take is.

$$c_0^{max} = 2(\frac{1}{3}c_1)^{3/2}. \tag{2.65}$$

The variables u, v and θ are introduced, given by,

$$\begin{aligned} u &= \sqrt{\frac{1}{3}c_1}\cos(\frac{1}{3}\theta) \\ v &= \sqrt{c_1}\sin(\frac{1}{3}\theta) \\ \theta &= \arccos\Big(\frac{c_0}{c_0^{max}}\Big), \end{aligned} \tag{2.66}$$

and it can be shown that the f_j can be written as,

$$f_j = \frac{h_j}{9u^2 - w^2}, \tag{2.67}$$

where,

$$\begin{aligned} h_0 &= (u^2 - w^2)e^{2iu} + e^{-iu}(8u^2\cos(w) + 2iu(3u^2 + w^2)\frac{\sin w}{w}) \\ h_1 &= 2ue^{2iu} - e^{-iu}(2u\cos(w) - i(3u^2 - w^2)\frac{\sin w}{w}) \\ h_2 &= e^{2iu} - e^{-iu}(\cos(w) + 3iu\frac{\sin w}{w}). \end{aligned} \tag{2.68}$$

Stout smearing is generally applied to gauge fields when irrelevant operators are in use, as it is critical that the gauge fields remain in $SU(3)$.

Gusken [21] proposed a method of smearing for fermions. The source and sink vectors are acted upon by an iterative function

$$\chi^{(n+1)}(x) = F(x,y)\chi^{(n)}(x), \tag{2.69}$$

where,

$$F(x,y) = (1-\alpha)\delta_{xy} + \frac{\alpha}{6}\sum_{\mu=1}^{3}\left(U_\mu^\dagger(x-a\hat{\mu})\delta_{x,y+\hat{\mu}} + U_\mu(x)\delta_{x,y-\hat{\mu}}\right). \tag{2.70}$$

This smearing has the effect of building a Gaussian profile from a point source that better approximates a particle's wave function.We let α take the same value of 0.7 in gaussian smearing as it does in APE smearing, then vary the number of iterations.

2.4 Background Field Method

The background field method [27, 28] applies a constant electromagnetic field to the lattice by introducing a phase to the $SU(3)$ links. Since we are only concerned with the magnetic properties of the proton, we will only consider a magnetic field, though a similar method can by applied for electric properties [29]. The symmetries of the lattice allow us to consider a field along one axis only, therefore we will chose the z axis, setting $\vec{B} = (0,0,B_z)$, which will align the field with the proton's spin. In order to accomplish this, we begin with the continuum definition of the magnetic field, $\vec{B} = \vec{\nabla} \times \vec{A}$, or, for a field specifically in the z direction.

$$B_z = \partial_x A_y^{EM} - \partial_y A_x^{EM}. \tag{2.71}$$

Like the $SU(3)$ gauge fields, we must reformulate the magnetic field in terms of the link variables. In order to do this, we consider the plaquette in the xy plane constructed by the vector potential,

$$W_{xy}(x,y,z,t) = -W_{yx}(x,y,z,t) = e^{ia^2eF_{\mu\nu}} = e^{ia^2eB_z}, \tag{2.72}$$

There are many vector potentials that give rise to such a magnetic field and we will consider two such constructions. Recalling the definition of the plaquette, we set the electromagnetic link variables in the y direction to,

$$U_y(x,y,z,t) = e^{iaeBx}, \tag{2.73}$$

and all other $U_\mu = 1$. Away from the periodic boundary, this gives,

$$\begin{aligned} W_{xy}(x, y, z, t) &= e^{ia^2eB(x+1)-ia^2eBx} \\ &= e^{ia^2eB}, \end{aligned} \tag{2.74}$$

as required. On the boundary in the x-direction, an extra phase is introduced by crossing the periodic boundary,

$$\begin{aligned} W_{xy}(N_S, y, z, t) &= e^{ia^2eBN_S-ia^2eB} \\ &= e^{ia^2eB(N_S-1)}. \end{aligned} \tag{2.75}$$

In order to remove this additional phase, we set the links in the x direction along the x boundary to,

$$U_x(N_S, y, z, t) = e^{ia^2eBN_SBy}. \tag{2.76}$$

The plaquette crossing the boundary then becomes,

$$\begin{aligned} W_{xy}(N_s, y, z, t) &= e^{ia^2eBN_S+ia^2eN_SBy-ia^2eB-ia^2eN_SB(y+1)} \\ &= e^{ia^2eB}, \end{aligned} \tag{2.77}$$

as required.

On the corner of the xy plane, the plaquette becomes

$$W_{xy}(N_S, N_S, z, t) = e^{ia^2eB}e^{-ia^2eN_S^2B}. \tag{2.78}$$

It is evident that, in order to meet the requirement of a constant field at every site on the lattice, the field must be quantised such that,

$$eB = \frac{2\pi n}{N_S^2}, \tag{2.79}$$

where n is an integer. We note that, due to the fractional charges of the quarks, the smallest non-zero physical field that can be considered at the hadron level has $n = 3$. The continuum version of this field is given by $\vec{A} = (0, Bx, 0)$. It is possible to define the same magnetic field with a second vector potential,

$$\vec{A} = (-By, 0, 0). \tag{2.80}$$

The link variables then become,

$$\begin{aligned} U_x(x,y,z,t) &= e^{-ia^2eBy} \\ U_y(x,y,z,t) &= 1 \quad \forall y \neq N_S \\ U_y(x,N_S,z,t) &= e^{-ia^2eBN_Sx} \\ U_z(x,y,z,t) &= U_t(x,y,z,t) = 1. \end{aligned} \tag{2.81}$$

Following the same procedure as before, it can be shown that this vector potential generates the same quantisation conditions as the first field considered. Furthermore, the two vector potentials are related by a gauge transformation.

$$G(x,y,z,t) = e^{ieBxy}. \tag{2.82}$$

The quantisation conditions required by the lattice lead to very large magnetic fields, leading to a mass splitting of the spin up and spin down proton of up to 30% of the particles mass. The key concern is that such a large field will have a detrimental effect on the ability of any operator to couple to the particle in the field. Furthermore, the field could be so large that the particle itself bears little resemblance to its zero field form. For this reason, the wave function becomes the ideal tool to investigate the effect of the magnetic field of the proton, as it allows us to directly visualise the effect of the field on the particle.

Chapter 3

Wave Functions

3.1 Two Point Functions

The two-point function is of fundamental importance in extracting hadron spectra from lattice QCD. Many important properties of of hadrons can also be extracted from the two point function. These include, but are not limited to, masses, magnetic moments [30, 31, 32] and polarisabilities [33] when a background field is introduced, and relativistic effects [34].

It is also possible to extract excitations of hadrons using linear superpositions of two point functions. Further information on extracted states can be obtained by considering the position space wave function [34, 35, 36, 37]. The wave function is used as a visual tool to show the effects of magnetic fields and momentum on the particle, and can also aid as a diagnostic tool for the lattice, allowing one to easily view finite volume effects, or the quality of the coupling of a state to the operator used.

On the lattice the Minkowski space two point function is given by,

$$G_{ij}(\vec{p},t) = \sum_{x} e^{-i\vec{p}\cdot\vec{x}} \langle \Omega | \chi_i(x) \bar{\chi}_j(0) | \Omega \rangle, \tag{3.1}$$

where the Dirac indices have been suppressed and the discrete version of the 3-dimensional Fourier transform is used for the projection to momentum space. The χ_i and $\bar{\chi}_j$ are the annihilation and creation operators respectively of some state. It is important to note here that momentum is an input parameter to the lattice two point function, and thus can be chosen according to the constraints

imposed by the discrete space time.

In order to determine how exactly a spectrum is extracted, we insert a complete set of baryon, spin and momentum states between the creation and annihilation operators

$$\mathbb{I} = \sum_{B,q,s} |B,q,s\rangle\langle B,q,s|, \tag{3.2}$$

giving,

$$G_{ij}(\vec{p},t) = \sum_{x} e^{-i\vec{p}\cdot\vec{x}} \sum_{B,q,s} \langle\Omega|\chi_i(x)|B,q,s\rangle\langle B,q,s|\bar{\chi}_j(0)|\Omega\rangle. \tag{3.3}$$

It is at this point we move the space time dependence from the operator $\chi_i(x)$ by invoking the space time translation operator. This gives,

$$G_{ij}(\vec{p},t) = \sum_{x}\sum_{B,q,s} e^{-i\vec{p}\cdot\vec{x}} \langle\Omega|e^{i\hat{p}x}\chi_i(0)e^{-i\hat{p}x}|B,q,s\rangle\langle B,q,s|\bar{\chi}_j(0)|\Omega\rangle, \tag{3.4}$$

where $\hat{p}$ is the 4-momentum operator. Applying the operators on the states gives,

$$\begin{aligned} G_{ij}(\vec{p},t) &= \sum_{x}\sum_{B,q,s} e^{-i\vec{p}\cdot\vec{x}} \langle\Omega|\chi_i(0)e^{iqx}|B,q,s\rangle\langle B,q,s|\bar{\chi}_j(0)|\Omega\rangle \\ &= \sum_{x}\sum_{B,q,s} e^{-iE_Bt - i(\vec{p}-\vec{q})\cdot\vec{x}} \langle\Omega|\chi_i(0)|B,q,s\rangle\langle B,q,s|\bar{\chi}_j(0)|\Omega\rangle, \end{aligned} \tag{3.5}$$

where E_B is the energy of the baryon state. We note that the Kronecker delta function in three dimensions is defined as,

$$\delta_{\vec{p},\vec{q}} = \sum_{x} e^{-i(\vec{p}-\vec{q})\cdot\vec{x}}, \tag{3.6}$$

and applying this and Eq. (3.5) gives,

$$G_{ij}(\vec{p},t) = \sum_{B,s} e^{-iE_Bt} \langle\Omega|\chi_i(0)|B,p,s\rangle\langle B,p,s|\bar{\chi}_j(0)|\Omega\rangle. \tag{3.7}$$

The quantity $\langle\Omega|\chi_i(0)|B,p,s\rangle$ can be represented as the product of a normalised Dirac spinor and some complex number that represents the relative coupling of

each state to the interpolating fields. *i.e.*

$$\langle\Omega|\chi_i(0)|B,p,s\rangle\langle B,q,s|\bar{\chi}_j(0)|\Omega\rangle = \sqrt{\frac{M}{E_B}}u(p,s)\lambda_{B,i}(p)\sqrt{\frac{M}{E_B}}\bar{u}(p,s)\lambda^*_{B,j}(p). \tag{3.8}$$

As these spinors are normalised, we are able to directly evaluate the sum over the spin,

$$G_{ij}(\vec{p},t) = \sum_B e^{-iE_Bt}\frac{\not{p}+M}{2E_B}|\lambda_B(p)|^2, \tag{3.9}$$

where $\lambda_B(p)$ is a momentum dependent complex number associated with the coupling strength of the particle B to the operators chosen. When the two point function is Wick rotated to Euclidean space *i.e.* $t \to -it$, we can see that the end result is a 'tower' of states whose signal decays proportional to the exponential of the relativistic energy. In the case that the input momentum is zero, this becomes the particles mass. Hence, by looking at time slices sufficiently far from the source, the ground state that couples to the chosen operator will dominate the signal. Furthermore, in the zero momentum case,

$$\frac{\not{p}+M}{2E_B} \to \frac{\gamma_0+\mathbb{I}}{2}, \tag{3.10}$$

which projects either the positive or negative parity states, depending on the transformation properties of the operator chosen.

In order to extract the mass from the two point function, one constructs a time-dependent 'effective mass',

$$M_{eff} = \log\Big(\frac{G(0,t)}{G(0,t+1)}\Big). \tag{3.11}$$

One then proceeds to perform a constant fit to the effective mass in the region where the ground state dominates.

A particle on the lattice undergoes an energy shift induced by the magnetic field, given by,

$$\Delta E = E(\vec{B}) - M_{eff} = \frac{|e\vec{B}|}{2m} - \hat{\mu}\cdot\vec{B} + \frac{e^2}{2}\beta_M B^2, \tag{3.12}$$

The first term denotes the lowest of the Landau levels, which is an energy induced

by cyclotron-type orbits in the background field. We consider only the lowest energy level, as it is assumed that the higher energy states have sufficiently decayed. The second term is the magnetic moment, which is proportional to the spin of the particle, and hence induces a spin dependent mass splitting. The third term contains the magnetic polarizability, β_M, and is proportional to the square of the elementary electromagnetic charge.

It is most beneficial to isolate a single state as early as possible, as the signal to noise ratio will be highest, and the fit most accurate. The addition of Gaussian smearing to the fermion source causes the linear superposition of states in the source to change. It is therefore apparent that there is the possibility of removing contributions from excited states by selecting an optimal amount of smearing. Methods for the suppression of excited states, and thus maximising the contribution of the ground state to the two point function will be discussed in Chapter 4.

Since the change invoked by the magnetic field appears in the energy of the particle, the two point function is the ideal tool to employ to investigate the effects of an external field. Further to this, since the wave function is proportional to the two point function, magnetic effects will be present when calculating the wave function.

The choice of operator for the two-point function is determined by the quantum numbers of the particle being investigated. In the case of the proton, the operator must have a total spin of $\frac{1}{2}$, isospin $+\frac{1}{2}$, positive parity, colour antisymmetry, and transform under the Lorentz group as a Dirac spinor. Whilst it is possible to construct a large number of operators that fulfill these requirements, there are three that are usually considered [38],

$$\begin{aligned}
\chi_1(x) &= \epsilon^{abc}(u_a^T(x)C\gamma_5 d_b(x))u_c(x) \\
\chi_2(x) &= \epsilon^{abc}(u_a^T(x)C d_b(x))\gamma_5 u_c(x) \\
\chi_4(x) &= \epsilon^{abc}(u_a^T(x)C\gamma_5\gamma_4 d_b(x))u_c(x),
\end{aligned} \tag{3.13}$$

where u and d represent the Dirac spinors for the up and down quarks respectively. The χ_1 operator, which contains scalar ud pair with the remaining u quark carrying the spinor index is the most commonly used operator when only the ground state is being considered. This operator has been shown [39] to pro-

vide better overlap by a factor of 100 over χ_2, which contains a vector ud pair. The χ_2 operator is considered in situations where states other than the ground states are being investigated. The χ_4 operator is the time component of the spin $\frac{3}{2}N^+$.

We insert χ_1 and its adjoint,

$$\bar{\chi}_1(0) = \epsilon^{a'b'c'}\bar{u}_{c'}(0)(\bar{d}_{b'}(0)\gamma_5\bar{u}^T_{a'}(0)), \tag{3.14}$$

in to the definition of the two point function in Eq. 3.1. This gives,

$$G_{11}(p,t) = \sum_x e^{-i\vec{p}\cdot\vec{x}}\langle\Omega|\epsilon^{abc}(u^T_a(x)C\gamma_5 d_b(x))u_c(x)\epsilon^{a'b'c'}\bar{u}_{c'}(0)(\bar{d}_{b'}(0)\gamma_5\bar{u}^T_{a'}(0))|\Omega\rangle, \tag{3.15}$$

By performing both sets of possible Wick contractions between the six quark and anti-quark fields, we can construct the full two point function for the proton in terms of quark propagators.

$$G_{11}(\vec{p},t) = -\sum_x e^{-i\vec{p}\cdot\vec{x}}\epsilon^{abc}\epsilon^{a'b'c'}\big(S_u^{cc'}(x,0)\mathrm{tr}(C\gamma_5 S_d^{bb'}(x,0)C\gamma_5)^T S_u^{aa'}(x,0) + (S_u^{cc'}(x,0)(C\gamma_5 S_d^{bb'}(x,0)C\gamma_5)^T S_u^{aa'}(x,0)\big) \tag{3.16}$$

Until now, we have limited the discussion to the case where only properties of the ground state are of interest. This is not always the case however, as it is beneficial to be able to study higher energy excitations of the particle. On the lattice, this is accomplished by the variational method.

3.2 Variational Method

By virtue of the fact that the two point function is composed of a linear superposition of exponentials, it is possible to construct a 'correlation' matrix [38, 40, 41, 42, 43, 44, 45] of two point functions whose eigenvectors can be used to project individual states from the two point function. We are able to do so due to the fact that the different operators give rise to weights on each of the states present. As the only time dependence in the two point function is in the

exponential, we construct the following right eigenvector equation.

$$G_{ij}(t_0 + \Delta t)u_j^B = e^{-M_B \Delta t} G_{ij}(t_0) u_j^B, \tag{3.17}$$

where

$$\bar{\phi}^B \equiv u_i^B \bar{\chi}_i \tag{3.18}$$

is a perfect creation operator, exciting only state B. Here t_0 and Δt can be chosen to lie in a region where the operators show the greatest variance in the superposition of the states, allowing the most reliable projection possible. We can rewrite Eq. (3.17) as,

$$[G^{-1}(t_0)G(t_0 + \Delta t)]_{ij} u_j^B = c_B u_i^B, \tag{3.19}$$

where $c_B = e^{-M_B \Delta t}$ is the eigenvalue for the baryon state B and u^B the corresponding eigenvector. Similarly, we are able to construct the left eigenvector equation,

$$v_i^{B'} G_{ij}(t_0 + \Delta t) = e^{-M_{B'} \Delta t} v_i^{B'} G(t_0). \tag{3.20}$$

We can rewrite this in a similar manner to Eq. (3.17)

$$v_i^{B'} [G(t_0 + \Delta t)G^{-1}(t_0)]_{ij} = v_j^{B'} c_{B'}. \tag{3.21}$$

The eigenvectors can then be used to diagonalise the correlation matrix as follows, allowing the isolation of a single state.

$$v_i^{B'} G(t)_{ij} u_j^B \propto \delta^{B'B}. \tag{3.22}$$

The projected two-point function can be then be treated as before and quantities such as the effective mass of the projected state are able to be calculated.

One must be careful with the choice of operators used to construct the variational basis, as if the two-point functions generated by the combination of any two operators give rise to the same superposition of states, the matrix will become singular, and thus, uninvertible. As there are few local operators that allow the reliable extraction of proton states, construction of the variational basis by varying the spin-flavour configuration of the interpolator alone is not sufficient to extract information about the excited states. One can increase the size of

the basis by introducing smearing to the operators [43, 44, 45].These references show that, in the region close to the source, different levels of smearing give the greatest variations to the weightings of each state present in the superposition. Therefore, an ideal choice of operators to construct the variational basis are the χ_i operators combined with different levels of smearing.

3.3 Wave Function Operators

In quantum field theory, a Schrödinger-like probability distribution can be constructed for bound states by taking a simplified view of the full quantum field theory wave functional in the form of the Bethe-Salpeter wave function [46], herein referred to as simply the 'wave function'.

The Bethe-Salpeter wave function underlying the probability distributions can be defined in the form of a gauge-invariant Bethe-Salpeter amplitude. For the wave function of the d quark about two u quarks in the proton, $|p\rangle$, the amplitude takes the form

$$\begin{aligned}\psi_d^p(y) \quad \propto \quad & \int d^4x \, \langle\Omega| \, \epsilon^{abc} \, u^{\mathsf{T}a}(x) \, C\gamma_5 \\ & \left[P \exp\left(ig \int_x^{x+y} A(x') \cdot dx'\right) d(x+y)\right]^b \\ & u^c(x) \, |p\rangle \, ,\end{aligned} \tag{3.23}$$

which exploits a string of flux to connect the quarks in a gauge invariant manner. Here we have selected the standard form of the proton interpolating field χ_1, u and d represent the up and down quark fields respectively with colour indices a, b and c and C is the charge conjugation matrix.

We can interpret the two-point function as the amplitude for the baryon B to be created at some time 0, with momentum $\vec{p}$ and annihilated some time t later. If we give each of the quarks within the interpolating operator a spatial dependence, *i.e.*

$$\chi(\vec{x}, \vec{y}, \vec{z}, \vec{w}) = \epsilon^{abc}(u_a^T(\vec{x}+\vec{y})C\gamma_5 d_b(\vec{x}+\vec{z}))u_c(\vec{x}+\vec{w}), \tag{3.24}$$

we are able to interpret the two point function constructed from this operator

and its adjoint at the point where $\vec{x} = \vec{y} = \vec{z} = \vec{w} = 0$,

$$G_{WF}(\vec{p}, t, \vec{y}, \vec{z}, \vec{w}) = \sum_{x} e^{-i\vec{p}\cdot\vec{x}} \epsilon^{abc}\epsilon^{a'b'c'} \\ \big(S_u^{cc'}(\vec{x}+\vec{w},0)\mathrm{tr}(C\gamma_5 S_d^{bb'}(\vec{x}+\vec{z},0)C\gamma_5)^T S_u^{aa'}(\vec{x}+\vec{y},0) \\ +(S_u^{cc'}(\vec{x}+\vec{w},0)(C\gamma_5 S_d^{bb'}(\vec{x}+\vec{z},0)C\gamma_5)^T S_u^{aa'}(\vec{x}+\vec{y},0)\big), \tag{3.25}$$

as the amplitude for some baryon B to be created at some spacetime point 0, with momentum $\vec{p}$, and have each of its quarks annihilated at three separate spatial points some time later [34, 35, 36, 37, 47]. In principle, we can then calculate G_{WF} for all values of $\vec{y}, \vec{z}$ and $\vec{w}$ and, giving regard to the centre of mass, normalise this to form a complete wave function. This approach is not feasible, however, as it requires on the order of N_S^6 standard two point functions to be calculated per time slice. We are able to reduce the complexity of the problem by taking advantage of the symmetries available on the lattice.

The combination of periodic boundary conditions and cubic rotational symmetry allows us to consider the case where one of $\vec{y}, \vec{z}$ or $\vec{w}$ varies across the entire lattice and the other two quarks are separated along only the x axis by some distance d. In the case of the d quark wave function, the interpolating operator becomes,

$$\chi(\vec{x}, \vec{d_1}, \vec{z}, \vec{d_2}) = \epsilon^{abc}(u_a^T(\vec{x}+\vec{d_1})C\gamma_5 d_b(\vec{x}+\vec{z}))u_c(\vec{x}+\vec{d_2}), \tag{3.26}$$

where $\vec{d_1} = (d_1, 0, 0)$ and $\vec{d_2} = (d_2, 0, 0)$. When the u quarks are separated by an even number of lattice sites, $d_1 = -d_2$ and where they are separated by an odd number of lattice sites, $d_1 = -(d_2 + 1)$. This reduces the number of two point function calculations to $\frac{3}{2}N_S^4$ per time slice.

We then proceed to normalise the wave function by introducing a time dependent factor $\xi(t)$ such that,

$$\sum_{\vec{y}} \xi^2(t)|G_{WF}(\vec{p}, t, 0, \vec{y}, 0)|^2 = 1, \tag{3.27}$$

with the same factor used to normalise the wave functions for all values of d_1, d_2. It is clear that the wave function defined in Eq. (3.25) is a gauge dependent

quantity, hence, unless one of two possible remedies is applied, the ensemble average of every point other than the point where the three quarks are colocated will be zero.

In a relativistic gauge theory the concept of a hadronic wave function is not unique and the Bethe-Salpeter wave function underlying the probability distributions can be defined in several different forms. For example, the gauge-invariant Bethe-Salpeter amplitude exploits a string of flux to connect the quarks annihilated at different spatial positions in a gauge invariant manner. Naively, this is a computationally simple choice, as it requires little more than a series of 3×3 matrix multiplications. As this leads to an explicit path dependence, an average over the paths is desirable. At this point, apparent simplicity breaks down as even on a small lattice, it is possible to define billions of paths between any two lattice sites. Therefore, the only way to form a complete picture of the wave function would be to consider all possible paths between each of the quarks, adding enormous complexity. Another approach considers Bethe-Salpeter amplitudes in which the gauge degree of freedom is fixed to a specific gauge. In lattice field theory, Coulomb and Landau gauges are most common due to their local gauge fixing procedure. Landau gauge provides distributions that compare favorably with constituent quark model predictions [48] and therefore we select Landau and Coulomb gauges herein.

3.4 Gauge Fixing

Gauge fixing on the lattice [49, 50] is accomplished by computing a gauge transformation to apply to a configuration that causes the transformed configuration to satisfy some classical gauge fixing condition. In the case of the Landau gauge, the condition is

$$\sum_{\mu=1}^{4} \partial_\mu A_\mu = 0, \tag{3.28}$$

and for the Coulomb gauge,

$$\sum_{i=1}^{3} \nabla_i A_i = 0. \tag{3.29}$$

In order to calculate the gauge transformation, we choose a functional to iteratively maximise such that the maximum condition matches the gauge fixing

condition. In the case of both the Landau and Coulomb gauges, this functional is given by.

$$\mathcal{F}_1 = \sum_{\mu,x}^{N} \frac{1}{2} \mathrm{Tr}(U_\mu^{(n)}(x) + U_\mu^{\dagger(n)}(x)), \tag{3.30}$$

where $N = 4$ for the Landau gauge and $N = 3$ for the Coulomb gauge. The gauge transformed configuration at the n-th iteration of functional maximisation is given by

$$U_\mu^{(n)}(x) = G^{(n)}(x) U_\mu^{(n-1)}(x) G^{(n)}(x+\mu), \tag{3.31}$$

where $G(x)$ is the gauge transformation to be calculated, parameterised by

$$G(x)^{(n)} = \exp(i\omega_a^{(n)}(x)\,\tau^a), \tag{3.32}$$

and ω is defined in the following discussion. We can take the variation of the functional with respect to $\omega^{(n)}$ in order to verify the fact that it matches the continuum gauge fixing condition,

$$\frac{\delta \mathcal{F}_1}{\delta \omega_a^{(n)}(x)} = \frac{i}{2} \sum_{\mu,x} \mathrm{Tr}(\Delta_{1,\mu}^{(n)}(x)) \tau^a, \tag{3.33}$$

where,

$$\Delta_{1,\mu}^{(n)}(x) = \big(U_\mu^{(n)}(x-\mu) - U_\mu^{(n)}(x) + U_\mu^{\dagger(n)}(x) - U_\mu^{\dagger(n)}(x-\mu)\big). \tag{3.34}$$

By using the definition of the link from Eq. (2.6), we can Taylor expand the gauge fields around $A_\mu(x)$, perform the integration, then expand the exponentials to first order. This gives

$$\frac{\delta \mathcal{F}_1}{\delta \omega_a^{(n)}(x)} = \frac{i}{2} \sum_{\mu,x} \mathrm{Tr}\big(a^2 \partial_\mu A_\mu + \frac{a^4}{12} \partial_\mu^3 A_\mu + \mathcal{O}(a^6)\big). \tag{3.35}$$

We can see that when $\mathcal{F}_1$ is maximised, the continuum gauge fixing condition is satisfied to $\mathcal{O}(a^2)$. It is possible to construct a linear combination of functionals containing up to n links to enforce the gauge fixing condition to $\mathcal{O}(a^{2n})$ [50]. We

will now consider the $n = 2$ case. The two link functional is given by

$$\mathcal{F}_2 = \sum_{\mu,x}^{N} \frac{1}{2}\mathrm{Tr}(U_\mu^{(n)}(x)(U_\mu^{(n)}(x+\mu) + U_\mu^{\dagger(n)}(x)U_\mu^{\dagger(n)}(x-\mu)), \tag{3.36}$$

Once again, we take the variation of the functional with respect to $\omega_a^{(n)}$, giving,

$$\frac{\delta\mathcal{F}_2}{\delta\omega_a(x)} = \frac{i}{2}\sum_{\mu,x}\mathrm{Tr}(\Delta_{2,\mu}(x))\tau^a, \tag{3.37}$$

where,

$$\begin{aligned}\Delta_{2,\mu}^{(n)}(x) = \big(&U_\mu^{(n)}(x-2\mu)U_\mu^{(n)}(x-\mu) - U_\mu^{(n)}(x)(U_\mu^{(n)}(x+\mu)+ \\ &U_\mu^{\dagger(n)}(x+\mu)U_\mu^{\dagger(n)}(x) - U_\mu^{\dagger(n)}(x-\mu)U_\mu^{\dagger(n)}(x-2\mu)\big).\end{aligned} \tag{3.38}$$

Performing the same sequence of Taylor expansions as before gives.

$$\frac{\delta\mathcal{F}_2}{\delta\omega_a^{(n)}(x)} = \frac{i}{2}\sum_{\mu,x}\mathrm{Tr}\big(4a^2\partial_\mu A_\mu + \frac{4a^4}{3}\partial_\mu^3 A_\mu + \mathcal{O}(a^6)\big). \tag{3.39}$$

We can see that, by performing the maximisation of the functional,

$$\mathcal{F}_{12} = \frac{4}{3}\mathcal{F}_1 - \frac{1}{12u_0}\mathcal{F}_2, \tag{3.40}$$

the continuum gauge fixing condition will be satisfied to $\mathcal{O}(a^4)$, *i.e.* it has been $\mathcal{O}(a^2)$-improved. In order to ensure our expansion of this link is $U_\mu(x) = 1+$ small corrections, we have introduced a factor of the mean link for the extra link in the two-link term.

The gauge transformation that performs the maximisation is set to

$$G^{(n+1)}(x) = \exp\Big(\frac{\alpha}{2}\sum_\mu\big(\Delta_{12,\mu}^{(n)}(x) - \frac{1}{3}\mathrm{Tr}\Delta_{12,\mu}^{(n)}(x)\big)\Big). \tag{3.41}$$

where α is a sufficiently small constant and $\Delta_{12,\mu}^{(n)}(x)$ takes the same superposition of $\Delta_{1,\mu}^{(n)}(x)$ and $\Delta_{2,\mu}^{(n)}(x)$ as $\mathcal{F}_{12}$ of $\mathcal{F}_1$ and $\mathcal{F}_2$. The iterations continue until the functional $\mathcal{F}_{12}$ has been maximised, which will be considered to be when Δ_{12} is

sufficiently close to zero,

$$\frac{1}{VN_C}\sum_{\mu}\Delta^{(n)}_{12,\mu} \leq 10^{-12}. \tag{3.42}$$

The exponential in Eq. (3.41) is generally approximated to first order and applied successively to the original gauge field, known as the 'steepest-descents' method. As the functional approaches the maximum, the difference between the gauge transformation and the identity matrix reduces. This makes it difficult to make long-range changes and is known as critical slowing down. This problem can be remedied by employing Fourier acceleration [49] to the gauge transformation. The Fourier transformed gauge transformation is then scaled by a factor inversely proportional to the momentum, then Fourier transformed back to position space. Thus, the iteration condition becomes

$$G^{(n+1)}(x) = \exp\Big(\hat{F}^{-1}\frac{\alpha}{2}\frac{p^2_{\max}}{p^2(\hat{x})}\hat{F}\sum_{\mu}\big(\Delta^{(n)}_{12,\mu}(x) - \frac{1}{3}\mathrm{Tr}\Delta^{(n)}_{12,\mu}(x)\big)\Big), \tag{3.43}$$

where $p^2(\hat{x})$ contains the square of all possible values of lattice momentum, except $p^2 = 0$. This has the effect of increasing the step size of the low momentum, and therefore, slowest converging modes of the gauge transformation. This in turn effectively eliminates the problem of critical slowing down, and can improve convergence time by up to a factor of 4 over a steepest descents algorithm.

A significant part of the work done for this thesis was the modernisation and parallelisation of legacy gauge fixing code. Features such as restartability and the Fourier acceleration algorithm were added and necessary in order to complete this work. Rewriting of code for the existing algorithms provided a factor of 3 increase in overall performance, and up to a factor of 10 in certain subroutines. The implementation of the Fourier acceleration gave a further performance boost of, on average, 50% over the conjugate gradient minimisation algorithm. This, coupled with parallelisation using the MPI2 standard, decreased convergence time per configuration by a factor of over 100 compared to the legacy implementation.

Chapter 4

Smearing Optimisation

Early pion electromagnetic form factor calculations [51, 52] and nucleon form factor calculations [53, 54, 55] established the formalism and presented first results establishing the challenges ahead for obtaining precision form factors to confront experimental data. Nucleon form factors continue to be an active area of research [56, 57, 58, 59, 60, 61, 62, 63] and a comprehensive review of recent form factor calculations can be found in [64] and references therein.

In practice, current lattice calculations were limited to a momentum transfer of approximately $Q^2 = 3\,\mathrm{GeV}^2$ due to a challenge of increasing statistical errors. Recently, calculations of the nucleon and pion form factors at $Q^2 = 6\,\mathrm{GeV}^2$ have been performed using variational techniques [65]. In this thesis we explore very high momentum states and propose that, with sufficient optimisation of the smearing parameters alone, momentum transfers of the order $Q^2 = 10\,\mathrm{GeV}^2$ can be accomplished in lattice hadron structure calculations.

Smearing techniques have seen wide spread use in many applications in lattice QCD since first being applied to fermion operators [24, 25]. The most notable impacts can be found in spectroscopy calculations using variational methods [38, 40, 41, 42, 44, 45]. In spite of these successes, there has been little in the way of the optimisation of smearing parameters for high-momenta states. For low-momenta states there is no real need for optimization as the overlap of states is typically slowly varying with the smearing parameters. In the following we reveal that this is not the case for high-momenta states and finely tuned optimization is very beneficial in accessing these states on the lattice.

Isolation of the ground state at high-momentum is essential to removing oth-

erwise large and problematic excited state contaminations. However, suppression of excited states through Euclidean evolution alone encounters a rapid onset of statistical noise. We introduce two different measures to quantify the coupling of a smeared operator to the ground state of a proton relative to the near-by excited states, and show how these measures determine the optimal smeared operator for ground state isolation early in Euclidean time.

We also introduce anisotropy into the smeared operators in the direction of momentum in an effort to improve the coupling to these Lorentz-contracted high-momentum states. Our results are complementary to the variational techniques of Ref. [65] in that the optimal set of smearings for accessing a variety of momenta can be combined to create a correlation matrix providing an effective basis for eigenstate isolation.

4.1 Techniques

Recalling the discussion from Chapter 2, when calculating the two-point function, it is possible to choose from a set of quantised momenta, given by

$$\vec{p} = \frac{2\pi}{N_S a}(p_x, p_y, p_z) \tag{4.1}$$

and limited to

$$-\frac{N_S}{2} < p_i \leq \frac{N_S}{2}. \tag{4.2}$$

As demonstrated in Section 2.2, the construction of the discrete fermion propagator gives momentum input into the two-point function proportional to $\sin(\vec{p})$, therefore, it is only reasonable to consider momentum states where

$$|\, p_i \,| \lesssim \frac{N_S}{4}, \tag{4.3}$$

such that the dispersion relation is approximately satisfied.

We can introduce anisotropy to the smearing defined in Section 2.3 by introducing a new constant α_x, which will act only in the x direction. The expression

for the smearing then becomes,

$$\begin{aligned} F(x,y) =&(1-\alpha_o)\,\delta_{xy} + \frac{\alpha_x}{6}\left(U_1^\dagger(x-a\hat{x})\,\delta_{x-\hat{x},y} + U_1(x)\,\delta_{x+\hat{x},y}\right) \\ &+\frac{\alpha}{6}\sum_{\mu=2}^{3}\left(U_\mu^\dagger(x-a\hat{\mu})\,\delta_{x-\hat{\mu},y} + U_\mu(x)\,\delta_{x+\hat{\mu},y}\right) \end{aligned} \tag{4.4}$$

where $\alpha_o = 0.7$ and α and α_x are normalised such that

$$\frac{4\alpha + 2\alpha_x}{6} = \alpha_o\,. \tag{4.5}$$

4.2 Measures

Gusken [21] introduced the measure

$$R = \frac{G_2(t')\,e^{+m_0\,t'}}{G_2(0)}\,, \tag{4.6}$$

for quantifying the ground state isolation of a hadron. By taking a point, t', sufficiently late in time such that the excited state contributions become negligible, the ground state can be evolved back to the source via $e^{+m_0\,t'}$ to evaluate the fraction of $G_2(0)$ it holds. However, with sufficient smearing, states can contribute negatively to the two-point function, allowing this ratio to exceed 1 and making it difficult to interpret the results.

The first measure we introduce follows from this idea by determining the deviation of $G_2(t)$ from the ideal two-point function of a single ground state. It is similar in principle to Gusken's measure, however, it is capable of taking into account the presence of states with negative coupling to the operator. The measure M_1 is defined as,

$$M_1 = \frac{-1}{t_f - t_i + 1}\sum_{t=t_i}^{t_f}\frac{\left(e^{-E_0(t-t_0)} - \tilde{G}_2(t)\right)^2}{\tilde{G}_2^2(t)}\,, \tag{4.7}$$

where $\tilde{G}(t) = G(t)/G(t_0)$. The factor -1 makes this measure maximal when $G(t)$ is a pure exponential of the ground state. The energy E_0 is determined from a 4×4 source-sink-smeared variational analysis [43] of the zero momentum state

with the correct dispersion relation applied for finite-momentum states.

Another common method of extracting coupling effectiveness is to perform a four parameter, two exponential fit on a region close to the source of the two-point function, *i.e.*

$$G_{\text{fit}} = a_1 e^{-a_2 t} + b_1 e^{-b_2 t}. \tag{4.8}$$

However, this method tends to prove unreliable with the parameters varying with the fit window. The method is limited by the fact that it can not take into account any states with higher energy than the two considered.

The second measure we introduce works similar to this. However, the parameters of the exponentials are predetermined by a variational analysis [43]. This leads to a simple linear fit of known exponentials, *i.e.*

$$G_{\text{fit}} = \lambda_0 \, e^{-E_0 \, t} + \lambda_1 \, e^{-E_1 \, t} + \lambda_2 \, e^{-E_2 \, t} \, . \tag{4.9}$$

We can then find the proportion of the i-th state in the two-point function with the measure

$$M_{2,i} = \frac{|\, \lambda_i \,|}{\sum_k |\, \lambda_k \,|} \, . \tag{4.10}$$

4.3 Lattice Details

Our calculations are performed on configurations of size $32^3 \times 64$ with a lattice spacing of 0.0907 fm provided by the PACS-CS collaboration [66]. These lattices have $2 + 1$ sea quark flavours generated with the Iwasaki gauge action [67] and the non-perturbatively improved Clover fermion action [16] with the κ values for the light quarks and the strange quark given by 0.13754 and 0.13640 respectively, and $C_{SW} = 1.715$. This gives a pion mass of $m_\pi = 389\,\text{MeV}$.

In order to eliminate any bias caused by smearing in the source, we use a single set of propagators generated with a point source. All of the smearing is then applied to the sink, making the two-point functions smearing dependent. All momentum will be in the x direction, *i.e.* $p_y = 0$ and $p_z = 0$ in Eq. (4.1).

We use a 4×4 correlation matrix to extract our excited state masses, constructed from the χ_1 operator with 16, 35, 100 and 200 sweeps of smearing. We choose to use the larger basis in order to ensure that the first three eigenstate energies are accurately determined.

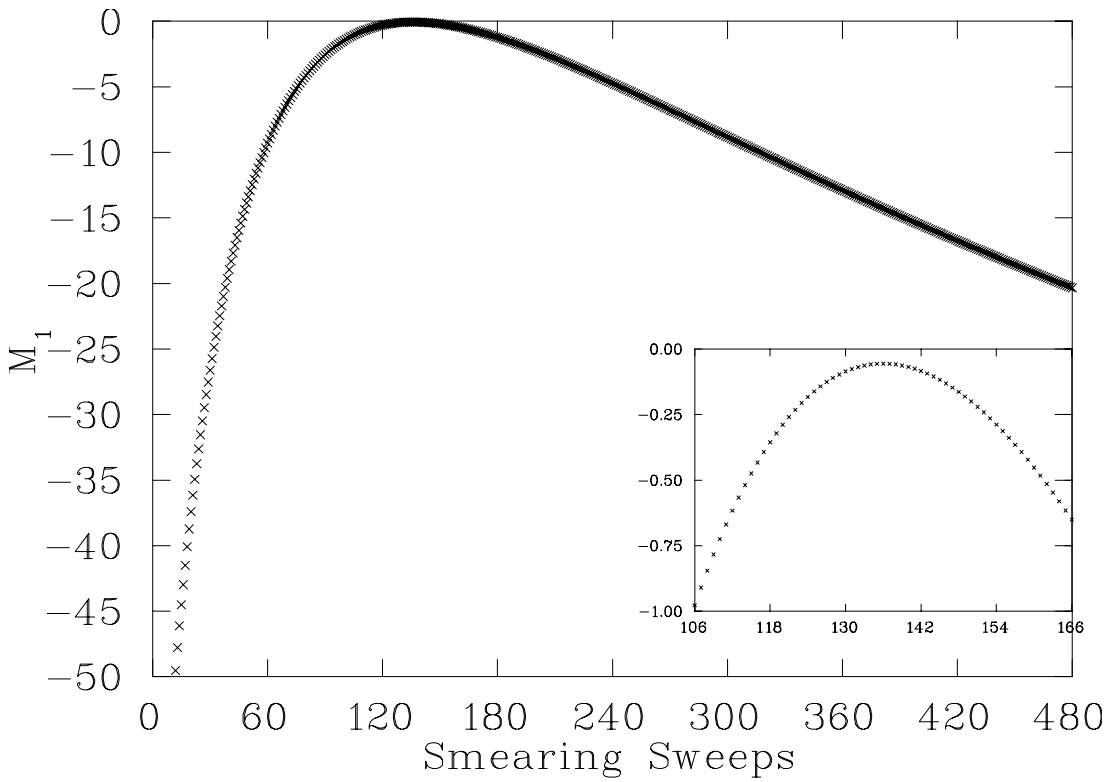

Figure 4.1: The measure, M_1, from Eq. (4.7) at $p_x = 0$ in Eq. (4.1). Deviation from the ideal two-point function increases by a factor of 10 less than 30 sweeps from the ideal smearing level, as shown in the inset graph

We have verified that no multi-particle states are present in the variational analysis by applying the single-particle dispersion relation to the zero momentum effective state masses to successfully predict the effective masses of the same states with non-zero momentum.

Our error analysis is performed with the second-order single-elimination jack-knife method. Linear fits are performed using the normal equations with exact matrix inversion where possible and singular value decomposition otherwise.

4.4 Results

4.4.1 Isotropic Smearing

We first calculate the measure from Eq. (4.7) where the two-point functions have been normalised 1 time slice after the source, with $t_i = 1$ and $t_f = 6$. The two-

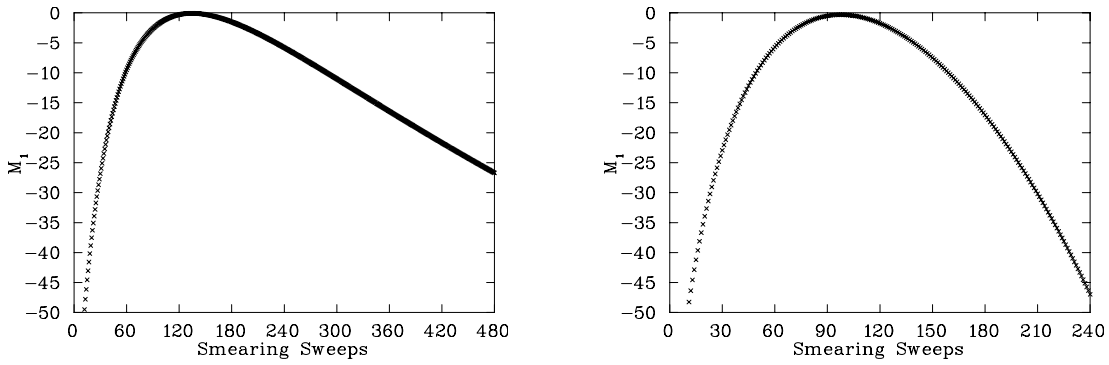

Figure 4.2: M_1 from Eq. (4.7) at $p_x = 1$ (left) and $p_x = 3$ (right) in Eq. (4.1). There is little difference between the measure at $p_x = 0$ and $p_x = 1$, due to the fact that the probability distributions between the two momentum states are nearly identical. At $p_x = 3$, the rms radius of the optimal smearing level is smaller by a factor of 0.85 relative to the $p_x = 0$ state, whereas the relativistic γ factor provides a Lorentz contraction factor of $\gamma^{-1} = 0.72$.

point function is calculated at every sweep of sink smearing between 1 and 480, up to an rms radius of 13.68 in lattice units. For this particular ensemble, the two-point function that shows the highest proportion of ground state has 136 sweeps of smearing at the sink, or an rms radius of 6.92 lattice units as seen in Fig. 4.1. Also apparent is that the effectiveness of the smearing at isolating the ground state is significantly reduced fairly close to the optimal amount of smearing. At only 30 sweeps away from the ideal number of sweeps, the deviation from the ideal two-point function has increased by a factor of 10.

When we move to $p_x = 1$ in Eq. (4.1), which gives momentum in the x direction of 427 MeV, the ideal number of smearing sweeps reduces by just one sweep to 135 (rms radius 6.90 lattice units), as shown in Fig. 4.2. This can be explained by considering the relativistic γ factor, which is given by the ratio of the relativistic energy momentum relation and the ground state mass. The fitted ground state mass for the proton is $M_P = 1.273(21)\,\text{GeV}$, giving a relativistic energy of $E_P|_{p=1} = 1.343(23)\,\text{GeV}$ and $\gamma = 1.05$. Given that all of the excited states are more massive, and therefore exhibit less Lorentz contraction than the ground state, it is feasible that there is very little difference in the probability distribution between this state and the zero momentum state, thus the ideal amount of smearing should be very similar to the zero momentum state.

At $p_x = 3$ in Fig. 4.2, the optimal number of smearing sweeps has decreased to

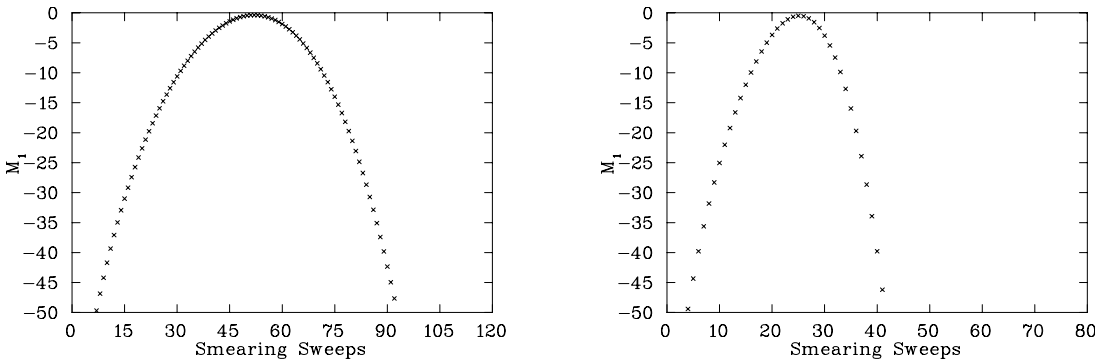

Figure 4.3: M_1 from Eq. (4.7) at $p_x = 5$ (left) and $p_x = 7$ (right) in Eq. (4.1). The value of the measure at the optimum number of smearing sweeps for this momentum state is approximately equal to that of the $p_x = 3$ state, indicating that good ground state isolation is possible even at higher momenta. At $p_x = 7$, the deviation from the ideal two-point function has increased by a factor of 10 only 5 sweeps from the optimal smearing level, as shown in the inset graph.

98. The maximum value of the measure has also decreased relative to the lower momentum states, indicating relatively more excited state contamination, though still achieving good isolation. The ratio of the rms radius of the optimal smearing for this state to the optimal smearing for the ground state is 0.85, compared to the relativistic γ^{-1} factor of 0.72. At $p_x = 5$, corresponding to a momentum transfer of approximately $4.55\,\mathrm{GeV}^2$, shown in Fig. 4.3, the optimal number of sweeps is 52 (rms radius 4.27 lattice units). However, the maximum value of the measure is close to the maximum value for the $p_x = 3$ case, indicating that very efficient isolation is possible, even at larger momentum transfers.

Moving to $p_x = 7$, equivalent to a momentum transfer of $8.93\,\mathrm{GeV}^2$, there is significant noise far from the source in the two-point function, even for highly optimised smearing values. Hence we consider $t_f = 5$ in the measure from Eq. (4.7) at this value of momentum. The ideal number of sweeps decreases to 27 sweeps, or 3.08 lattice units rms radius, seen in Fig. 4.3. Notably, the deviation from the ideal two-point function increases by a factor of 10 only 5 sweeps from this optimal value, corresponding to a change in rms radius of less than 0.3 lattice units.

Using the measure described in Eq. (4.10), we first consider the three exponential fit between time slices 1 and 6 after the source with masses 1.273(21) GeV, 2.301(28) GeV and 2.786(95) GeV as determined in our correlation matrix anal-

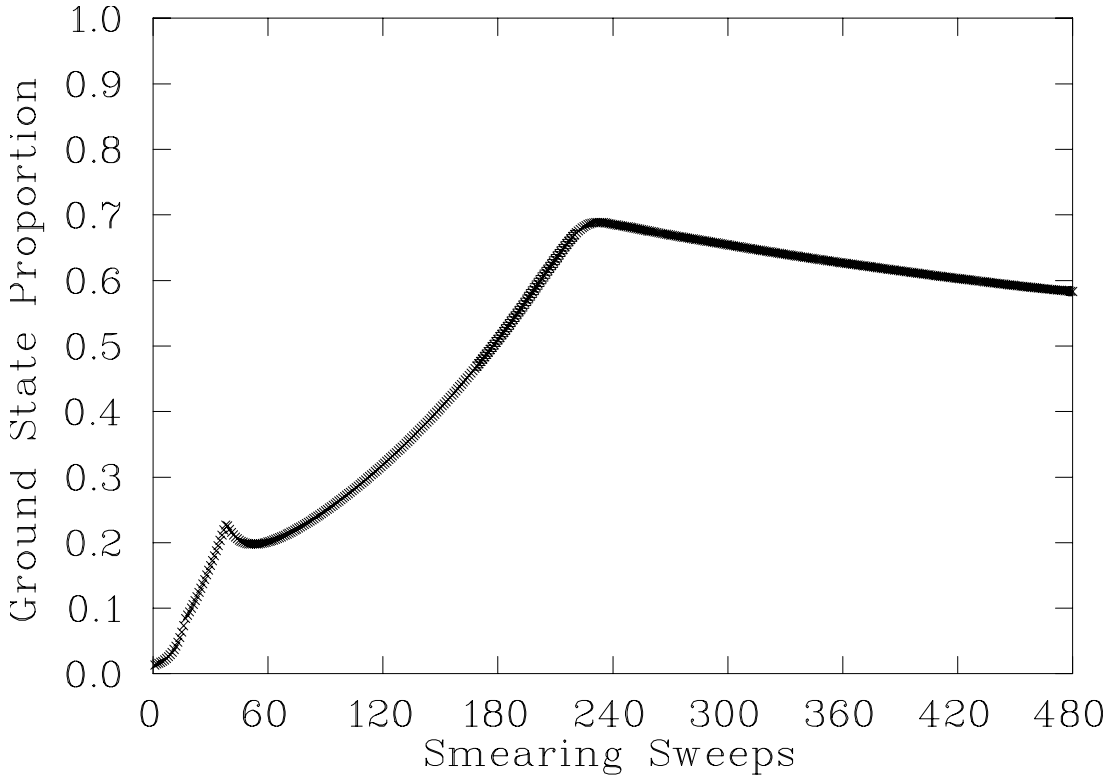

Figure 4.4: Ground state proportion from the three exponential fit, *i.e.* M_2 from Eq. (4.10) where $k = 3$ and $i = 1$ at $p_x = 0$ in Eq. (4.1). There is insufficient information on the second excited state close to the optimal amount of smearing, thus requiring use of the two exponential fit, $k = 2$, to determine the optimal amount of smearing with M_2.

ysis. From the results for $p_x = 0$ in Fig. 4.4, we can see that, in the region where the first measure predicts ideal smearing levels, there is a sharp change in the structure of the graph. In order to determine the cause of this, we compare with the fits containing only the ground and first excited states. Fig. 4.5 shows that the optimal number of smearing sweeps lies close to the value predicted by the first measure. The overlap at the optimal number of sweeps, 138 in this case, is 99.31(8)%, indicating that, in the three exponential fit, we are attempting to fit two quickly decaying exponentials using only 0.69% of the signal available. This leads us to believe that, in the regions of ground state dominance where we are most interested, the coefficient from the quickly decaying third state cannot be determined accurately, therefore dominates well beyond where it should be allowed to contribute at all. For this reason, we will only consider fits using the ground and first excited states.

The contamination due to excited states in the two exponential fit at zero momentum increases rapidly away from the optimum smearing level. Of the smearing sweeps used to extract the masses from the variational analysis, the one that shows the most overlap with the ground state is 200 sweeps, or an rms radius of 8.55 lattice units, with 77.69(7)%, or 32 times more excited state contamination than the optimal smearing level.

At the first non-zero momentum state, the results present similarly to the first measure, the optimal amount of smearing is 1 sweep less than that of the non-zero momentum ground state, and 2 sweeps more than the optimal amount determined by the first measure. At $p_x = 3$ in Eq. (4.1) shown in Fig. 4.6, the overlap is maximised at 101 sweeps of smearing, or an rms radius of 5.95 lattice units, once again agreeing within only a few sweeps of the optimum level suggested by the first measure. Remarkably, considering the use of a point source, the proportion of ground state present at this optimal amount of smearing is 98.87(12)%.

At $p_x = 5$ and $p_x = 7$ in Fig. 4.7 there is again good agreement between the two measures, with the optimal smearing level being 53 and 26 sweeps respectively. Even at a momentum transfer of $8.93\,\mathrm{GeV}^2$, 97.20(20)% overlap is achieved with the ground state, and once again, very few sweeps from the optimum level, the overlap drops dramatically. At $p_x = 7$, there is a second peak far from the optimal number of smearing sweeps, it is unlikely that any highly Lorentz contracted state would couple to such a large sink. The second peak in Fig. 4.7 can therefore be

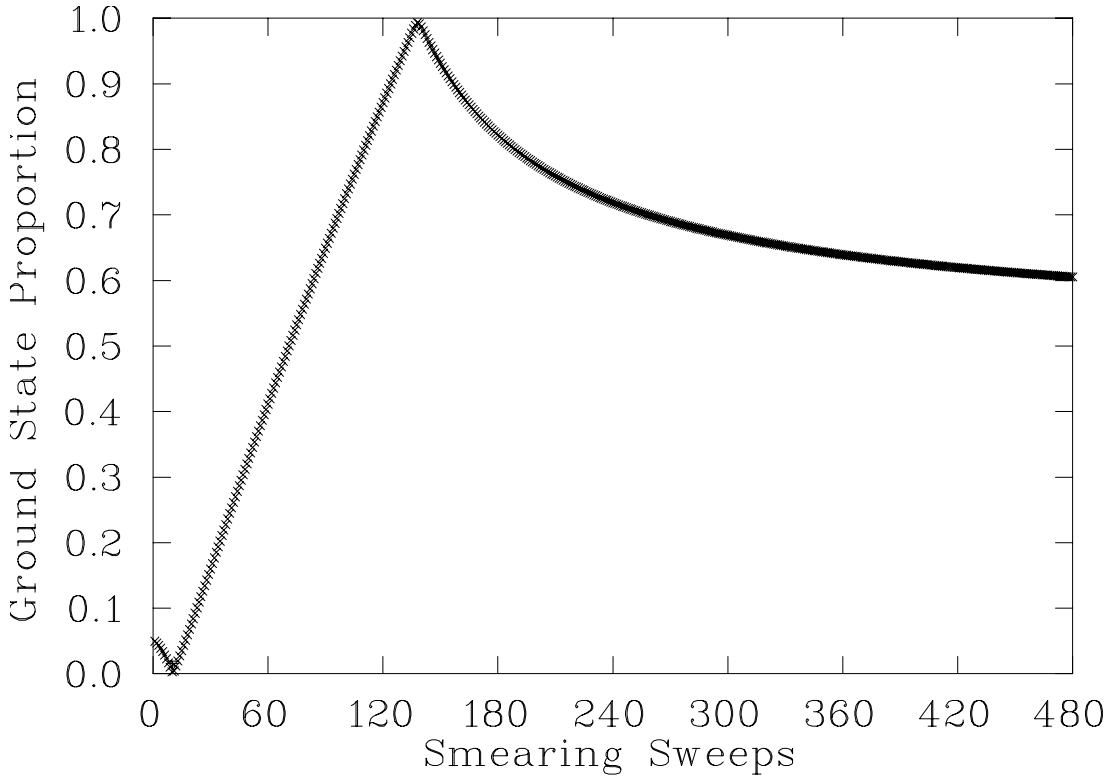

Figure 4.5: Ground state proportion for the two exponential fit, M_2 with $k = 2$ and $i = 1$ in Eq. (4.10) at $p_x = 0$ in Eq. (4.1). Contamination due to excited states increases rapidly away from the optimal smearing level. There is good agreement between the two exponential fit here and the three exponential fit in Fig. 4.4 away from the optimum smearing levels.

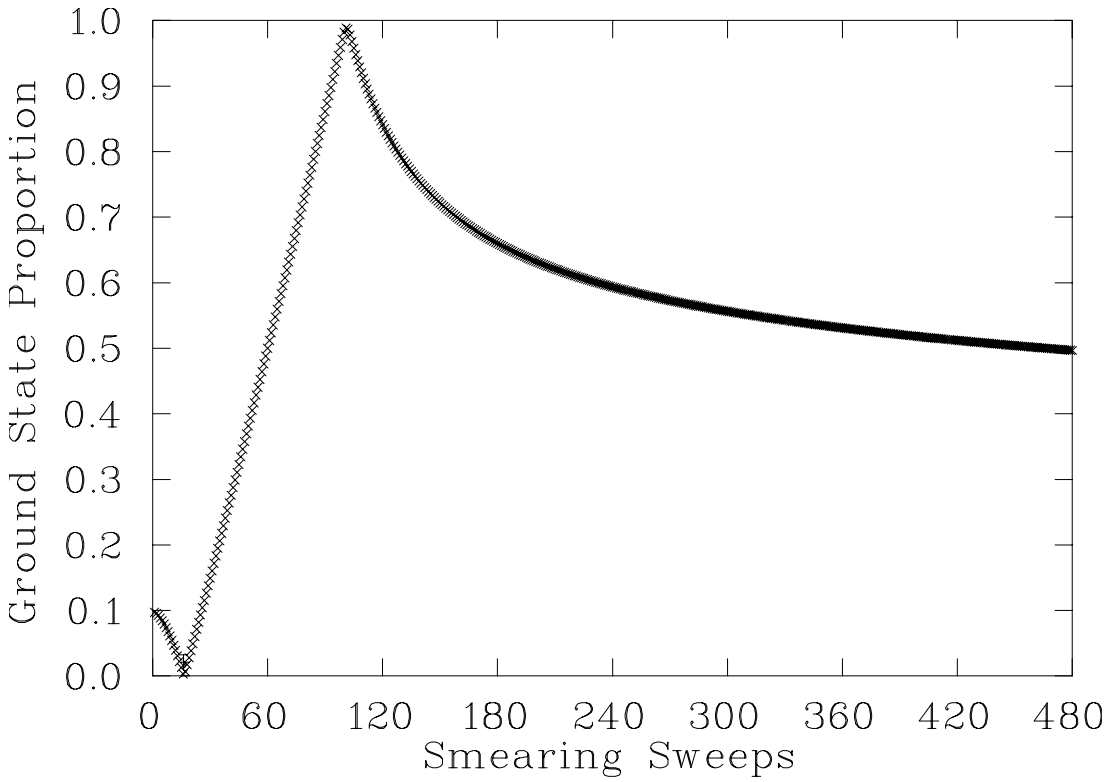

Figure 4.6: Ground state proportion according to M_2 at $p_x = 3$ in Eq. (4.1). As momentum increases, the contamination due to excited states increases more rapidly away from the ideal smearing level.

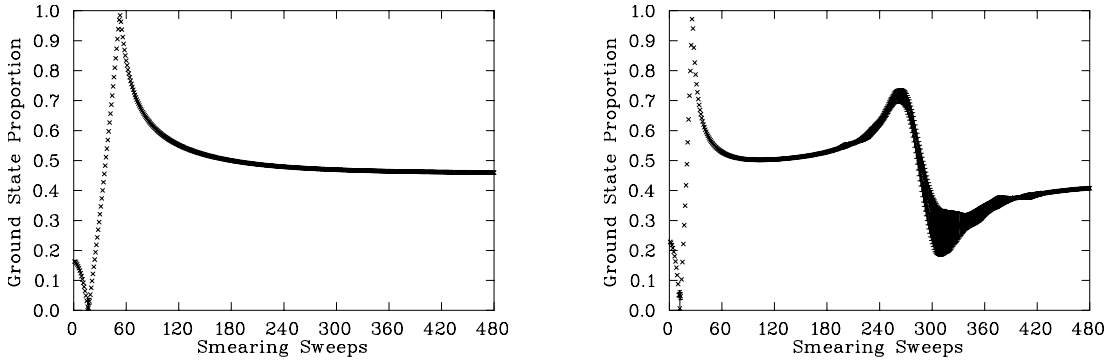

Figure 4.7: Ground state proportion according to M_2 at $p_x = 5$ (left) and $p_x = 7$ (right) in Eq. (4.1) Even at these very high momentum transfers, good overlap with the ground state is achieved for an optimised sink. Far from the optimal number of smearing sweeps at $p_x = 7$, it is clear that the measure is no longer applicable, as there would be little, if any highly Lorentz contracted ground state present.

considered to signify a limit to the domain of validity of the measure. Table 4.1 summarises the ideal number of smearing sweeps for both measures at each of the momenta studied.

Table 4.1: The ideal number of smearing sweeps found for each measure and momenta investigated.

p_x	γ^{-1}	M_1 ideal sweeps	M_2 ideal sweeps
0	1	136	138
1	0.95	135	137
3	0.72	98	101
5	0.51	52	53
7	0.39	27	26

4.4.2 Anisotropic Smearing Results

As anisotropy is introduced to the smearing as described in Eq. (4.4), we consider the first measure from Eq. (4.7) at the first non-zero momentum state and find that there is no improvement to the ground state isolation, as shown in Fig. 4.8. There is, however, an ideal number of sweeps that increases for decreasing α_x that shows approximately equal ground-state proportion relative to the isotropic smearing case, that is $\alpha_x = \alpha = 0.7$.

At $p_x = 3$ in Eq. (4.1), in spite of the clear difference in the smearing sweeps required to maximise overlap with the source, Fig. 4.9 shows that introducing anisotropy to the smearing does not result in improved isolation of the ground state. The structure of the curve is similar to that of the $p_x = 1$ state, where there is an optimal number of sweeps for every value of α_x which increases with decreasing α_x.

Once again, there is no improvement in the ability of anisotropic smearing to isolate the ground state at the momentum of $p_x = 5$, as shown in Fig. 4.10. The structure revealed in the lower momentum states persists for this state and for the $p_x = 7$ state in Fig. 4.11. From these results, optimisation of the number of smearing sweeps alone is sufficient to achieve good isolation of the ground state of the two-point function at a range of momenta.

We now investigate how anisotropic smearing affects the signal-to-noise ratio

or quality of the two-point function at high momenta. Since we have ensured that the ground state is isolated as close to the source as possible, we now determine the quality of the signal a few time slices away from the source. We consider the relative error of the two-point function four time slices after the source at the optimal number of smearing sweeps for each value of our anisotropy parameter, α_x.

For $p_x = 3$, Fig. 4.12 shows the relative error in the two-point function at $t = 4$. The smallest relative error occurs when the smearing is isotropic. Increasing the momentum to $p_x = 5$ lattice units shows that there is only a small improvement to the relative error for values of $\alpha_x \sim 0.48$. It is worth noting that the first of the minima visible in Fig. 4.13 at $\alpha_x = 0.36$ corresponds to the anisotropy expected due to Lorentz contraction as $\alpha_x/\alpha = 0.51$ equals $\gamma^{-1} = 0.51$.

The banding structure visible in Fig. 4.13 is a result of the optimal number of smearing sweeps increasing for decreasing values of α_x. Each discontinuity in the graph for $\alpha_x > 0.36$ is the result of the optimal number of smearing sweeps decreasing by 1. It is an artifact resulting from the density of the points in α_x being much finer than the density of the points in the number of smearing sweeps.

Moving to $p_x = 7$ in Fig. 4.13 we see a distinct improvement in the correlation-function relative error when anisotropy is introduced. Both $\alpha_x = 0.26$ and 0.32 provide a 10% reduction in the error relative to that observed at the isotropic value of 0.7. The values of $\alpha_x \simeq 0.26$ to 0.32 provide $\alpha_x/\alpha = 0.37$ to 0.46, in accord with the value of $\gamma^{-1} = 0.39$ predicted by Lorentz contraction.

4.5 Summary

We have presented two new measures of the effectiveness of smeared operators in isolating the ground state of a hadron in the two-point function. Both measures show good agreement with each other. We have performed a detailed analysis of ground state isolation with each measure and have shown that optimisation of the smearing can lead to remarkable improvement to the ground state isolation. Furthermore, the ability to isolate the ground state decreases dramatically a few sweeps from the optimal number of smearing sweeps for the higher momentum states. In selecting a basis for a correlation matrix analysis, these optimal smearing parameters are preferred.

On the introduction of anisotropy to the smearing, we found that there was no appreciable improvement to the overlap with the ground state. The relative proportion of the ground state for an isotropic source is already high. Optimising the number of sweeps of isotropic smearing alone is sufficient to ensure maximal isolation of high-momentum ground states. The introduction of anisotropy does provide a small improvement to the correlation function of high-momentum states a few Euclidean time slices after the source.

Our results indicate that future studies of high-momentum states should adopt this relatively cheap program of tuning the smearing parameters to optimize isolation and overlap with the states of interest. We anticipate this approach will be of significant benefit in future form factor studies.

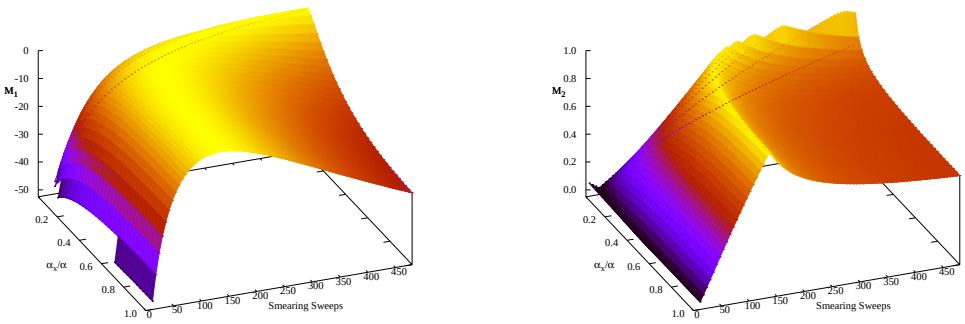

Figure 4.8: The first measure, M_1 ,from Eq. (4.7) (left) and the Ground State Proportion (right) with anisotropic smearing at $p_x = 1$ from Eq. (4.1). Introducing anisotropy to the smearing does not improve the isolation of this state. However, the Lorentz contraction is small so little improvement would be expected.

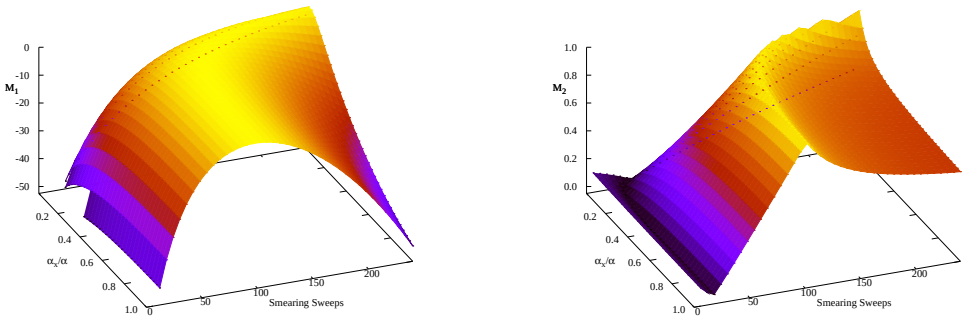

Figure 4.9: The first measure, M_1, from Eq. (4.7) (left) and the Ground State Proportion (right) with anisotropic smearing at $p_x = 3$ from Eq. (4.1). No improvement is seen in the isolation of the ground state, in spite of the relativistic γ factor of 1.39 giving a length contraction factor of 0.72 in the x direction.

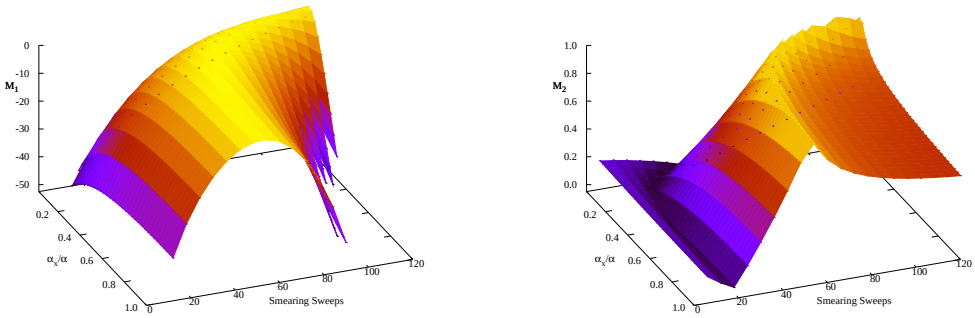

Figure 4.10: The first measure, M_1, from Eq. (4.7) (left) and the Ground State Proportion (right) with anisotropic smearing at $p_x = 5$ from Eq. (4.1). The structure observed in the plots of the $p_x = 3$ state is retained, with more sweeps of smearing required as anisotropy is increased.

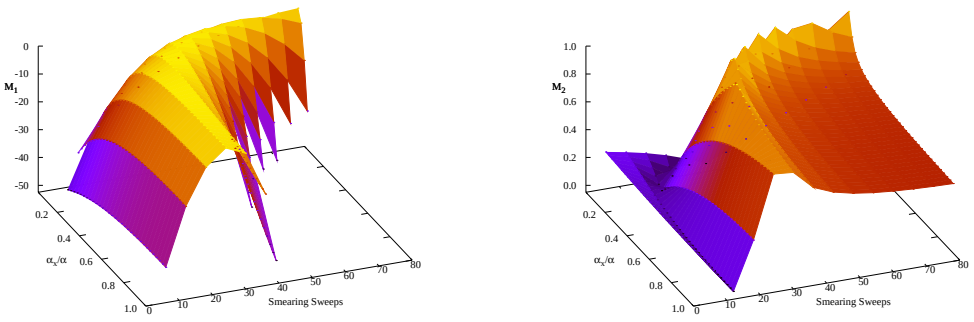

Figure 4.11: The first measure, M_1, from Eq. (4.7) (left) and the Ground State Proportion (right) with anisotropic smearing at $p_x = 7$ from Eq. (4.1). Even at a momentum of 2.99 GeV, anisotropy in the smearing does not improve isolation of the ground state.

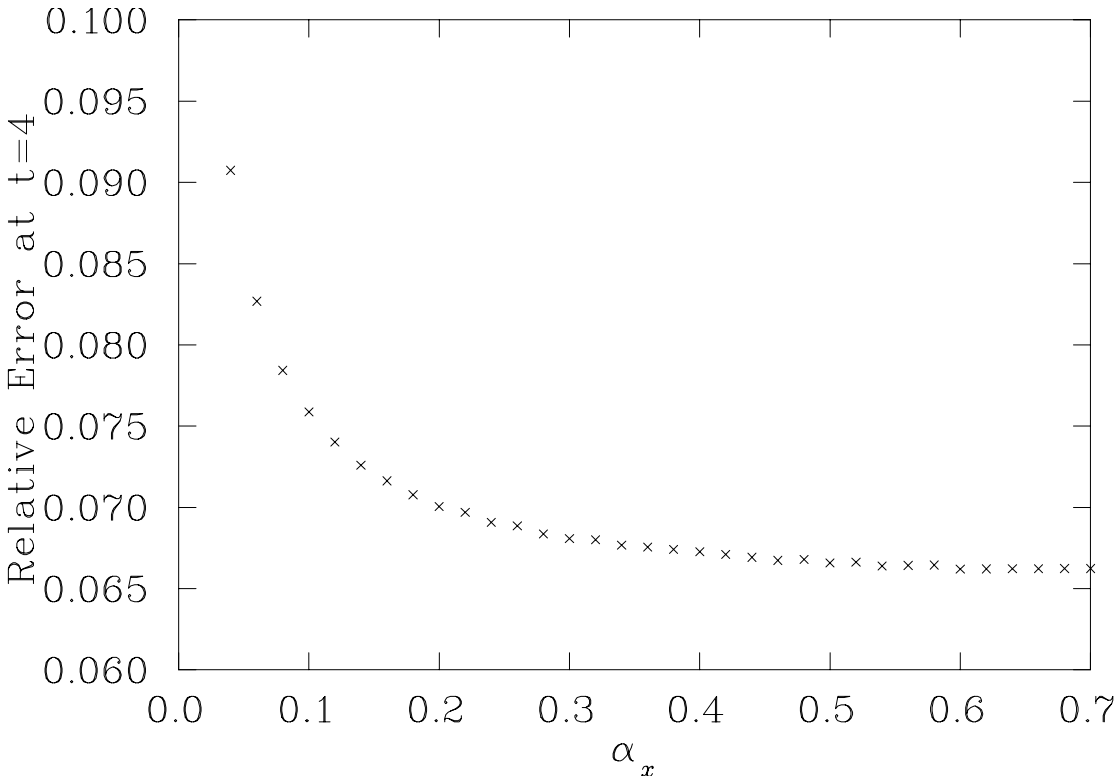

Figure 4.12: The size of the relative error in the two-point function measured four time slices after the source for $p_x = 3$ as in Eq. (4.1). At this momentum, the two point functions displaying the smallest relative error were created with an isotropic source.

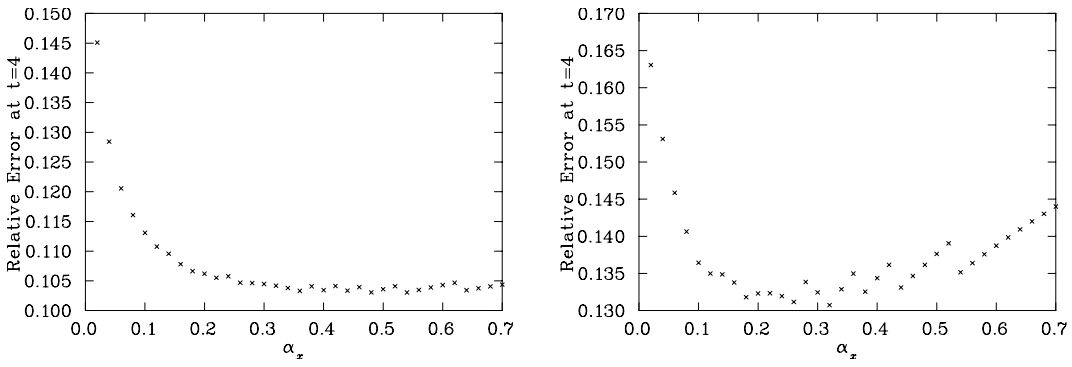

Figure 4.13: The size of the relative error in the two-point function measured four time slices after the source for $p_x = 5$ (left) and $p_x = 7$ (right) as in Eq. (4.1). At $p_x = 5$, there is a small amount of improvement for anisotropic smearing at α_x/α in the region of $\gamma^{-1} = 0.51$. At $p_x = 7$, improvement in the relative error is seen for values of $\alpha_x \simeq 0.26$ to 0.32 where $\alpha_x/\alpha = 0.37$ to 0.46, in accord with the value of $\gamma^{-1} = 0.39$ predicted by Lorentz contraction. Note that the emergent banding structure reflects a change in the optimal number of smearing sweeps by one.

Chapter 5

Quenched QCD Wave Functions

The earliest work on wave functions on the lattice was carried out on small lattices, for the pion and rho, initially in $SU(2)$ [35]. Further progress was made in the early nineties, where gauge invariant Bethe-Salpeter amplitudes were constructed for the pion and rho [34, 36] by choosing a path ordered set of links between the quarks. This was then used to qualitatively show Lorentz contraction in a moving pion. Hecht and DeGrand [37] conducted an investigation on the wave functions of the pion, rho, nucleon and Delta using a gauge dependent form of the Bethe-Salpeter amplitude, primarily focusing on the Coulomb gauge.

The background field method [27] for placing an external electromagnetic field on the lattice has been used extensively in lattice QCD to determine the magnetic moments of hadrons. Early studies on very small lattices with only a few configurations [30, 31] showed remarkable agreement with the experimental values of the magnetic moments of the proton and neutron. More recent studies on magnetic moments [32] have shown good agreement with experimental values of the magnetic moments of the baryon octet and decuplet. This method has also been extended to the calculation of magnetic and electric polarisabilities [28, 33]. Here we use the wave function to determine the effect of the background magnetic fields on the shape of the proton.

As background field methods have become more widely used, it is apparent that the large fields demanded by the quantisation conditions should cause some concern with regards to the calculation of moments and polarisabilities. It is entirely possible that the distortion caused by these fields could be so dramatic that the particle under investigation bears little resemblance to its zero-field form. For

this reason, we will use the wave function as a tool to investigate the deformation caused by a background field on a particle.

5.1 Simulation Details

Following the wave function formalism laid out in Section 3.3, we will investigate the effects of a magnetic field on the wave function of the nucleon. The magnetic field is placed on the lattice using the background field formalism described in Section 2.4. We use an ensemble of 200 quenched configurations with a lattice volume of $16^3 \times 32$, generated using the Luscher-Weisz $\mathcal{O}(a^2)$ improved gauge action [5], described in Section 2.1. The $\mathcal{O}(a)$ improved FLIC fermion action [68], Section 2.2, is used to generate the quark propagators with fixed boundary conditions in the time direction. Four sweeps of stout link smearing [26], described in Section 2.3, with smearing parameter $\rho = 0.1$ are applied to the gauge links in the irrelevant operators of the FLIC action. We use $\beta = 4.53$, corresponding to a lattice spacing of $a = 0.128\,\text{fm}$, determined by the Sommer parameter, $r_0 = 0.49\,\text{fm}$ [3]. We employ 50 sweeps of gauge invariant Gaussian smearing [21] to the fermion source at time slice 8. Two values for the hopping parameter are considered, $\kappa = 0.12885$ and 0.12990, corresponding to pion masses of $0.697\,\text{GeV}$ and $0.532\,\text{GeV}$. The gauge fields generated are fixed to the Landau gauge using the conjugate gradient Fourier acceleration method for improved actions [49], to an accuracy of 1 part in 10^{12}. The normalisation chosen for the wave function is to scale the raw correlation function data such that the sum (over $\vec{x}$ and the parameter associated with the quark wave function coordinate) of the square of the correlation function is 1 for each Euclidean time, t. For the d quark, this is given by Eq. (3.27) and similarly for the u quarks. The wave functions of other quark separations are then scaled by the same factor, $\xi(t)$. In reporting our results, we focus on the probability distribution,

$$\rho_{\gamma\delta} = \xi^2(t)\frac{1}{V}\sum_{\vec{x}} G^{\star}_{\gamma\delta}(\vec{x},\vec{y},\vec{z},\vec{w},t)G_{\gamma\delta}(\vec{x},\vec{y},\vec{z},\vec{w},t), \tag{5.1}$$

where γ and δ are the previously suppressed Dirac indices of the wave function defined in Eq. (3.25). For the zero field case, we report the probability distribution from the average of spin-up, $(\gamma,\delta) = (1,1)$ and spin down, $(\gamma,\delta) = (2,2)$

correlators. For finite $\vec{B}$, spin up and spin down probability distributions are reported individually. The time t is selected to lie well within the ground state dominant regime as identified by a standard covariance-matrix analysis of the local two-point function.

5.2 Zero-Field Results

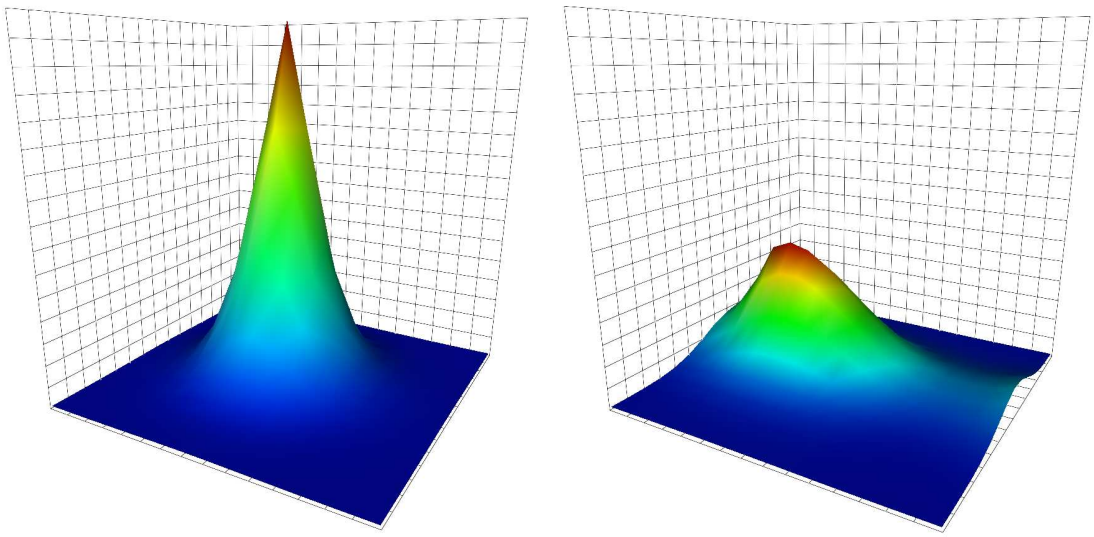

Figure 5.1: The Landau gauge probability distribution for the d quark of the proton from Eqs. (3.25) and (5.1), in the plane of the u quarks separated by zero lattice units (left), and by seven lattice units (right). The d quark is seen to prefer to reside near the u quark which is placed in the scalar pair in the χ_1 interpolating field of Eq. (3.24).

We begin by looking at the probability distribution of the d quark with the aforementioned u quark separations in the Landau gauge. Immediately we notice that the probability distribution is not symmetric around the centre of mass of the proton. We note that in Fig. 5.1, the peak is centred around the u quark that resides in the scalar pairing with the d quark in Eq. (3.24). This leads us to believe that the u and d quarks tend to form a scalar pair within the proton. At this point, we choose to anti-symmetrise the identical u quarks, changing our

annihilation operator from Eq. (3.24) to

$$\chi_P(\vec{x},\vec{y},\vec{z},\vec{w}) = \epsilon^{abc}(u_a^T(\vec{x}+\vec{y})C\gamma_5 d_b(\vec{x}+\vec{z}))u_c(\vec{x}+\vec{w}) + \epsilon^{abc}(u_a^T(\vec{x}+\vec{w})C\gamma_5 d_b(\vec{x}+\vec{z}))u_c(\vec{x}+\vec{y}). \tag{5.2}$$

This choice is motivated by the fact that the interpolating field places one of the u quarks permanently within the scalar pair, however, physically, this would not be the case, as the u quarks within the proton should be indistinguishable.

Upon implementing this symmetrisation, we see no evidence that diquark clustering is occurring at small u-quark separations. Rather, the probability distribution broadens and flattens around the centre of mass of the system. However, when we move to a separation of five or more lattice units, or 0.640 fm, we see the formation of two distinct peaks as illustrated in Fig. 5.2. At this stage, the u quarks are separated further than was considered in [37].

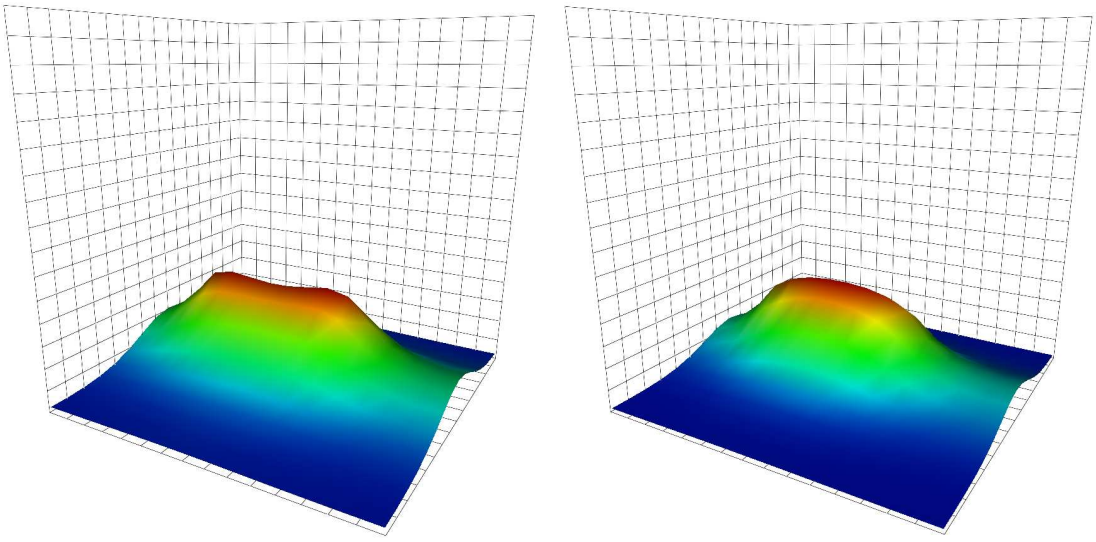

Figure 5.2: The probability distribution for the d quark of the proton in the plane of the u quarks separated by 7 lattice units, in the Landau gauge (left), and the Coulomb gauge (right). Two distinct peaks have formed over the location of the u quarks in the Landau gauge probability distribution, whereas a single, broad peak is visible over the centre of mass of the system in the Coulomb gauge. Note: as discussed following Eq. (3.27) the scale is such that the largest value of all of the fixed quark separations will sit at the top of the grid, with all other points of the probability distribution scaled accordingly.

To more clearly illustrate this double peaked structure, we plot values of the probability distribution along the line joining the two fixed quarks in Fig. 5.3. We have taken advantage of correlations in the uncertainties in the lattice results and present the uncertanty relative to the value at $x = 6$.

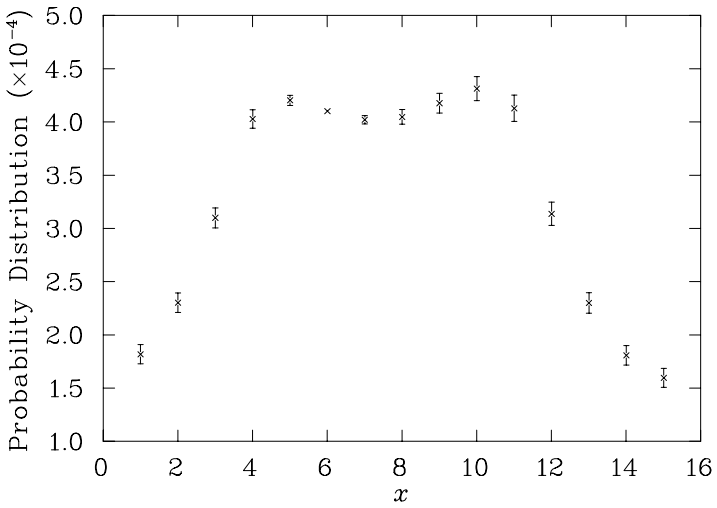

Figure 5.3: The probability distribution of the d quark in the proton with the u quarks 7 lattice units apart along the x axis at $x = 4$ and 11. To clearly display the double peak structure, uncertanties are reported relative to the distribution at $x = 6$.

In the Coulomb gauge, diquark clustering is present as evidenced in the unsymmetrised wave function, however, the support in the centralized region hides the diquark clustering upon anti-symmetrisation. Fig. 5.2 illustrates results for u quarks separated by 7 lattice units. Such a difference in the probability distribution between the two gauges is a remarkable result.

In both the Landau and Coulomb gauges, the mass dependence of the probability distributions is almost negligible, as there are no significant differences in the shape of the probability distribution when the quark mass is changed. This was also noted in Refs. [35, 36]

When we look at the probability distribution of the scalar u quark (i.e. the u quark in the scalar pair with the d quark in Eq. (3.24)) diquark clustering becomes more pronounced in the Landau gauge, as well as becoming apparent in the Coulomb gauge as illustrated in Fig. 5.4.

The probability distribution of the vector u quark (i.e. the u quark that carries

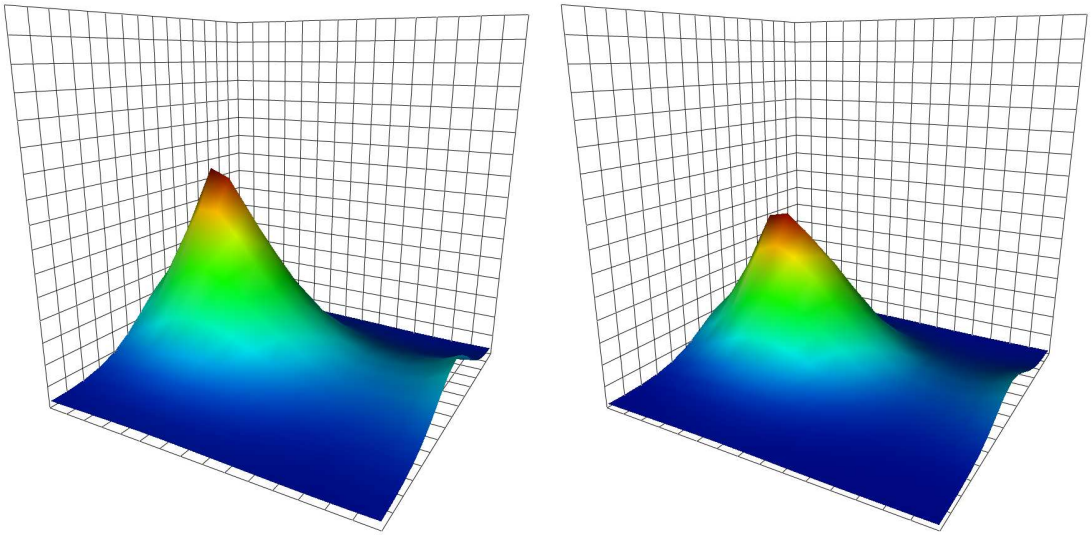

Figure 5.4: The probability distribution for the scalar u quark of the proton in the plane of the u and d quarks separated by seven lattice units, in the Landau gauge (left), and the Coulomb gauge (right). In both gauges, the u quark is seen to prefer to be nearer the d quark, which is to the left of the centre of each lattice. However, in the Coulomb gauge, the scalar u quark is closer to the centre of the lattice than in the Landau gauge probability distribution. The scale is as described in Fig. 5.2

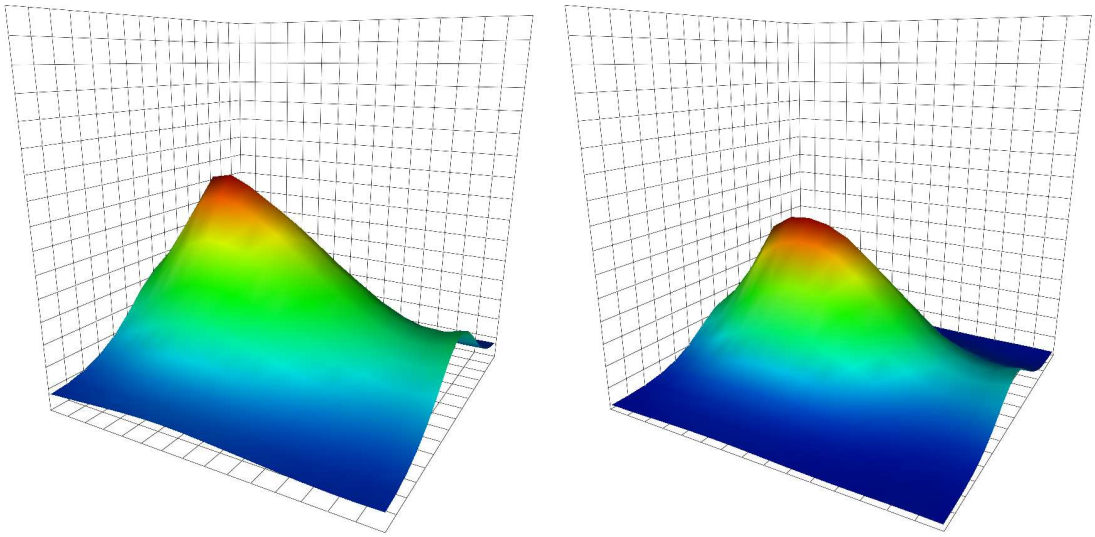

Figure 5.5: The probability distribution for the vector u quark of the proton in the plane of the u and d quarks separated by seven lattice units, in the Landau gauge (left), and the Coulomb gauge (right). The probability distribution presents similarly to the d quark probability distribution in that strong clustering is seen in the Landau gauge. The Coulomb gauge results here reveal a small amount of preferred clustering with the d quark, which is to the left of the centre of each lattice. Also of note is that these probability distributions show less structure than the others, as can be seen by the height of the smallest values, with the scale as described in Fig. 5.2

the spinor index of χ_P in Eq. (3.24)) in the Landau gauge also exhibits diquark clustering without a direct spin correlation in the interpolating field. Such a clustering is anticipated in constituent quark models with hyperfine interactions. Clustering is also observed in the Coulomb gauge. However, much like the d quark, the probability distribution is more towards the centre of mass of the system (Fig 5.5).

While it is possible to classify three types of quark probability distribution, including the d quark, scalar u quark and vector u quark probability distributions, the scalar u quark and vector u quark probability distributions are not physical quantities as the two u quarks in the proton are identical particles. The proper u quark probability distribution can be obtained from the same anti-symmetrised interpolating field of Eq. (5.2). In spite of the symmetrisation, the u quark allowed to vary prefers to reside near the d quark rather than the fixed u quark as illustrated in Fig. 5.6.

The probability distribution of the scalar u quark of Fig. 5.4 very closely resembles that of the symmetrised operator, indicating that the scalar term contributes the most to the symmetrised probability distribution of Fig. 5.6

We note that there are several reasons that we are able to see diquark clustering in the Landau gauge where Ref. [37] did not. Our use of a large smeared source, the averaging over $\vec{x}$ in Eq. (3.25), using improved actions for both the quarks and the gauge fields and the consideration of hundreds of gauge fields provides better statistics, allowing access to further u quark separations with a high signal-to-noise ratio, as well as the ability to investigate lighter quark masses. Furthermore, our lattices extend twice as far in the temporal direction and use fixed boundary conditions, thus reducing the chance of any contamination associated with the boundary conditions.

Although models featuring diquarks within hadrons have been used extensively for many years [69], there has been little, if any, direct evidence for the existence of such a cluster within a particle. Earlier lattice studies that have paired two light quarks with a static quark [70, 71] have shown a large diquark ($\mathcal{O}(1)$ fm) can form inside of a baryon, though with limited effect on the structure of the particle. More recently, light quarks have been paired with various diquark correlators [72] which suggest that diquarks are not a significant factor in light baryons. To the best of our knowledge, this is the first time that such a diquark

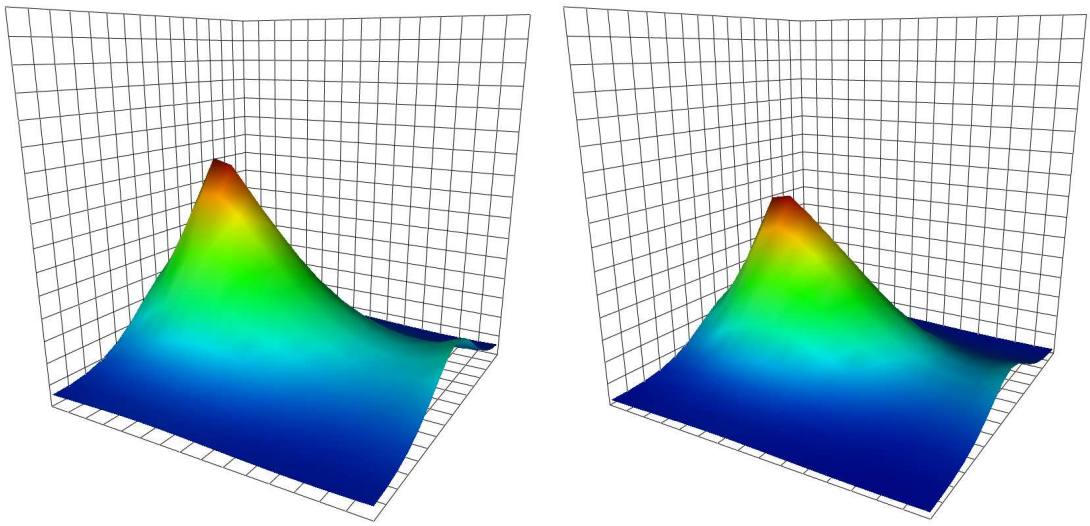

Figure 5.6: The probability distribution for an anti-symmetrised u quark of the proton in the plane of the remaining quarks which are separated by 7 lattice units, in the Landau gauge (left), and the Coulomb gauge (right). In contrast to the d quark probability distribution, a single peak is visible above the location of the d quark (left of centre on each lattice) in both the Coulomb and the Landau gauge. Note: as discussed following Eq. (7) the scale is such that the largest value of all of the fixed quark separations will sit at the top of the grid, with all other points of the probability distribution scaled accordingly.

configuration has been shown in a baryon composed of three light quarks.

5.3 Background Fields on the Lattice

Further to the material presented in Section 2.4, there are several points to note about placing a background field on the lattice, the first of which is that adding any constant to the potential will not affect the resultant field. It can also be shown that there is a gauge transformation that links both of the above implementations of a constant background field in the z direction, given by,

$$G(x, y) = e^{ieBxy}, \tag{5.3}$$

where x, y denote lattice sites $1, 2, \ldots, N_x, N_y$ in units of the lattice spacing a and

$$U_\mu(x) \to G(x)U_\mu(x)G^\dagger(x + \hat{\mu}). \tag{5.4}$$

These implementations of the background field are applied to both the Landau and Coulomb-fixed configurations.

We expect that this magnetic field will cause a distortion of the probability distribution, as the proton responds to the presence of the field. Since the magnetic field is in the z direction, we expect that physical distortion will be symmetric about this direction, and all other effects will be a result of the choice of the gauge potential $\vec{A}$.

A particle on the lattice in the presence of a background magnetic field will undergo a mass shift given by Eq. (3.12). Due to the quantisation imposed by the periodic boundary conditions and the relatively small size of these lattices, the magnetic field will be very large. For $n = 3$ in the quantisation conditions in Eq. (2.79), which the smallest value that can accommodate the fractional charges of the quarks, the value of the field on our lattices is $eB = 0.175$ GeV^2, which implies that the first order response of a proton to the field would be $\mu B = 260$ MeV in the continuum. On the lattice however, the mass of the ground state of the proton is larger and the moment itself is smaller[32], and as such the response will be smaller at approximately 150 MeV at our lighter mass.

5.4 Background Magnetic Field Results

The first notable result from the use of the aforementioned method of placing a background field on the lattice is that an asymmetry is produced in the direction of the changing vector potential as illustrated in Fig. 5.7. This asymmetry occurs in both the Landau gauge and Coulomb gauge to a similar extent. This is an unphysical result of the gauge-dependent method in which we place the field on the lattice, which can be shown by using the second implementation described in Section 5.3. Upon doing this, the asymmetry in the probability distribution can be seen to move to the direction of the vector potential once again as shown in Fig. 5.7. In order to minimise the effect of the choice of gauge potential on the probability distribution, we choose an average over four implementations of the background field. The two implementations described above and two in which a gauge transformation is applied such that the magnitude of the vector potential decreases across the lattice. For the first implementation

$$G(x, y) = e^{iaeBN_x y}, \tag{5.5}$$

and similarly for the second of the two implementations. Once averaging over the four vector potentials has been applied, symmetry around the z-axis is obtained. Thus, we look at the probability distribution in the xz-plane.

In spite of the very large magnetic field strength imposed by the boundary conditions, the change in the probability distribution is quite small for the case where the remaining quarks are both located in the centre of the lattice, (Fig. 5.8). This subtle result is consistent with that expected from the polarisablilty as the current experimental value for the proton polarisability is $\beta_M = 1.9(5) \times 10^{-4}\,\mathrm{fm}^3$ which gives the second order response to the field of around, $\frac{1}{2}\beta_M e^2 B^2 = 40\,\mathrm{MeV}$.

Very little spin dependence can be seen in the probability distributions themselves, the probability distributions of the spin up proton quarks are largely the same as the probability distributions of the spin down proton. A subtle difference appears in the vector u quark probability distributions in the Coulomb gauge, as illustrated in Fig. 5.9. A more prominent difference is visible in the Landau gauge (Fig. 5.10). The probability distribution appears more spherical and localized when the spin is aligned with the field, and a very subtle asymmetry is present in the direction of the field. Spin dependence also manifests itself in the

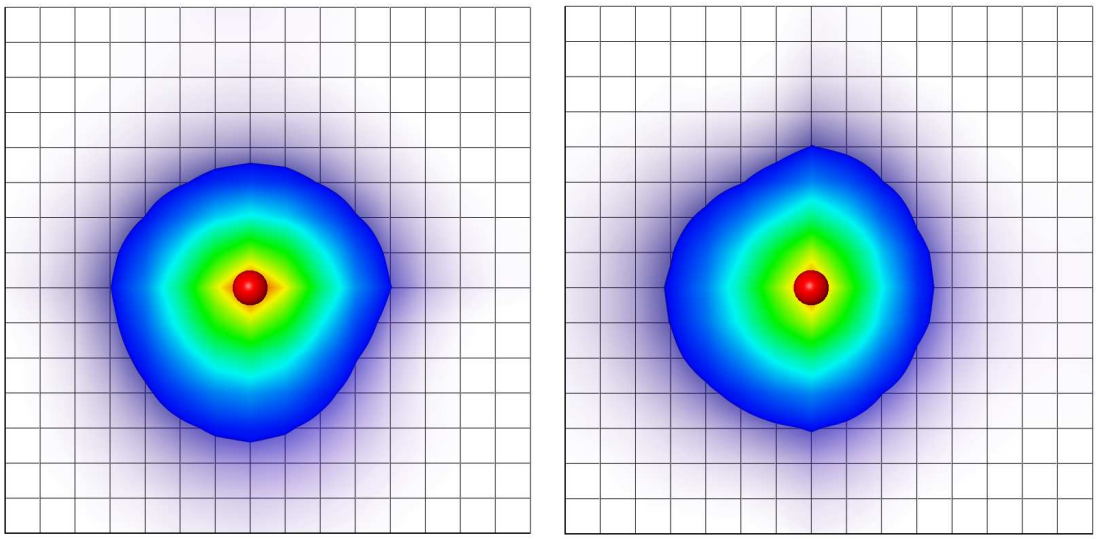

Figure 5.7: The probability distribution for the d quark cut in the $x - y$ plane of the u quarks, in the presence of a background magnetic field in the Landau gauge, with the first implementation (left), and the second implementation (right) of the vector potential described in Section 5.3. In this image, the field, $\vec{B}$, is pointing into the page. The red sphere denotes the location of the remaining quarks. There is a clear asymmetry perpendicular to the field that changes with the vector potential, A_μ, in spite of the background magnetic field not changing.

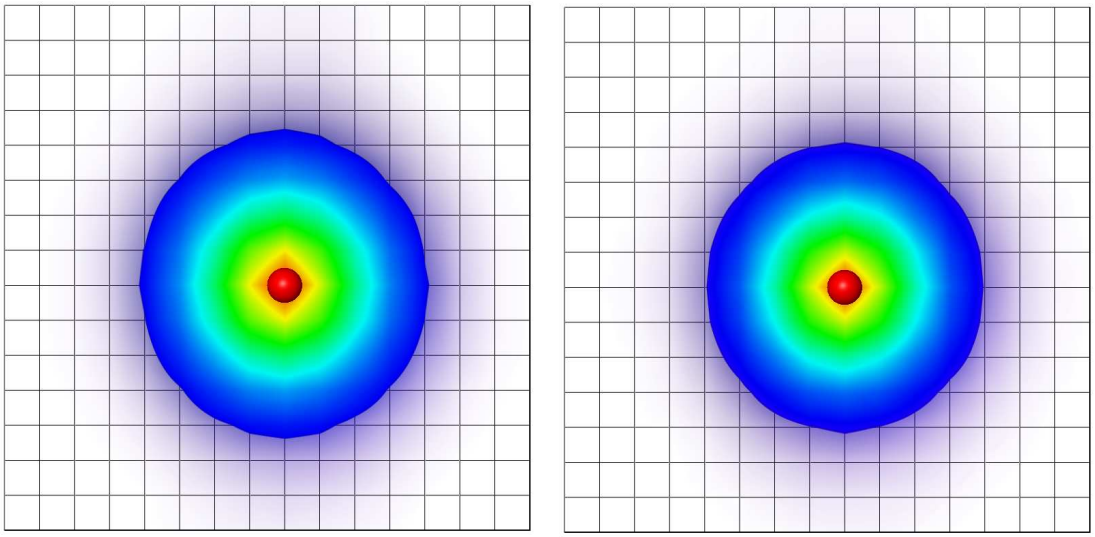

Figure 5.8: The probability distribution for the d quark cut in the $x-z$ plane of the u quarks, after symmetrising the vector potential, A_μ in the presence of the field in the Landau gauge (left) and Coulomb gauge (right). In this image, the field, $\vec{B}$, is pointing to the top of the page, and the u quarks are both in the centre of the lattice, denoted by the red sphere. In spite of the magnitude of the field, a fairly small deviation from spherical symmetry is seen in both gauges.

energy of the proton, as can be seen in Table 5.1, where the energy of the proton when its spin is anti-aligned to the field is lower than the zero-field energy, indicating that Landau levels are not having a dominant effect on the particle energy. The spin aligned proton receives a larger energy, due to the sign on the moment term.

Table 5.1: The dependence of the spin up and spin down mass of the proton on the background magnetic field. When the spin is aligned with the effective field on the proton, the mass of the proton increases, whereas when the spin is anti-aligned with the field, we see a mass decrease. The strength of the field is given for the proton when $n = 1$ in Eq. (2.79) applied to the d quark.

κ	spin	B	Mass (GeV)	m_π^2 (GeV^2)	window	χ^2/dof
0.12885	averaged	0	1.492(10)	0.486	10-18	1.001
	anti-aligned	-3	1.366(11)		10-14	0.879
	aligned	-3	1.688(11)		10-18	0.991
0.12990	averaged	0	1.327(11)	0.283	10-18	0.954
	anti-aligned	-3	1.197(13)		10-14	1.061
	aligned	-3	1.528(13)		10-15	0.983

The localization of the spin aligned probability distribution can be understood in terms of a constituent quark mass effect in a simple potential model. The effect of the increased proton energy is to cause an increase in the constituent quark mass, hence causing the probability distribution to sit lower in the potential. This makes the spin aligned probability distribution smaller than the spin anti-aligned probability distribution.

As the quarks are separated, the probability distributions in the background field tend to be more localized than the same probability distributions without a background field. Some stretching along the field orientation at the centre of the distribution is apparent, making the distribution more spherical (Fig. 5.11). This is consistent with the effect of raising the constituent quark mass. In the Landau gauge, the diquark clustering is removed from the d quark probability distribution by the presence of the field as illustrated in Fig. 5.12.

In contrast, diquark clustering is still apparent in the u quark probability distribution in the presence of the field, with the distribution moving towards the centre of the baryon on application of the magnetic field, as shown in Figs. 5.13

and 5.14. The scalar u quark probability distribution also shows more localization than either the vector u quark or d quark probability distributions. The anti-symmetrised u quark probability distribution illustrated in Figs. 5.15 and 5.16 still bears close resemblance to that of the scalar u quark. However, it is not as localized as the scalar u quark probability distribution due to the contribution from the vector u quark required to anti-symmetrise the identical u quarks. The Landau gauge probability distribution is still larger than the Coulomb gauge probability distribution.

As illustrated in Figs. 5.17 and 5.18 for the Coulomb and Landau gauges respectively, the effect of the field on the probability distribution of the vector u quark is more pronounced than the d quark and scalar u quark probability distributions.

The spin orientation dependence as the quarks are separated remains largely the same as in the case where the quarks are at the origin, with the vector u quark probability distribution changing the most between the spin aligned and anti-aligned cases. In the case where the spin is aligned with the field and the mass increases, the probability distribution becomes more localized perpendicular to the field relative to when the spin is anti-aligned with the field. This is in keeping with the constituent quark model, where the field causes the constituent quark mass to increase, and as such, the proton sits lower in the potential.

Very little spin dependence is visible in the d quark and scalar u quark probability distributions. However, the effect on the probability distribution due to the magnetic field is more prominent when the remaining quarks are separated, compared to when the quarks are at the origin.

5.5 Relativistic Wave Functions

Non-zero momentum wave functions have been briefly investigated in an early study [34], in which Lorentz contraction was able to be observed for the pion at relatively small momentum. Using the smearing optimisation method detailed in Chapter 4, we investigate the wave function of the proton at momentum up to $p_x = \frac{N_S}{4}$ lattice units in the Landau Gauge.

Following the conclusions of the previous chapter, we choose to only optimise over the number of smearing sweeps, and to not add any anisotropy. The ideal

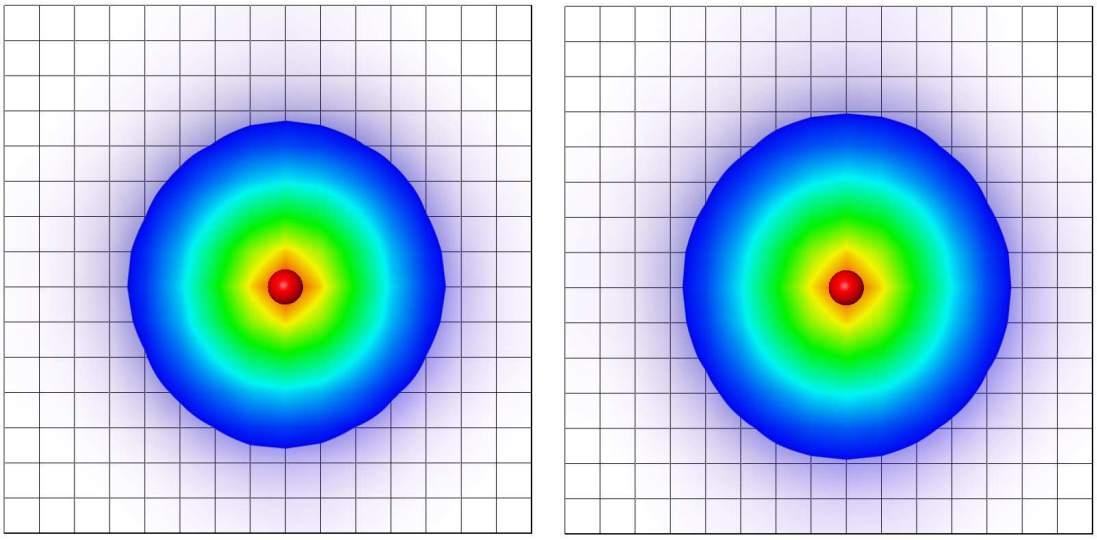

Figure 5.9: The probability distribution for the vector u quark in the presence of the background field, cut in the $x - z$ plane of the remaining quarks in the Coulomb gauge with the spin aligned (left) and anti-aligned (right) to the field. The direction of the field is down the page, and the red sphere denotes the remaining quarks. The probability distribution appears more spherical and localized when aligned with the field, and a very subtle asymmetry is present in the direction of the field.

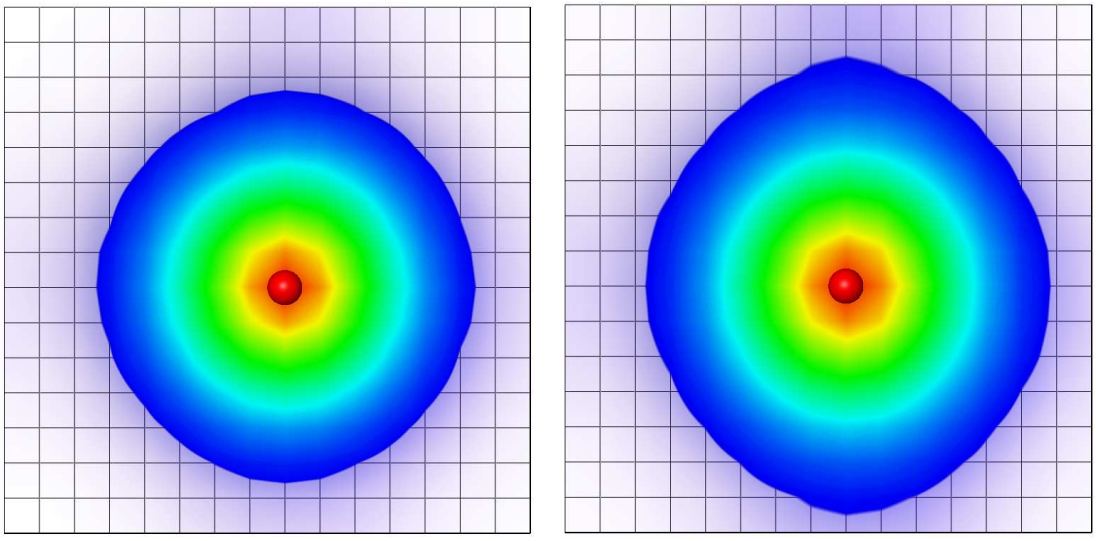

Figure 5.10: The probability distribution of the vector u quark in the presence of the background field, cut in the $x - z$ plane of the remaining quarks in the Landau gauge with the spin aligned (left) and anti-aligned (right) to the field, and the red sphere denotes the remaining quarks. The direction of the field is down the page. Much like in the Coulomb gauge, the probability distribution appears more spherical and localized when aligned with the field.

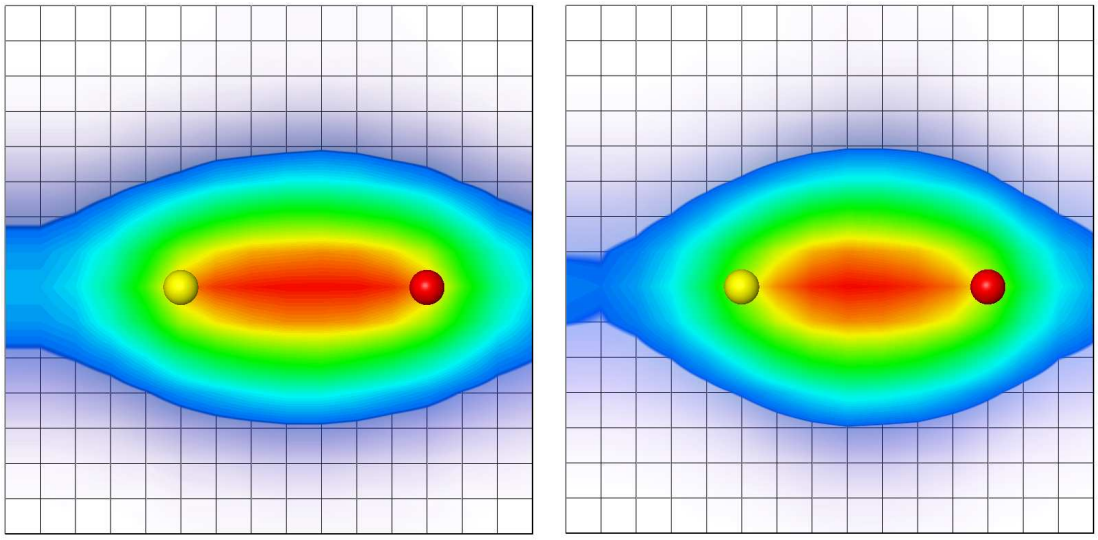

Figure 5.11: The probability distribution of the d quark in the Coulomb gauge cut in the $x-z$ plane of the u quarks which are separated by seven lattice units in the transverse direction with zero background field (left) and in the presence of the field (right). The direction of the field is up the page and the spheres denote the positions of the u quarks.

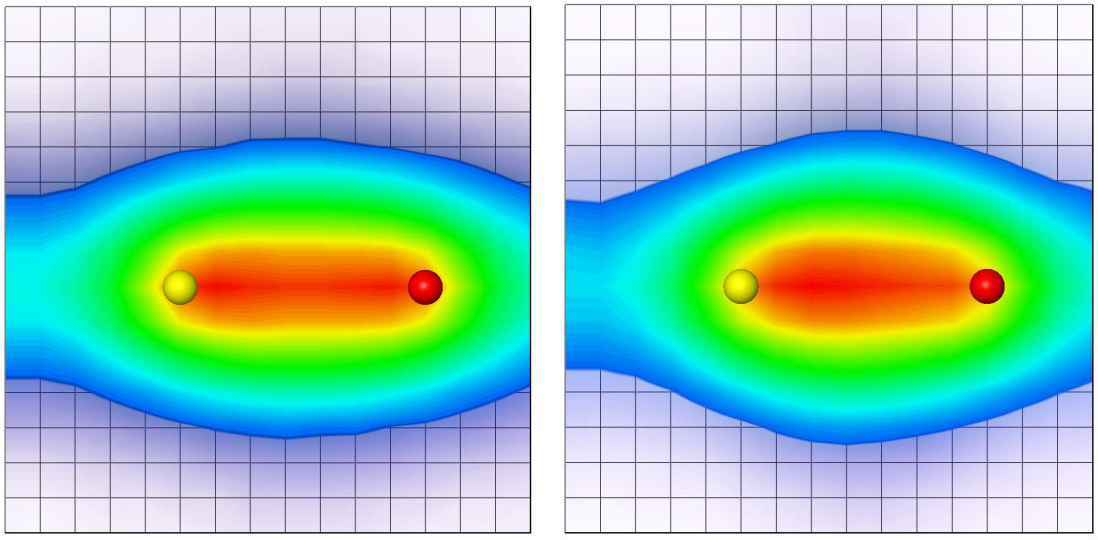

Figure 5.12: The probability distribution of the d quark, in the Landau gauge cut in the $x-z$ plane of the remaining quarks which are separated by 7 lattice units in the transverse direction with zero background field (left) and in the presence of the field (right). The spheres denote the positions of the u quarks. The diquark clustering is barely visible in this view, and disappears completely in the presence of the field. The probability distributions are broader in the Landau gauge.

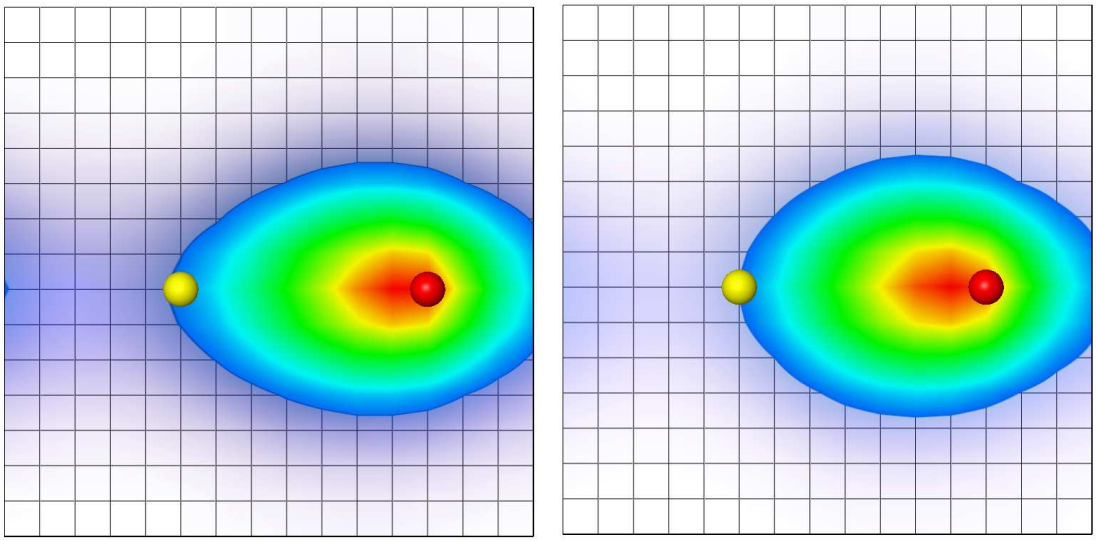

Figure 5.13: The probability distribution of the scalar u quark in the Coulomb gauge cut in the $x-z$ plane of the remaining quarks which are separated by seven lattice units in the transverse direction with zero background field (left) and in the presence of the field (right). The direction of the field is up the page and the d quark is on the right, denoted by the red sphere. In contrast to the d quark probability distribution, there is still a distinct preference for the formation of a scalar diquark. When the field is applied, the probability distribution can be seen to move toward the centre of the lattice.

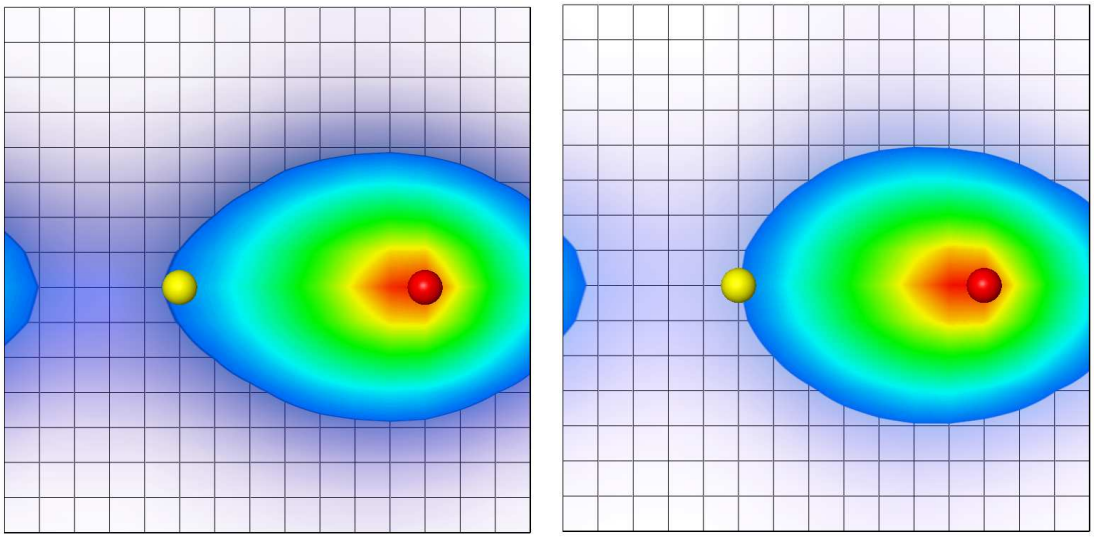

Figure 5.14: The probability distribution of the scalar u quark, in the Landau gauge which are separated by 7 lattice units in the transverse direction with zero background field (left) and in the presence of the field (right). The direction of the field is up the page and the d quark is on the right, denoted by the red sphere. Preference towards the centre of the lattice is also visible in the Landau gauge, but is more subtle than in the Coulomb gauge.

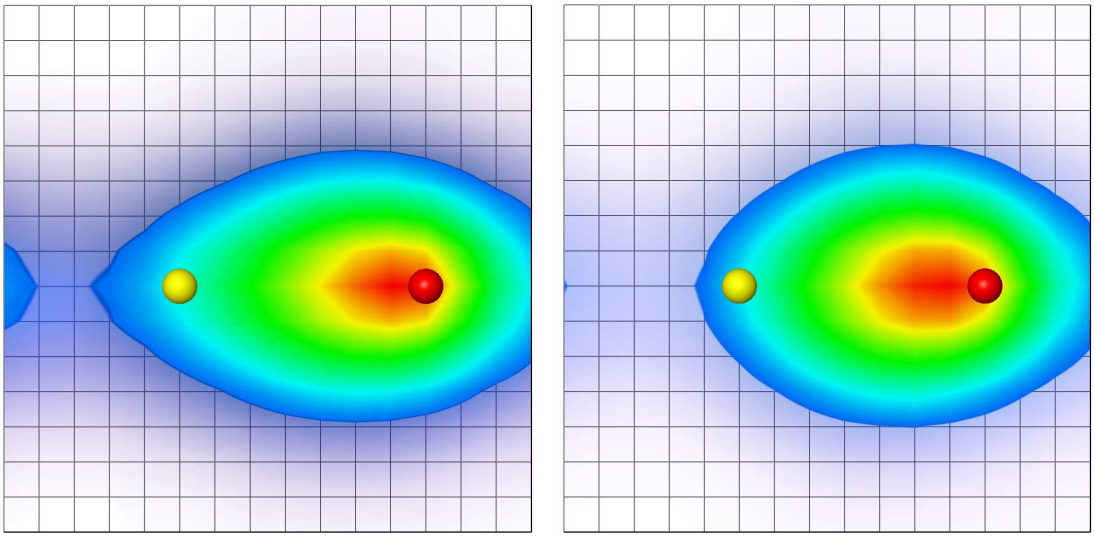

Figure 5.15: The probability distribution of a u quark in the Coulomb gauge cut in the $x-z$ plane of the remaining quarks which are separated by seven lattice units in the transverse direction with zero background field (left) and in the presence of the field (right). The direction of the field is up the page and the d quark is on the right, denoted by the red sphere. The symmetrised u quark probability distribution bears close resemblance to the scalar u quark, but less localized due to the vector u quark contribution.

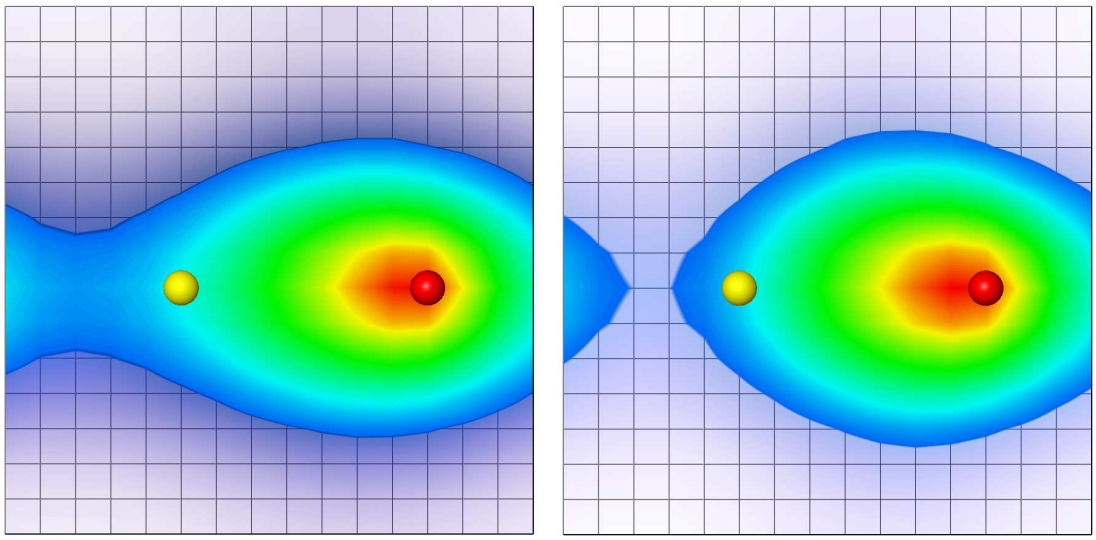

Figure 5.16: The probability distribution of a u quark, in the Landau gauge cut in the $x-z$ plane of the remaining quarks which are separated by 7 lattice units in the transverse direction with zero background field (left) and in the presence of the field (right). The direction of the field is up the page and the d quark is on the right, denoted by the red sphere. The contribution to the symmetrised probability distribution from the vector u quark is enhanced in the Landau gauge compared to the Coulomb gauge.

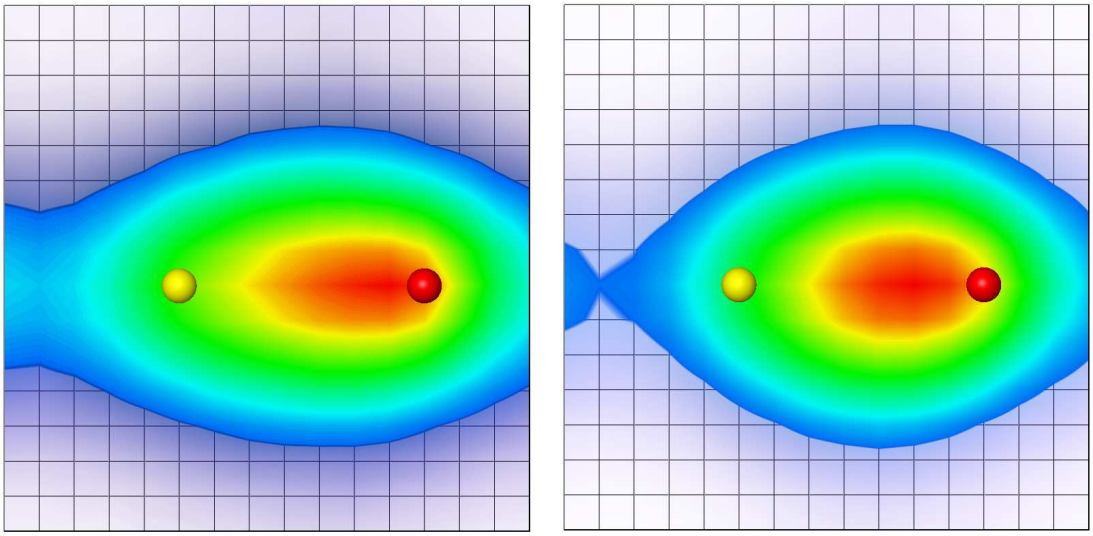

Figure 5.17: The probability distribution of the vector u quark in the Coulomb gauge cut in the $x-z$ plane of the remaining quarks which are separated by seven lattice units in the transverse direction with zero background field (left) and in the presence of the field (right). The direction of the field is up the page and the d quark is on the right, denoted by the red sphere. The effect of the field on the vector u quark probability distribution is more pronounced than the d quark and scalar u quark probability distributions.

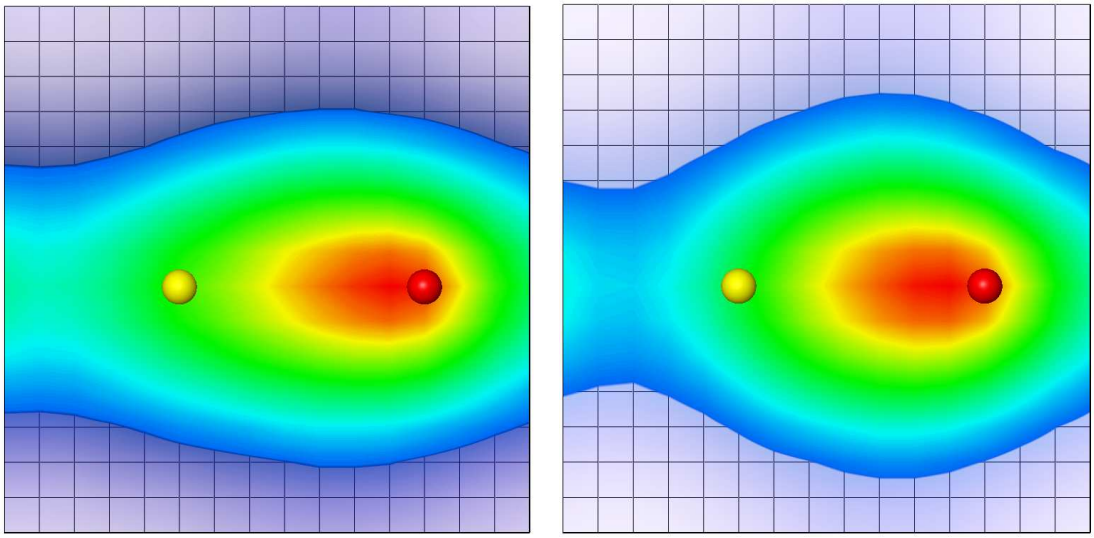

Figure 5.18: The probability distribution of the vector u quark, in the Landau gauge cut in the $x-z$ plane of the remaining quarks which are separated by 7 lattice units in the transverse direction with zero background field (left) and in the presence of the field (right). The direction of the field is up the page and the d quark is on the right, denoted by the red sphere.

p_x	p_y	p_x	n_{sweeps}	M_1
0	0	0	45	-0.00475
1	0	0	40	-0.0209
2	0	0	31	-0.0334
3	0	0	23	-0.996
4	0	0	14	-12.38

Table 5.2: The ideal number of smearing sweeps and the value of M_1 from Eq. (4.7) with $t_i = 1$ and $t_f = 7$ time slices after the source at each momentum considered.

number of smearing sweeps for each of the 5 values of momentum considered is given in Table 5.2. We have kept t_i and t_f consistent between all momentum, and as such, the value of the measure for $p_x = 4$ is significantly higher than the rest. Reducing t_f by a single time slice, to 6 after the source, reduces the value of the measure at 14 sweeps of source smearing by a factor of 4, indicating that the signal is reasonable even 6 time slices after the source.

Figure. 5.19 shows the wave function calculated at 2 units of lattice momentum in the x direction, which gives the expected Lorentz contraction factor $\gamma^{-1} = 0.73$. calculated 3 time slices after the source. Clearly, the wave function constructed at 45 sweeps of source smearing exhibits the most contraction in the tail, however, all 3 probability distributions shown exhibit roughly consistent contraction closer to the peak of the distribution, up to the edge of the light blue shaded area. At this relatively low momentum, it is apparent that a reasonable wave function can be extracted without the need for an optimised source.

Wave functions constructed at the highest momentum considered, giving a Lorentz contraction factor of $\gamma^{-1} = 0.47$, shown in Fig. 5.20, demonstrate that only the wave function constructed with the optimised source resembles a Lorentz contracted state 3 time slices after the source. The wave functions constructed by all other source operators have clear artefacts due to poor coupling with the operator. These results reinforce the need for carefully tuned operators when accessing high momentum states on the lattice.

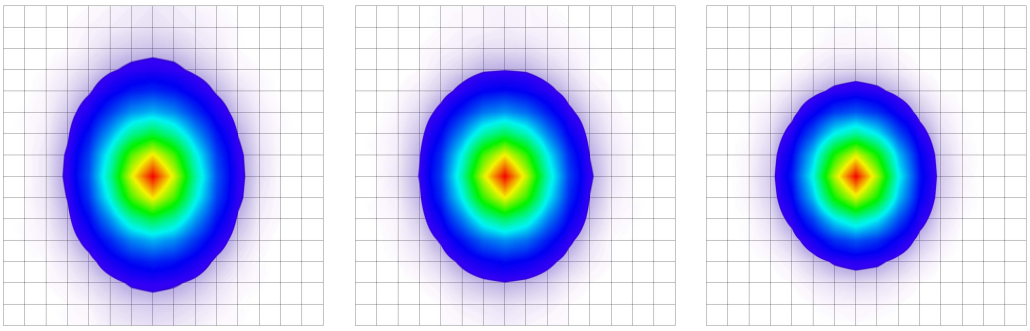

Figure 5.19: The probability distribution of the d quark at two units of lattice momentum applied across the page, with the u quarks co-located in the centre of mass of the system in the Landau gauge at 45 (left), 31 (center) and 14 (right) sweeps of source smearing. The number of sweeps chosen was determined to be ideal by performing the analysis detailed in the previous chapter for zero, 2 and 4 units of lattice momentum respectively. All probability distributions have been cut of at the same relative value to the peak. It is clear that, even at this relatively low value of momentum, differences are visible in the wave functions.

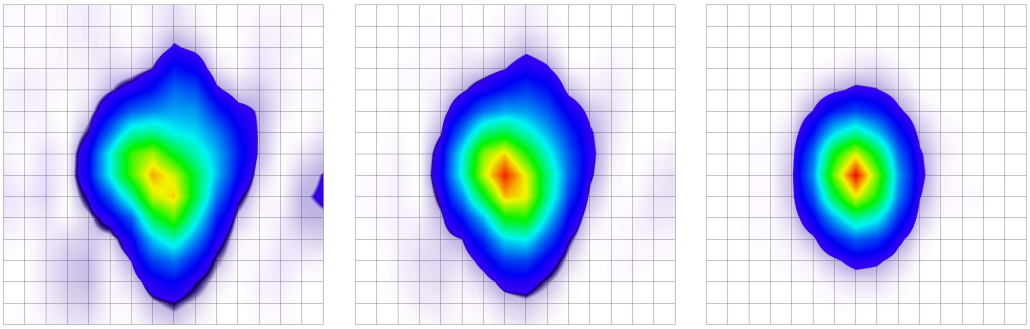

Figure 5.20: The probability distribution of the d quark at four units of lattice momentum applied across the page, with the u quarks co-located in the centre of mass of the system in the Landau gauge at 45 (left), 31 (center) and 14 (right) sweeps of source smearing. The number of sweeps chosen was determined to be ideal by performing the analysis detailed in the previous chapter for zero, 2 and 4 units of lattice momentum respectively. All probability distributions have been cut of at the same relative value to the peak. Only the wave function produced at the ideal number of smearing sweeps bares any resemblance to a Lorentz contracted state.

5.6 Summary

In this chapter, we have performed the first examination of the probability distribution of quarks in the proton in the presence of a background magnetic field in both the Landau and Coulomb gauges.

We have shown that there is a distinct difference between the d quark probability distributions in the Landau and Coulomb gauge, with the Landau gauge exhibiting clear diquark clustering. The probability distributions in the Coulomb gauge did not. The scalar u quark and vector u quark probability distributions show clear diquark clustering in both the Landau and Coulomb gauge, with the scalar u quark being more tightly bound to the d quark than the vector u quark probability distribution. This is the first direct evidence of the ability of a scalar diquark pair to form in a baryon. Also, the probability distributions in the Landau gauge were larger than those in the Coulomb gauge.

On the application of the background field, we found a gauge dependence in the probability distribution in the direction of the vector potential. A symmetrisation was performed to rectify this.

In spite of the very large magnetic field required by the quantisation conditions, the change in the probability distribution is small, being most prominent in the vector u quark. The effect is to elongate the distribution along the axis of the field while generally localizing the distribution. The vector u quark exhibits the most spin dependence, with the probability distribution being more localized when the spin is aligned with the magnetic field. This effect can be understood in terms of a constituent quark model where the constituent quark mass increases in the presence of the magnetic field.

More notable spin dependence appeared in the energy of the proton itself, largely associated with the magnetic moment, as opposed to higher order effects impacting the structure of the proton. The nucleon is rather stiff and only slightly more localized in a magnetic field. We anticipate the background field approach to determining the magnetic moment of baryons to be effective, even in a strong background field.

On the application of momentum along one axis, Lorentz contraction was visible in the probability distribution. At lower momenta, a tuned source was not necessary for the production of a clean probability distribution. When momentum was increased to the highest value considered, only the probability distribution

generated by the tuned source was relatively free of unphysical artefacts, reinforcing the need for carefully tuned sources when considering high momentum states.

Chapter 6

Full QCD Wave Function

The hadron spectrum is the manifestation of the highly complex dynamics of QCD. It is an observable that is readily accessible in collider experiments. While the quantum numbers of the states can be ascertained, properties providing more insight into the structure of the resonances often remain elusive to experiment. We aim to provide some insight into the underlying dynamics governing the structure of these states.

Recent advances in the isolation of nucleon excited states through correlation-matrix based variational techniques in lattice QCD now enable the exploration of the structure of these states and how these properties emerge from the fundamental interactions of QCD.

In this chapter, we focus on the wave function of the Roper excitation [73] to the four lowest-lying even-parity states excited by the standard χ_1 interpolating field which incorporates a scalar diquark construction. We examine the quark mass dependence of the probability distributions for these states. Here we search for a signature of multi-particle components mixed in the finite-volume QCD eigenstates at the two largest quark masses where the states sit close to the multi-particle thresholds. We also explore the dependence of the d-quark probability distribution on the positions of the two u quarks along an axis through the centre of the distribution.

In presenting our results we make extensive use of isovolume and surface plots of the probability distributions for the quarks. Such visualizations have already been used to illustrate physical effects such as Lorentz contraction [34, 36], the effect of external magnetic fields [47] and finite volume effects [48, 74], for example.

Early explorations of these states were based on non-relativistic constituent quark models. The probability distributions of quarks within hadrons were determined using a one-gluon-exchange potential augmented with a confining form [75, 76]. These models have been the cornerstone of intuition of hadronic probability distributions for many decades. In this chapter, we will confront these early predictions for quark probability distributions in excited states directly via Lattice QCD.

6.1 Lattice Techniques

Robust methods have been developed that allow the isolation and study of the states associated with these resonances in Lattice QCD [19, 38, 39, 45, 48, 77, 78, 79, 80, 81, 82, 83], which we discuss in detail in Section 3.2. We apply the variational method [40, 41] to extract the ground state and first three P_{11} excited states of the proton associated with the Roper [73] and other higher-energy P_{11} states. We then combine this with lattice wave function techniques to calculate the probability distributions of these states at several quark masses and quark positions. We use the $2+1$ flavour $32^3 \times 64$ PACS-CS configurations [66] at a pion mass as low as 156 MeV.

Landau gauge is a smooth gauge that preserves the Lorentz invariance of the theory. While the size and shape of the wave function are gauge dependent, our selection of Landau gauge is supported by our results. For example, the ground state wave function of the d quark in the proton is described accurately by the non-relativistic quark model using standard values for the constituent quark masses and string tension of the confining potential [48]. Therefore this gauge provides a foundation for a more comprehensive wave function examination.

The non-local sink operator used to construct the wave function is unable to be smeared, and hence the standard technique of Eq. (3.22) cannot be applied. However, Eq. (3.19) illustrates it is sufficient to isolate the state at the source using the right eigenvector. Thus, the probability distributions are calculated with each smeared source operator and the right eigenvectors calculated from the standard variational analysis are then applied in order to extract the individual states of interest.

Our focus on χ_1 in this investigation follows from the results of Ref. [84],

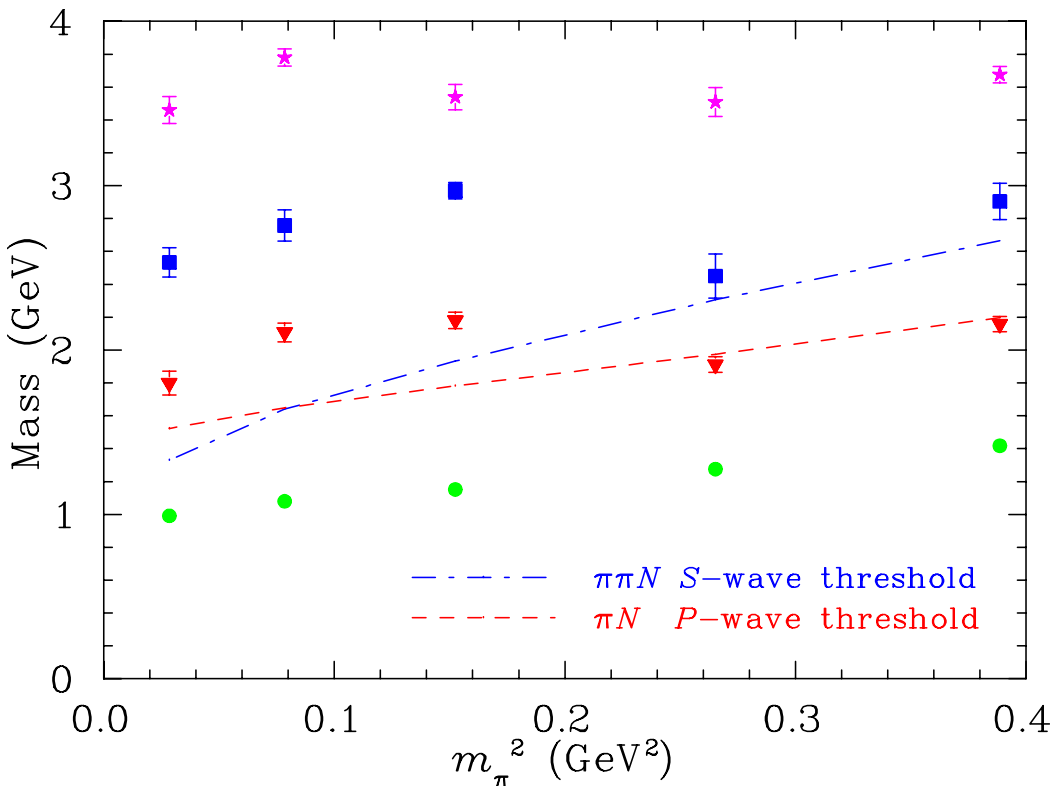

Figure 6.1: The mass dependence of the four lowest-lying even-parity eigenstates excited by the χ_1 interpolating field is compared with the S and P-wave non-interacting multi-particle energy thresholds on the finite volume lattice. Plot symbols track the eigenvector associated with each state.

where the lowest-lying excitation of the nucleon was shown to be predominantly associated with the χ_1 interpolating field. The results from their 8×8 correlation matrix of χ_1 and $\chi_2 = \epsilon^{abc} \left(u^{Ta}(x) \, C \, d^b(x) \right) \gamma_5 \, u^c(x)$ revealed that χ_2 plays a marginal role in exciting the Roper. The coefficients of the Roper source eigenvector multiplying $\overline{\chi}_2$ are near zero. Further comparison with Ref. [84], identifies the third state extracted herein as the fifth state of the twelve states identified and the fourth state herein as the tenth state. Figure 6.1 illustrates the quark mass dependence of these four states which will be examined in detail herein.

The quark mass flow of these states tracked by their associated eigenvectors [84] is not smooth and suggests the presence of avoided level crossings as one transitions from the heaviest two quark masses to lightest three quark masses. At the two heaviest quark masses, it is seems likely these states are dominated by multi-particle $N\pi$ components, whereas at the lighter three quark masses, single

particle components are more dominant. We will search for evidence of this in the wave functions of these states.

In summary, the wave function for the d quark in state α having momentum $\vec{p}$ observed at Euclidean time t with the u quarks at positions $\vec{d}_1$ and $\vec{d}_2$ is

$$\psi_d^\alpha(\vec{p},t;\vec{d}_1,\vec{d}_2;\vec{z}) = \sum_{\vec{x}} e^{-i\vec{p}\cdot\vec{x}} \,\mathrm{tr}\,(\gamma_0+1) \\ \langle\Omega|\, T\{\,\chi_1(\vec{x},\vec{d}_1,\vec{z},\vec{d}_2;t)\,\bar{\chi}_j(\vec{0},\vec{0},\vec{0},\vec{0};0)\,\}\,|\Omega\rangle\, u_j^\alpha\,, \tag{6.1}$$

where $\chi_1(\vec{x},\vec{d}_1,\vec{z},\vec{d}_2;t)$ is given by Eq. (3.26).

As discussed above, χ_1 has the spin-flavour construct that is most relevant to the excitation of the Roper from the QCD vacuum. As such, it is an ideal choice for revealing the spatial distribution of quarks within the Roper. However, the selection of χ_1 in Eq. (6.1) is not unique and other choices are possible. For example, the selection of χ_2 would reveal small contributions to the Roper wave function where vector diquark degrees of freedom are manifest. Similarly, D-wave contributions could be resolved through the consideration of a spin-3/2 isospin-1/2 interpolating field at the sink. Research exploring these aspects of the wave functions is in progress.

6.2 Simulation Results

6.2.1 Lattice Parameters

We use the $2+1$ flavour $32^3\times 64$ configurations created by the PACS-CS collaboration [66] constructed with the Iwasaki gauge action [12] and the $\mathcal{O}(a)$-improved Wilson action [16] with $\beta = 1.90$, giving a lattice spacing of 0.0907(13) fm. The hopping parameters are 0.13700, 0.13727, 0.13754, 0.13770 and 0.13781 giving pion masses of 702, 570, 411, 296 and 156 MeV respectively. For each quark mass we consider 398, 391, 447, 395 and 198 gauge field configurations respectively, and at the lightest quark mass we increase statistics through the consideration of four sources per configuration distributed evenly along the time axis.

To isolate the QCD eigenstates, a 4×4 variational basis is constructed using the χ_1 operator with four smearing levels; 16, 35, 100 and 200 sweeps [45] of gauge-invariant Gaussian smearing [21]. These smearing levels correspond to

smearing radii of 2.37, 3.50, 5.92 and 8.55 lattice units or 0.215, 0.317, 0.537 and 0.775 fm respectively.

The choice of variational parameters $t_0 = 2, \triangle t = 2$ relative to the source position is ideal, resulting in the effective mass plateaus of the states commencing at $t = t_0 = 2$ as desired [48]. This indicates that the number of states contributing significantly to the correlation functions of the correlation matrix at $t_0 = 2$ equals the dimension of the correlation matrix. As such we examine the wave functions of all four states with the caution that the fourth state is most susceptible to excited state contamination. In reporting the wave functions we select the mid point of the correlation matrix analysis at $t = 3$. The wave functions observed for all our states show an approximate symmetry over the eight octants surrounding the origin. To improve our statistics we average over these eight octants when $d_1 = d_2 = 0$, and an average over the four quadrants sharing an axis with the u quark separation at all other values of d_1 and d_2.

We fix to Landau gauge by maximizing the $\mathcal{O}(a^2)$ improved gauge-fixing functional [50]

$$\mathcal{F}_{Imp} = \sum_{x,\mu} \mathrm{Re}\,\mathrm{tr}\left(\frac{4}{3}U_\mu(x) - \frac{1}{12\,u_0}\left(U_\mu(x)U(x+\hat{\mu}) + \mathrm{h.c.}\right)\right) \tag{6.2}$$

using a Fourier transform accelerated algorithm [49], described in detail in Section 3.4.

In carrying out our calculations, we average over the equally weighted $\{U\}$ and $\{U^*\}$ link configurations as an improved unbiased estimator [55]. The two-point function is then perfectly real and the probability density is proportional to the square of the wave function. In this analysis, we choose to look at the zero-momentum probability distributions.

6.2.2 Wave Functions and Constituent Quark Model Predictions

Figure 6.2 presents the wave functions for the first three states at our lightest quark mass providing $m_\pi = 156$ MeV. In the excited states, the wave function changes sign revealing a node structure consistent with $2S$ and $3S$ excited state wave functions. To further explore the details of these wave functions, we con-

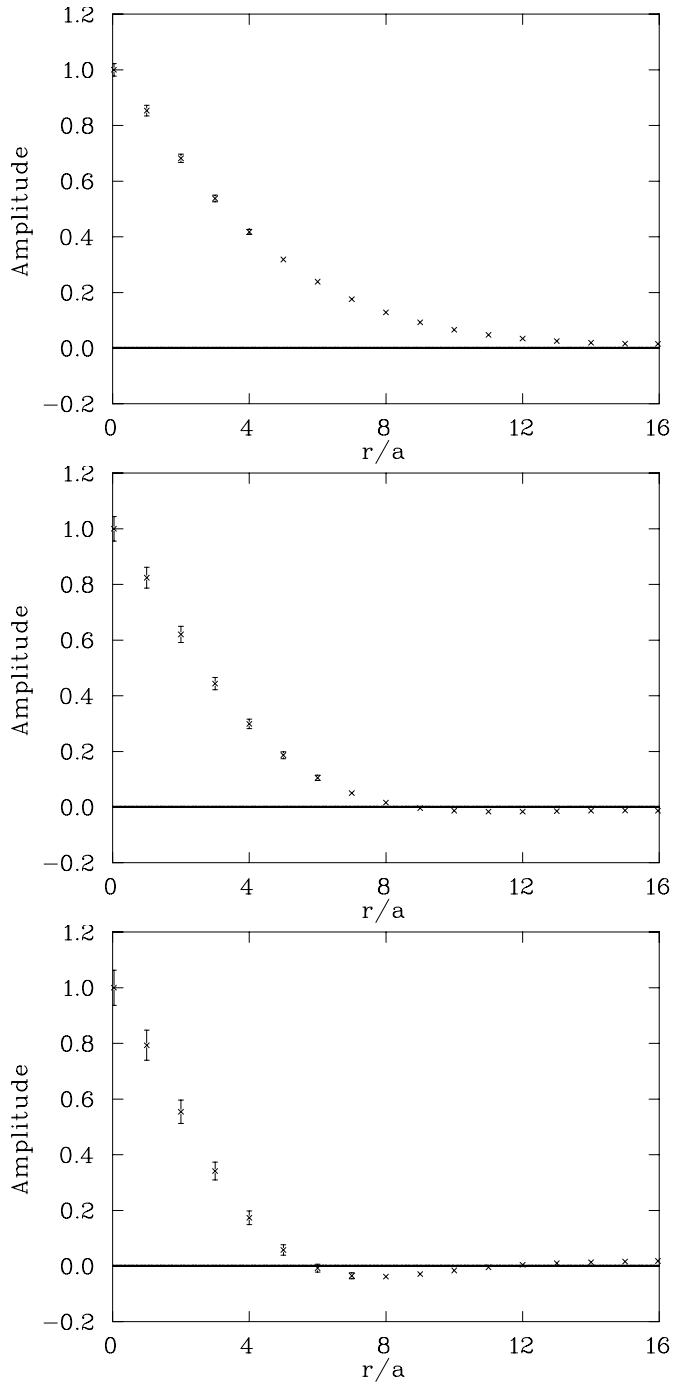

Figure 6.2: The wave function of the d quark in the proton about the two u quarks fixed at the origin for the lightest quark mass ensemble providing $m_\pi = 156$ MeV. From top down, the plots correspond to the ground, first and second excited states observed in our lattice simulation. The wave function changes sign in the excited states and reveals a node structure consistent with $1S$, $2S$ and $3S$ states.

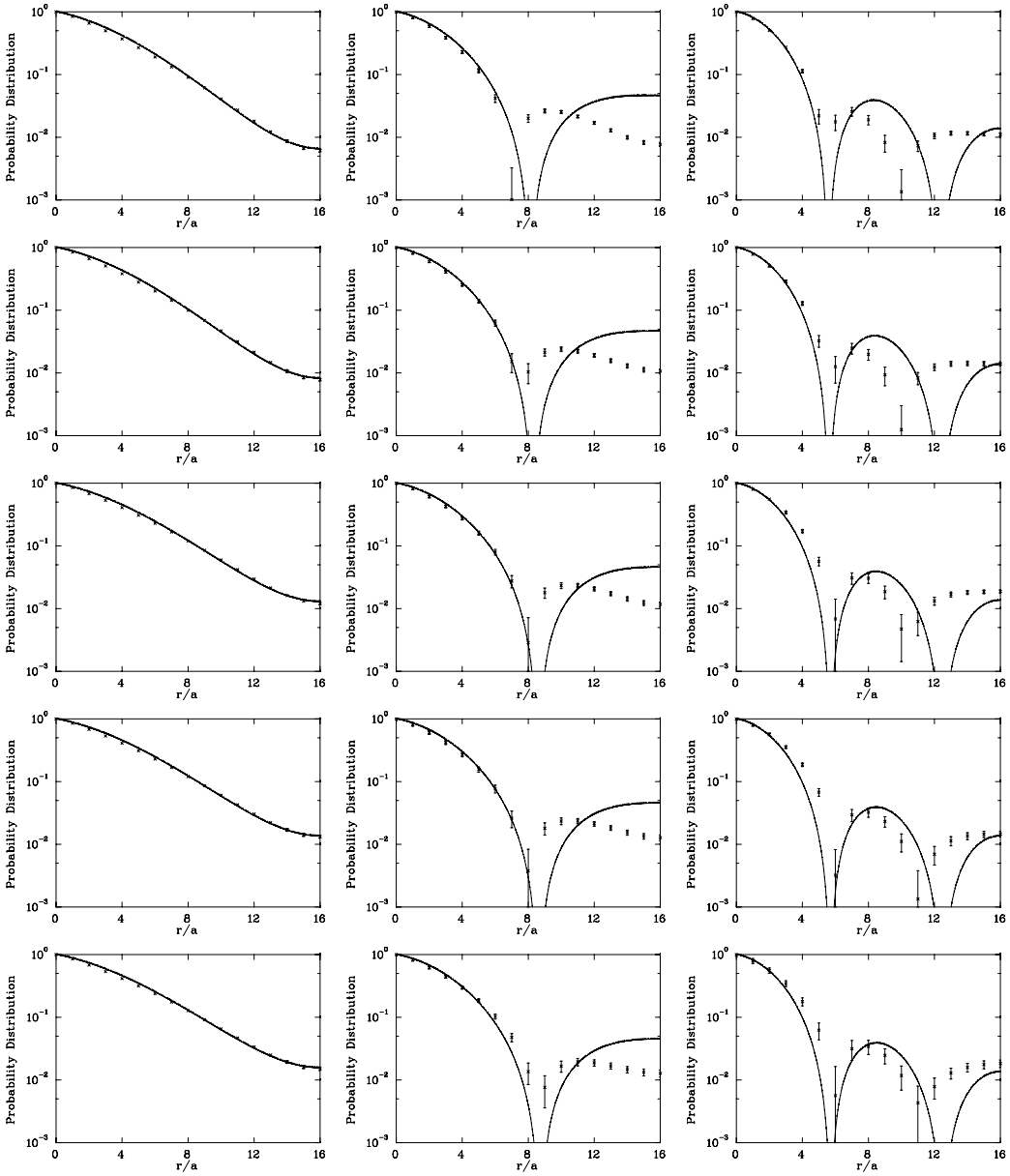

Figure 6.3: The probability distributions for the d quark about two u quarks fixed at the origin obtained in our lattice QCD calculations (crosses) are compared with the quark model prediction (solid curve) for the ground (left column), first- (middle column) and second- (right column) excited states. Quark masses range from the heaviest (top row) through to the lightest (bottom row). The ground state probability distribution of the quark model closely resembles the lattice data for all masses considered. The first excited states matches the lattice data well at small distances, but the node is placed further from the centre of mass in the quark model, after which, the lattice data shows a distinct second peak, whereas the quark model rises to the boundary. It is interesting that the most significant difference is observed where long-distance physics associated with pion-cloud effects not included in the quark model are significant. For the third state the amplitudes of the shells between the nodes of the wave function are predicted well.

struct a probability density from the square of the wave function and plot it on a logarithmic scale in Fig. 6.3.

Our point of comparison with previous models of quark probability distributions comes from a non-relativistic constituent quark model with a one-gluon-exchange motivated Coulomb-plus-ramp potential. The spin dependence of the model is given in Ref. [76] and the radial Schrodinger equation is solved with boundary conditions relevant to the lattice data; *i.e.* the derivative of the wave function is set to vanish at a distance $L_x/2$ from the origin.

We consider standard values of the string tension $\sqrt{\sigma} = 440 \pm 40$ MeV and optimize the constituent quark mass to minimize the logarithmic difference between the quark model and lattice QCD ground-state probability distributions illustrated in the left-hand column of Fig. 6.3. We find best fit results for $\sqrt{\sigma} = 400$ MeV and the optimal constituent quark masses range from 340 to 350 MeV over the range of PACS-CS quark masses available. The quark mass dependence is more subtle than expected and may be associated with the finite volume of the lattice suppressing changes in the wave function as the quark mass is varied. At the lightest quark mass, just above those of Nature, the value of 340 MeV is in accord with those traditionally used to describe the hadron spectrum or baryon magnetic moments.

The lattice data for the first three states and all five quark masses are compared with the constituent quark model in Fig. 6.3. The wave functions are normalized to 1 at the origin. As the quark model parameters are determined using only the ground state probability distribution, the probability densities illustrated for the excited states are predictions.

An examination of the left-hand column of Fig. 6.3 reveals the subtle changes associated with the quark mass. The probability distribution of the heaviest ensemble falls off faster and requires a slightly heavier constituent quark mass to fit the lattice results. This subtle mass dependence is consistent with early, quenched wave function studies [37].

Comparing the lattice probability distribution for the d quark in the first excited state to that predicted by the constituent quark model in the middle column of Fig. 6.3, we see a qualitative similarity but with important differences. The quark model predicts the behavior of the lattice wave function very well within the node and predicts the position of the node rather well, particularly

at the lightest quark mass. However, the shape of the wave function tail is very poorly predicted, suggesting an important role for degrees of freedom not contained within the quark model. For example, the long range pion tail of multi-particle components could alter the distribution of quarks within the state on the lattice. The poorest agreement is for the heaviest ensembles, where the baryon mass is in close proximity to the πN scattering threshold.

Similar comments apply to the second excited state illustrated in the right-hand column of Fig. 6.3. While the positions of the nodes are predicted approximately, the amplitudes of the wave function between the nodes are very accurately predicted by the quark model. Again the largest discrepancies are for the heaviest states where the baryon mass is in close proximity to the $\pi\pi N$ scattering threshold.

6.2.3 Quark Mass Dependence of the Probability Distributions

Ground-State Distribution

The mass dependence of the ground state probability distribution for the d quark about the two u quarks fixed at the origin is illustrated in the two left-hand columns of Fig. 6.4. The plots are arranged from heaviest to lightest ensembles with quark mass decreasing down the page.

Although a Gaussian distribution is used to excite the ground state from the vacuum, the well-known sharp-peaked shape associated with the Coulomb potential is reproduced in the probability density for all quark masses. This is best observed in the left most column where an isosurface reports the probability-density values in the plane containing the two u quarks at the origin.

Because the total probability density is normalised to unity in the spatial volume, the height of the peak drops as the d quark becomes light and moves to larger distances from the u quarks. The isosurface provides the clearest representation of the mass dependence of the ground state.

This gentle broadening of the distribution is also reflected in the isovolume rendering of the projected ground state probability density in the second column if Fig. 6.4. The isovolume has been cut into the plane containing the u quarks at the origin. Probability-density values are depicted by a colour map similar to

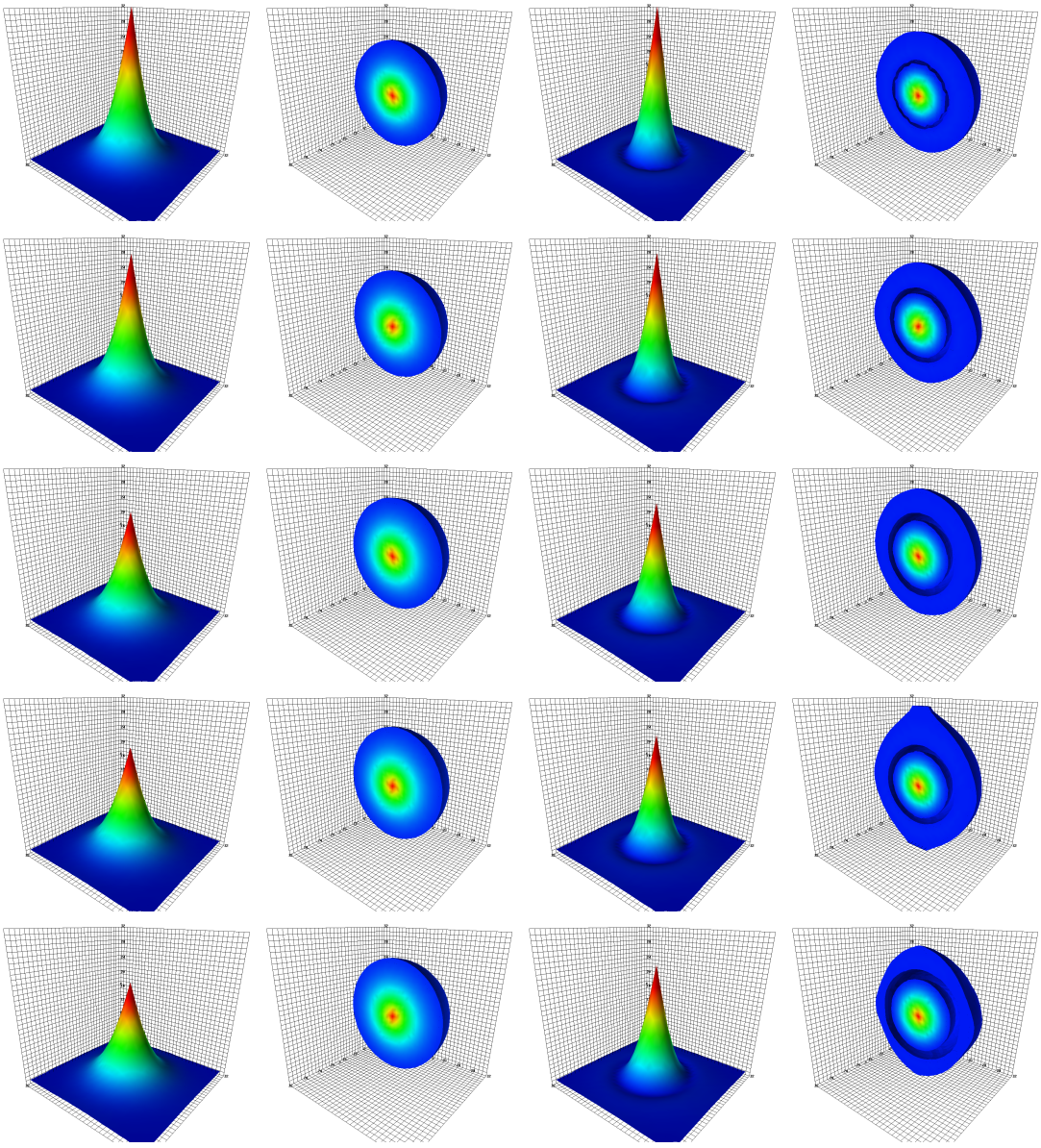

Figure 6.4: The dependence of the d-quark probability distribution on the masses of the quarks in the proton (two left-hand columns) and its first excited state (two right-hand columns). The u quarks are fixed at the origin at the centre of the plot. The quark mass decreases from heaviest (top row) to lightest (bottom row). For each mass and state, the probability density is normalised to unity over the spatial volume of the lattice. The isovolume threshold for rendering the probability distribution in the second and fourth columns is 3.0×10^{-5}.

that used for the isosurface. The threshold for rendering the probability distribution is 3.0×10^{-5}, revealing a smooth sphere for the surface of the probability distribution.

Finite volume effects do not appear to be significant in the probability densities of the ground state at any of the quark masses considered. This is in spite of the fact that the lightest ensemble has $m_\pi L = 2.23$.

First Excited State

Lattice results for the d-quark probability distribution about the two u quarks at the origin in the first excited state of the proton are illustrated in the third and fourth columns of Fig. 6.4. In the light quark-mass regime, this first excited state is associated with the Roper resonance. The darkened ring around the peak of the isosurface indicates a node in the probability distribution, consistent with a $2S$ radial excitation of the d quark. The node is better illustrated in the isovolume renderings where the probability density drops below the rendering cutoff of 3.0×10^{-5} and leaves a void between the inner and outer shells of the state.

It is interesting that the narrowest distribution is seen at the heaviest quark masses, even though these states have energies coincident with the πN scattering threshold. Enforcing a colour singlet structure in annihilating the three spatially separated quarks prevents a direct observation of the two-particle components contained in the dynamics governing the energy of the state. In this case the multi-particle components only modify the three-quark distributions.

The outer edge of the isovolume reveals interesting boundary effects which may be associated with the necessary finite-volume effects of multi-particle components mixed in the state. The deviation from spherical symmetry in the outer shell will be reflected in the energy of the excited state observed in the finite-volume lattice simulation. At the lightest two quark masses, the distortion of the probability distribution is significant and will correspondingly influence the eigen-energy. Even with $m_\pi L = 4.4$ at the second lightest quark mass, finite volume effects distort the wave function in a significant manner. Of course, this interplay between the finite volume and the energy of the state is key to extracting resonance parameters from lattice simulation results.

The nodal structure of the first excited state also indicates that the ideal

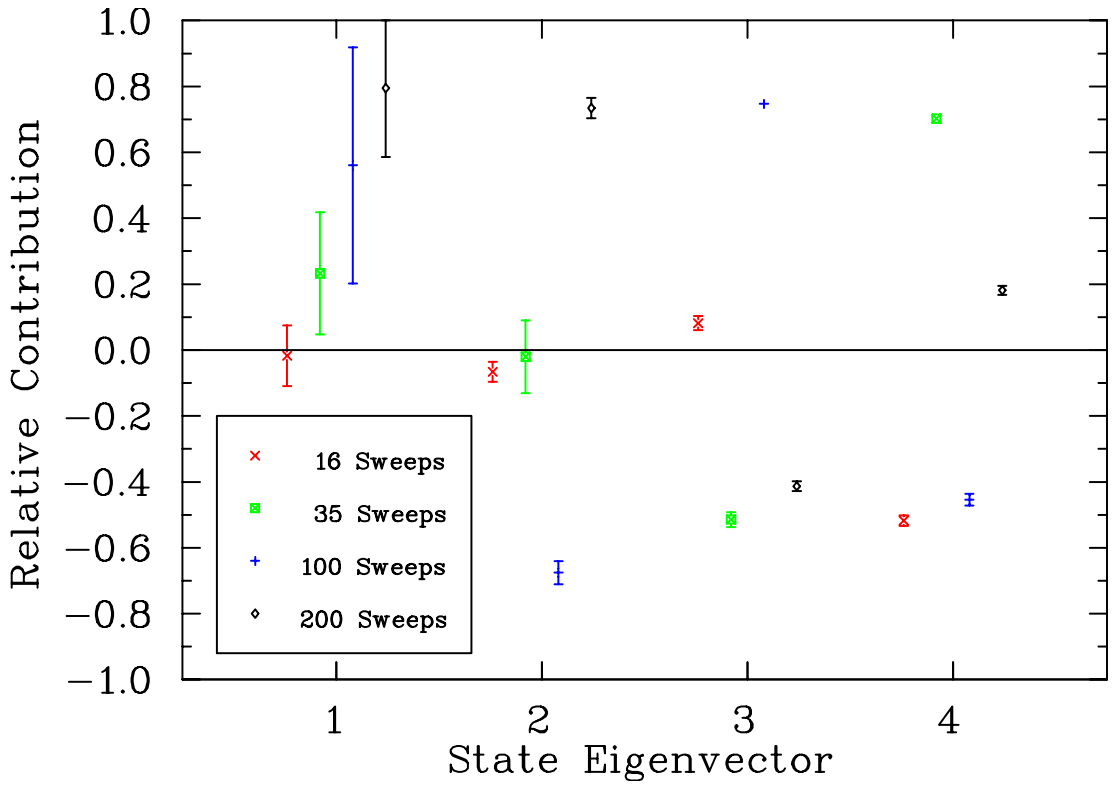

Figure 6.5: The eigenvectors u_i^α describing the contributions of each of the source smearing levels to the states α for the lightest quark-mass ensemble considered. Indices $i = 1$ to 4 correspond to 16, 35, 100 and 200 sweeps of gauge-invariant Gaussian smearing. The superposition of positive and negative Gaussian smearing levels is consistent with the nodal structure recovered in the wave functions.

combination of operators to access this state on the lattice is a superposition of Gaussian distributions of different widths and opposite signs [45, 84]. Figure 6.5 presents the eigenvectors u_i^α describing the contributions of each of the source smearing levels to the states α for the lightest quark-mass ensemble considered.

For the ground state, all smeared sources contribute positively to the state. There is significant interplay between the smeared sources over the jackknife sub-ensembles giving rise to larger uncertainties for the preferred operators. This is not the case for the excited states where particular superpositions of interpolating fields are required to isolate the states.

For the first excited state, a single large width Gaussian contributes with a sign opposite to that of a narrower Gaussian, reflecting the wave function illustrated in the second plot of Fig. 6.2. The combination of sources creating the second excited state has a similar pattern, with a narrow Gaussian contributing positively, an intermediate Gaussian contributing negatively and a wide Gaussian contributing positively, again reflecting the wave function illustrated in Fig. 6.2 for this state. This sign alternating structure is also apparent for the fourth state suggesting a $3S$ excitation for this state. We will examine this state further in the following.

Turning our attention to the mass dependence of the node we note the movement is somewhat unusual. While there is a general trend of the node in the wave function moving outwards as the quark mass decreases, there is negligible movement in the node between the third and second lightest quark masses. We also note how the width of the void in the probability density increases with as the quarks become lighter.

Second Excitation

The probability distributions for the second excitation of the proton observed in this study are illustrated in the two left-hand columns of Fig. 6.6. Two nodes are evident at all quark masses, consistent with a $3S$ radial excitation for the d quark. The first inner node is thin at the heavier masses and difficult to see in the isovolume renderings. Finite volume effects are readily observed in the outer-most shell.

For the heaviest mass, finite volume effects at the nodes are minimal. The nodes are spherical in shape and are largely unaffected by the boundary. Again there is a trend of the nodes moving further from the centre as the quarks become

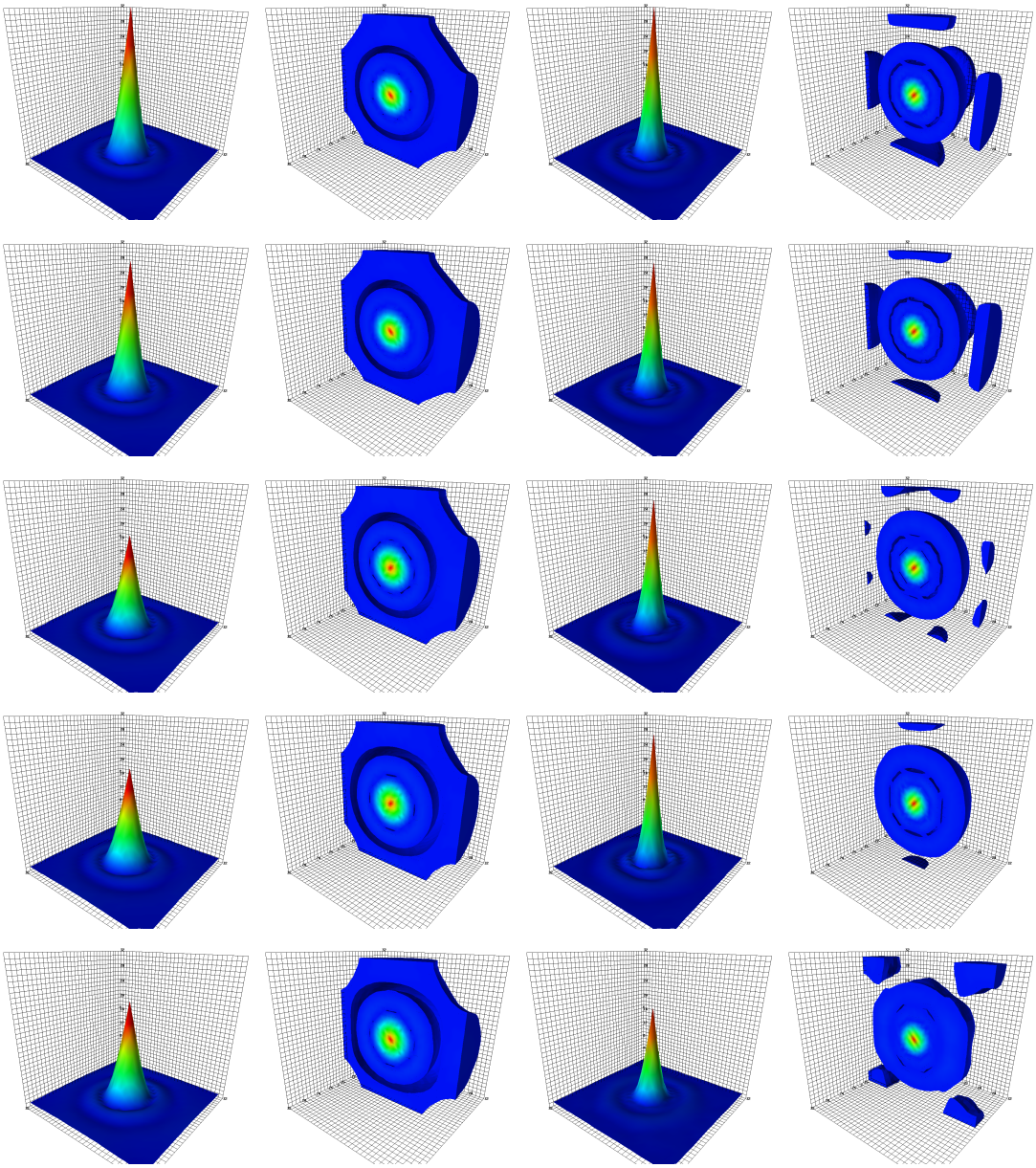

Figure 6.6: The dependence of the d-quark probability distribution on the masses of the quarks in the proton for the second (two left-hand columns) and third (two right-hand columns) S-wave excited states of the proton observed herein. The u quarks are fixed at the origin at the centre of the plot. The quark mass decreases from heaviest (top row) to lightest (bottom row). For each mass and state, the probability density is normalised to unity over the spatial volume of the lattice. The isovolume threshold for rendering the probability distribution in the second and fourth columns is 2.0×10^{-5} and 3.0×10^{-5} respectively. While the former renders the outer shell coherently, the latter better reveals the node structure of the $3S$ distribution.

light.

However, it is the middle quark mass considered that has the broadest distribution. The quark mass flow of the eigenstate energies suggests avoided level crossings are important between the third and fourth heaviest quark masses. It may be a strong mixing with multi-particle states that is giving rise to the broad distribution of quarks at the middle quark mass.

For the lightest two quark masses the outer node has taken on a squared-off shape, having been distorted by the boundary of the lattice. Again, this is an indication that, even though the ground state wave function presents as spherical for this quark mass, this excited state is showing clear finite volume effects. Even at relatively modest quark masses, the wave functions of states above the decay thresholds show an important relationship with the finite volume of the lattice.

Third Excitation

The two right-hand columns of Fig. 6.6 illustrate the mass dependence of the d-quark probability distribution for the the highest excitation of the proton observed in our analysis. The presence of three nodes in the wave function is best observed at the heaviest and second lightest quarks masses.

The inner-most node is easily observed in the surface plots. However it is very sharp and does not render in an obvious manner in the isovolume illustrations. The second node is easily rendered and the third node is very broad. To illustrate this node structure the outer-most shell has become fragmented in the isovolume plots. The fragments reveal the strong finite volume effects on this state.

What is interesting is the manner in which the finite volume effects on the outer shell change as a function of quark mass. At the heaviest quark mass, the outer shell is strongest along the sides of the lattice. By the time one encounters the lightest ensemble, the outer shell has moved to the corners as if there is no longer room for the outer shell along the sides of the 2.9 fm lattice.

6.3 Quark Separation

In order to investigate a more complete picture of the wave functions of the states isolated herein, we choose to focus on the second-lightest quark mass ensemble providing $m_\pi = 293\,\mathrm{MeV}$ and examine the dependence of the d quark probability

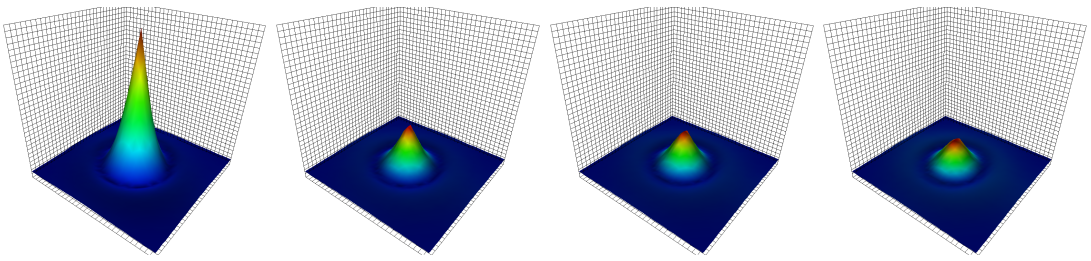

Figure 6.7: The dependence of the d-quark probability distribution on the positions of the u quarks in the first even-parity excited state of the proton at the second lightest quark mass considered. The u quarks are fixed on the x-axis running from back right through front left through the centre of the plot. The u quarks are fixed a distance of d_1 and d_2 from the origin located at the centre. From left to right, the distance $d = d_1 - d_2$ increases, taking values 0, 1, 2 and 3 times the lattice spacing $a = 0.0907$ fm.

distribution on the positions of the two u quarks composing the states. This mass provides the best compromise between finite-volume effects, quark mass and the ensemble size governing the signal quality and associated uncertainties.

In continuing to investigate the wave function of the d-quark, we consider the separation of the u quarks along the x axis as described in Eq. (3.26). All integer separations, $d = d_1 - d_2$, between zero and half the lattice extent in the x direction (*i.e.* 16 lattice units) are considered.

Figure 6.7 illustrates the probability distribution of the d quark for u quarks separated by 0, 1, 2 and 3 lattice steps in the first excited state associated with the Roper resonance. The most notable feature is the rapid reduction in the overlap of the interpolator with the state as the two u quarks are moved away from the origin. While some broadening of the distribution peak is apparent, it is clear that using a normalization suitable for zero u quark separation is not effective for illustrating the probability distribution at large u quark separations.

To better illustrate the underlying shape of the wave functions, the probability distributions are normalised to keep the maximum value of the probability density constant. For small u quark separations, the centre peak height of the distribution is held constant, but for larger separations the maximum value can be elsewhere in the distribution.

Figure 6.8 presents the d-quark probability distributions for u-quark separations of $d = 0$, 2, 4, 6 and 8 times the lattice spacing $a = 0.0907$ fm and Fig. 6.9 completes the study, illustrating u-quark separations of 10, 12, 14 and 16 times the lattice spacing. Each column corresponds to a different state with the ground, first-, second-, and third-excitations illustrated from left to right. The two small spheres above the isosurface indicate the positions of the two u quarks.

Ground-State Distribution

Focusing first on the ground state, on separation of the u quarks the probability distribution of the d quark forms a single broad peak. The structure is slightly rounded until $d = d_1 - d_2 = 12\,a = 1.09$ fm, with small peaks at the u-quark positions. At a separation of $d = 13\,a = 1.18$ fm the wave function takes on a double peak structure associated with scalar-diquark clustering similar to that illustrated in the third row of Fig. 6.9 for $d/a = 14$. These results are similar to the earlier quenched wave function results of Refs. [37, 47].

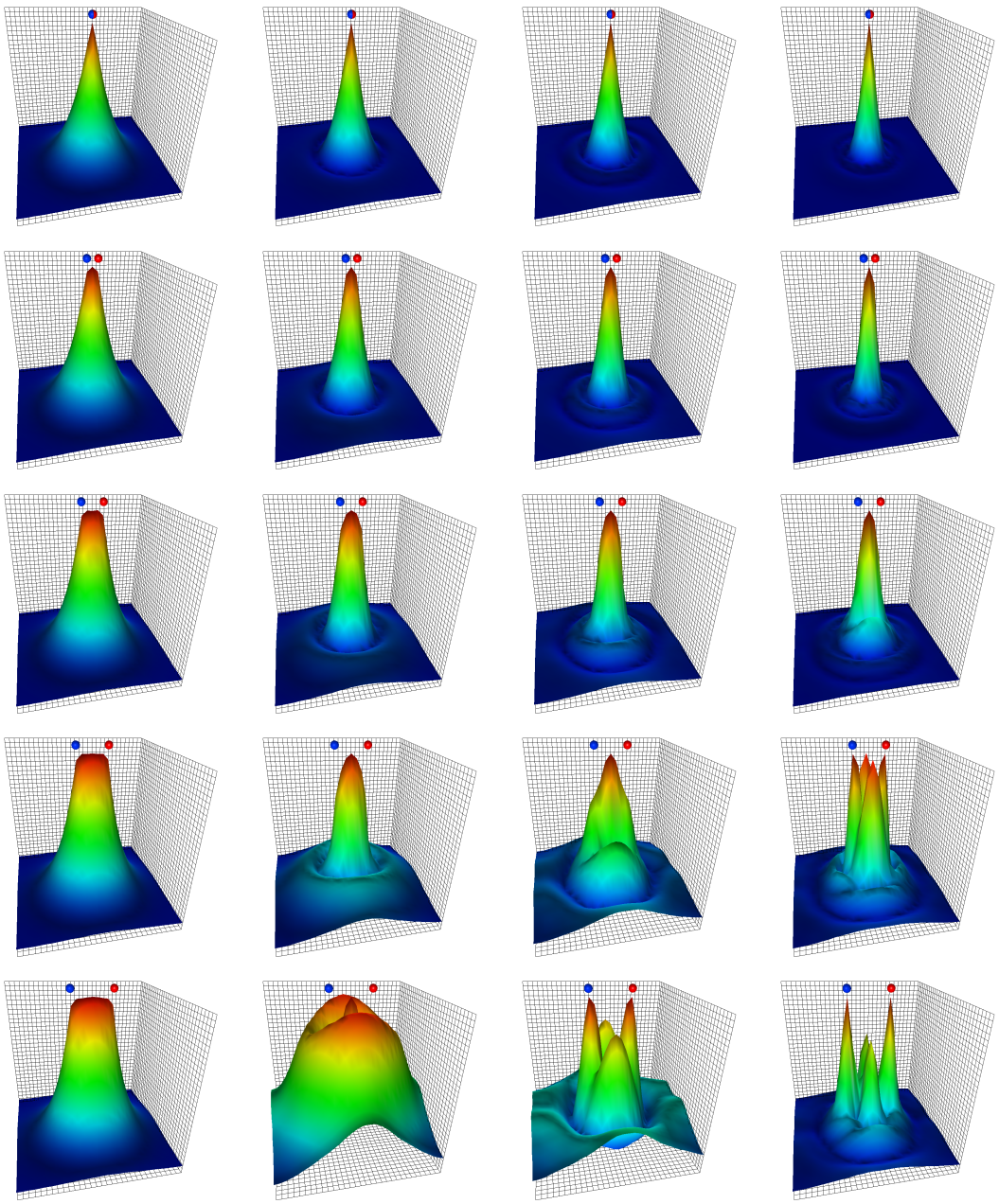

Figure 6.8: The dependence of the d-quark probability distribution on the positions of the u quarks in the proton and its excited states. From left to right, the columns correspond to the ground, first, second and third S-wave excitations. The u quarks are fixed on the x-axis running from back right through front left through the centre of the plot. The u quarks are fixed a distance of d_1 and $d_2 = -d_1$ from the origin located at the centre. The distance between the quarks, $d = d_1 - d_2$, increases from the top row through to the bottom row, taking values 0, 2, 4, 6 and 8 times the lattice spacing $a = 0.0907$ fm.

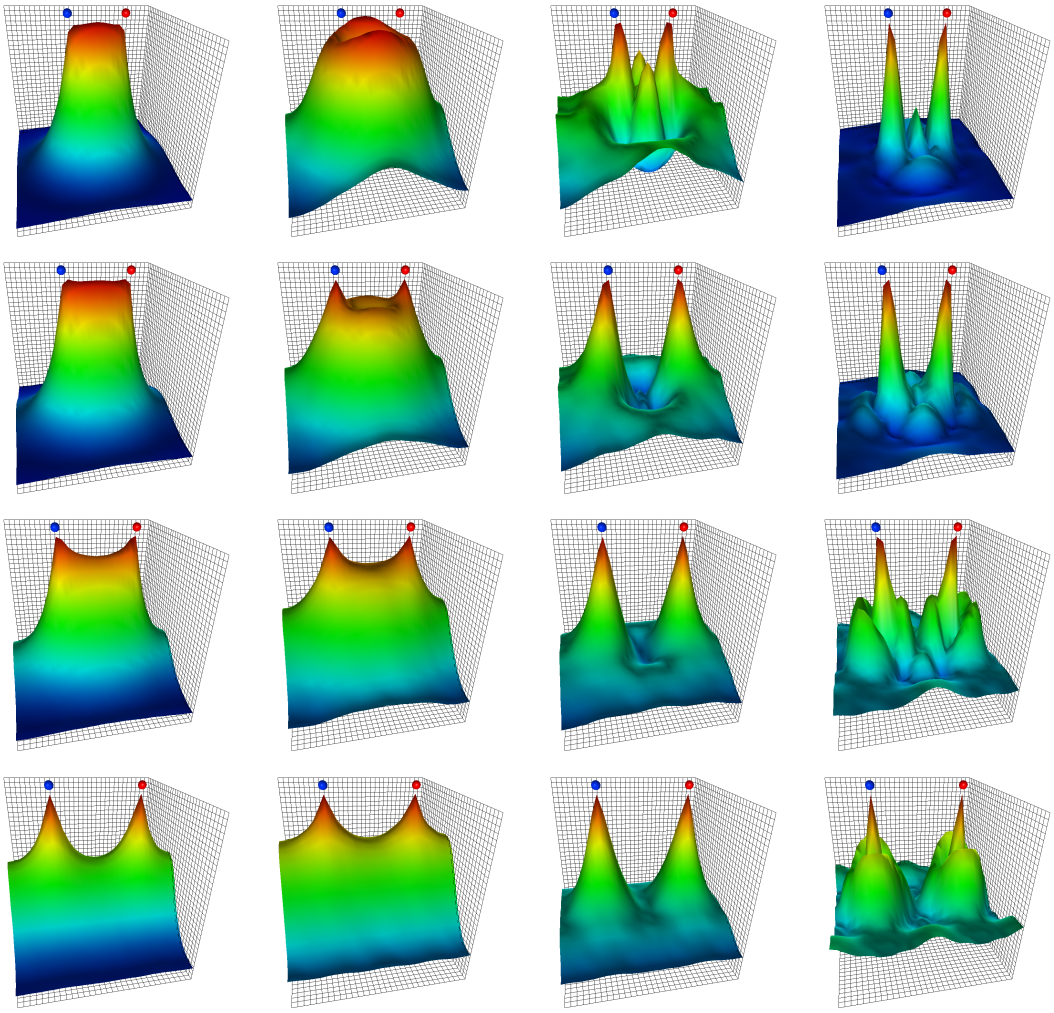

Figure 6.9: The dependence of the d-quark probability distribution on the positions of the u quarks in the proton and its excited states. From left to right, the columns correspond to the ground, first, second and third S-wave excitations. The u quarks are fixed on the x-axis running from back right through front left through the centre of the plot. The u quarks are fixed a distance of d_1 and $d_2 = -d_1$ from the origin located at the centre. The distance between the quarks, $d = d_1 - d_2$, increases from the top row through to the bottom row, taking values 10, 12, 14, and 16 times the lattice spacing $a = 0.0907$ fm.

First Excited-State Distribution

As the u quarks are separated in the first excited state associated with the Roper, the central peak of the d-quark distribution broadens in a manner similar to that for the ground state. However by $d = 4\,a = 0.36$ fm strength in the wave function is seen to move from the centre into the outer shell of the $2S$ state. This transition continues to $d = 10\,a = 0.91$ fm where the u quarks are still well inside the original node position of the $2S$ distribution. At this point, the central peak has been suppressed entirely leaving a hole inside the ring or shell in three dimensions. In other words, the node of the wave function has shrunk to the origin. It's interesting how the ring-like probability density is enhanced in the direction perpendicular to the separation of the u quarks.

At $d = 11\,a = 1.00$ fm, small peaks form in the probability distributions at the positions of the u quarks revealing the first onset of scalar diquark clustering similar to that in the second row of Fig. 6.9. At $d = 12\,a = 1.09$ fm, the u quarks are still within the node of the original wave function. but the radius of the outer shell of the wave function illustrated by the ring in the probability density has reduced slightly. At $d = 14\,a = 1.27$ fm, the u quarks sit in the node of the original wave function and there is little memory of the original $2S$ structure. Only a slight swelling at the centre of the distribution remains. The central probability density reduces at $d = 15\,a = 1.36$ fm such that scalar-diquark clustering dominates the probability distribution at $d = 16\,a = 1.45$ fm.

Second Excitation

For the second excited state observed herein, we again see a shift of the probability density from the central peak to the next shell of the original $3S$-like wave function. At $d = 6\,a = 0.54$ fm in the fourth row of Fig. 6.8, a similar enhancement in the first shell is observed as for the Roper at $d = 8\,a = 0.73$ fm with strength in the probability density enhanced in the direction perpendicular to the separation of the u quarks.

The radius of the first shell about the central peak of the original distribution shrinks as the u quarks are pulled apart and at $d = 8\,a = 0.73$ fm corresponding to the bottom row of Fig. 6.8, the u quarks are now in the first shell where four peaks are apparent. The original first node has shrunk to the centre and may have emerged, centered about each of the u quarks. Further evidence of this process

is discussed in the analysis of the third excitation below. The second node of the original wave function now surrounds the four peaks.

The u quarks approach the position of the second node of the wave function at $d = 10\,a = .91$ fm. The node is still apparent in the front and back of the distribution, orthogonal to the u-quark separation axis. The peaks in the probability distribution are still associated with the first shell surrounding the central peak of the original distribution with zero u-quark separation.

By $d = 12\,a = 1.09$ fm the quarks have moved beyond the second node. The radius of node has reduced and can be seen in the dark-blue regions at the centre of the plot. At $d = 13\,a = 1.18$ fm the second node has collapsed to the origin and explains the strong separation of the two peaks observed at $d = 14\,a = 1.27$ fm in the third row of Fig. 6.9. Even at the largest quark separations examined, the node structure of this state is apparent, suppressing the probability density between the two peaks once again governed by scalar-diquark dynamics.

Third Excitation

The third excitation displays a wonderfully complex structure that mirrors the transitions observed for the first and second excitations for the first few separations. For example at $d = 4\,a = 0.36$ fm, one can see the enhancement of the first shell in a direction orthogonal to the u quark separation axis.

At $d = 6\,a = 0.54$ fm, a four-peak structure emerges as the u quarks enter the first shell of the wave function. Remarkably, a new nodal structure has emerged. Upon shrinking to the origin, the original first node emerged surrounding each of the peaks at the u quark positions. This node now cuts through the first shell strength of the underlying $4S$ configuration and divides what would normally be a ring shape into four peaks.

By $d = 10\,a = 0.91$ fm the third node surrounds all significant structure in the distribution. The second node has shrunk to surround the small peak in the centre and the first surrounds the u quark peaks.

At $d = 12\,a = 1.09$ fm the third node now surrounds both of the major peaks and the fore and aft humps near the centre. The first node continues to surround each of the peaks at the u quark positions, The emergence of a second node around each of the u quarks is becoming apparent at the left- and right-hand edges of the plot.

At $d = 14\,a = 1.27$ fm the third node maintains a circular structure centred about the origin and cuts through the ring like structures forming around each of the u quarks. The rings clearly reveal the shifting of the first and second nodes to surround each of the u quarks.

At the largest u-quark separation of $d = 16\,a = 1.45$ fm the third node has shrunk further to just touch the inside edges of the rings which have formed though the first and second nodes shrinking to the origin and emerging around the two u quarks.

Chapter 7

Conclusion

In this thesis, we provide a comprehensive discussion of the lattice techniques required to explore the wave function of the proton, as well as its excited states in both quenched and $2+1$ flavour Lattice Quantum Chromodynamics. These techniques are then applied to calculate the proton wave function under an extensive set of conditions.

We develop a program of quantifying the effectiveness of smeared operators in coupling to specific states, in particular, high-momentum ground states. A detailed analysis of the ground state isolation shows that the two measures introduced are in good agreement with each other at all momenta studied. This analysis demonstrates that optimisation of the smearing sweeps alone can lead to significant improvement in the isolation of the ground state, particularly at high-momenta, where the ability of an operator to isolate the ground state is dramatically reduced only a few sweeps from the optimal number.

A method of altering the distribution of the smearing applied along a particular axis is developed, allowing the 'shape' of the source to more closely resemble that of a Lorentz contracted state. On applying this anisotropic smearing to high-momentum states, no appreciable improvement over standard smearing is found in the ability of an operator to couple to such a state. A small improvement in the relative error is observed using anisotropic smearing.

Our results indicate that this relatively cheap method of tuning the smearing parameters to optimise access to high-momentum states should be adopted by future studies of high-momentum states on the lattice. In particular, this approach could prove significantly beneficial in future form factor studies.

Wave functions of the proton from quenched QCD are examined in an external magnetic field, in both the Landau and Coulomb gauges. Interesting phenomena are observed even in the free field case. For example, the d quark wave function in the Landau gauge exhibits mild diquark clustering that is not apparent in the Coulomb gauge. In the case of the scalar u quark wave functions, clear clustering with the d quark is evident in both the Landau and Coulomb gauges. For the vector u quark in the proton interpolating field, clustering with the d quark is also evident, however, the wave function is not as tightly bound as either the scalar u quark or d quark wave function. Furthermore, the wave functions in the Coulomb gauge are consistently more localised than those in the Landau gauge.

When a constant magnetic field is applied to the proton, the wave function is shown to be dependent on the choice of vector potential, an unphysical effect. Gauge transformations are performed on the vector potential to rotate it by 90 degrees and reverse the direction in which it increases without changing the magnetic field. The wave function is then calculated for each vector potential and averaged over all four choices.

In spite of the very large magnetic field required by the quantisation conditions, the change in the probability distribution is found to be small, being most prominent in the vector u quark. The effect observed is the elongation of the distribution along the axis of the field while localising the distribution in the plane perpendicular to the field. The vector u quark exhibits the most spin dependence, with the probability distribution being more localized when the spin is aligned with the magnetic field. This effect can be understood in terms of a constituent quark model where the constituent quark mass increases in the presence of the magnetic field.

In spite of a small variation in the wave function of the proton, the mass changes as expected with the field strength, increasing or decreasing depending on the whether the spin is aligned or anti aligned with the field. These results show promise for the background field method, as there is little change to the structure of the proton in these large magnetic fields.

Wave functions at non-zero momentum are also calculated, and Lorentz contraction is qualitatively observed. When source smearing parameters are chosen by using the methods discussed in Chapter 5, we find a cleaner signal at higher momentum than with a non-optimised source, further demonstrating the effec-

tiveness of those techniques.

In this first study of the quark probability distribution within excited states of the nucleon, we show that all the states accessed in our correlation matrix analysis display the node structure associated with radial excitations of the quarks. For example the first excited state associated with the Roper resonance displays a node in the d quark wave function consistent with a radial excitation of the d quark. The second and third excitations display two and three nodes respectively.

On comparing these probability distributions to those predicted by the constituent quark model, we find good qualitative similarity with interesting differences. The core of the states is described very well by the model and the amplitudes of the S-wave shells between the nodes are predicted very accurately by the constituent quark model. The discovery of a node structure provides a deep understanding of the success of the smeared-source/sink correlation matrix methods of Ref. [45].

Finite volume effects are shown to be particularly significant for the excited states explored herein at relatively light quark mass. As these excited states have a multi-particle component, the interplay between the lattice volume, the wave function and the associated energy are key to extracting the resonance parameters of the states.

Fascinating structure in the d-quark probability distributions of the nucleon excited states is revealed when separating the u quarks from the origin. As the u quarks are separated the original node structure of the wave function shrinks in size. For example, the Roper reveals a ringed structure in the surface plots corresponding to an empty shell in three dimensions as the node collapses to the origin. The second excited state reveals a four-peaked structure at mid-range quark separations. At large separations these states all display diquark clustering with the d quark most likely found near one of the u quarks. The third state reveals the most exotic structure with new nodes centred about the u quarks appearing after the original nodes collapsed to the origin.

This thesis shows a distinct congruency between the wave functions of states on a lattice and some of the techniques widely used in Lattice QCD. Analysis of the wave function can serve as a vital tool for the determination of finite volume, relativistic and electromagnetic effects on hadrons. Future calculations will explore the structure of these states in more detail, examining the effect of the

introduction of isospin-1/2 spin-3/2 interpolating fields [85, 86] to reveal the role of D-wave contributions. While our use of improved actions suppresses lattice discretization errors, ultimately simulations will be done at a variety of lattice spacings directly at the physical quark masses. An analysis of finite volume effects will also be interesting to further reveal the interplay between the finite volume of the lattice, the structure of the states and the associated energy of the states; thus connecting the lattice QCD simulation results to the resonance physics of Nature.

Appendix A

Publications by the author

- W. Kamleh, D. B. Leinweber and D. S. Roberts, *Exploring the Roper wave function in Lattice QCD*, Prepared for The 31st International Symposium on Lattice Field Threory (Lattice 2013) arXiv:1312.2314 [hep-lat].
- D. S. Roberts, W. Kamleh and D. B. Leinweber, *Nucleon Excited State Wave Functions from Lattice QCD*, Phys. Rev. D **89**, 074501 (2014) [arXiv:1311.6626 [hep-lat]].
- D. Trewartha, W. Kamleh, D. Leinweber and D. S. Roberts, *Quark Propagation in the Instantons of Lattice QCD*, Phys. Rev. D **88**, 034501 (2013) [arXiv:1306.3283 [hep-lat]].
- D. S. Roberts, W. Kamleh and D. B. Leinweber, *Wave Function of the Roper from Lattice QCD*, Phys. Lett. **B725** 164 (2013) [arXiv:1304.0325 [hep-lat]].
- D. S. Roberts, W. Kamleh and D. B. Leinweber, *The wave function of the Roper resonance*, PoS LATTICE **2012**, 261 (2012).
- D. S. Roberts, W. Kamleh, D. B. Leinweber, M. S. Mahbub and B. J. Menadue, *Accessing High Momentum States In Lattice QCD*, Phys. Rev. D **86**, 074504 (2012) [arXiv:1206.5891 [hep-lat]].
- D. S. Roberts, P. O. Bowman, W. Kamleh and D. B. Leinweber, *Proton wave functions in a uniform magnetic field*, AIP Conf. Proc. **1354**, 224 (2011).

A. PUBLICATIONS BY THE AUTHOR

- D. S. Roberts, P. O. Bowman, W. Kamleh and D. B. Leinweber, *Wave function of the proton in a uniform magnetic field*, PoS LATTICE **2010**, 328 (2010).
- D. S. Roberts, P. O. Bowman, W. Kamleh and D. B. Leinweber, *Wave Functions of the Proton Ground State in the Presence of a Uniform Background Magnetic Field in Lattice QCD*, Phys. Rev. D **83**, 094504 (2011) [arXiv:1011.1975 [hep-lat]].
- D. S. Roberts, P. O. Bowman, W. Kamleh and D. B. Leinweber, *Shape of the proton in a uniform magnetic field*, AIP Conf. Proc. **1261**, 135 (2010).

References

[1] H. Rothe, World Sci.Lect.Notes Phys. **43**, 1 (1992). 10

[2] K. G. Wilson, Phys.Rev. **D10**, 2445 (1974). 11, 18

[3] R. Sommer, Nucl.Phys. **B411**, 839 (1994), [hep-lat/9310022]. 12, 60

[4] G. P. Lepage (1996), [hep-lat/9607076]. 12

[5] M. Luscher and P. Weisz, Commun.Math.Phys. **97**, 59 (1985). 12, 14, 60

[6] K. Symanzik, Nucl.Phys. **B226**, 187 (1983). 13

[7] K. Symanzik, Nucl.Phys. **B226**, 205 (1983). 13

[8] P. Weisz, Nucl.Phys. **B212**, 1 (1983). 13

[9] P. Weisz and R. Wohlert, Nucl.Phys. **B236**, 397 (1984). 13

[10] G. P. Lepage and P. B. Mackenzie, Phys.Rev. **D48**, 2250 (1993), [hep-lat/9209022]. 14

[11] Y. Iwasaki, Nucl.Phys. **B258**, 141 (1985). 15

[12] Y. Iwasaki (2011), [arXiv:1111.7054 [hep-lat]]. 15, 86

[13] S. Duane, A. Kennedy, B. Pendleton, and D. Roweth, Phys.Lett. **B195**, 216 (1987). 16

[14] H. B. Nielsen and M. Ninomiya, Phys.Lett. **B105**, 219 (1981). 17

[15] M. Luscher, S. Sint, R. Sommer, and P. Weisz, Nucl.Phys. **B478**, 365 (1996), [hep-lat/9605038]. 20

[16] B. Sheikholeslami and R. Wohlert, Nucl.Phys. **B259**, 572 (1985). 20, 44, 86

[17] M. Luscher and P. Weisz, Nucl.Phys. **B479**, 429 (1996), [hep-lat/9606016]. 22

[18] M. Luscher, S. Sint, R. Sommer, P. Weisz, and U. Wolff, Nucl.Phys. **B491**, 323 (1997), [hep-lat/9609035]. 22

[19] J. M. Zanotti *et al.* [CSSM Lattice Collaboration], Phys.Rev. **D65**, 074507 (2002), [hep-lat/0110216]. 22, 84

[20] J. Zanotti, S. O. Bilson-Thompson, F. Bonnet, P. Coddington, D. Leinweber, *et al.*, Nucl.Phys.Proc.Suppl. **109A**, 101 (2002), [hep-lat/0201004]. 22

[21] S. Gusken, Nucl.Phys.Proc.Suppl. **17**, 361 (1990). 23, 25, 43, 60, 86

[22] H. van der Vorst, SIAM J. Sc. Stat. Comp. **13**, 631 (1992). 23

[23] A. Frommer, V. Hannemann, B. Nockel, T. Lippert, and K. Schilling, Int.J.Mod.Phys. **C5**, 1073 (1994), [hep-lat/9404013]. 23

[24] M. Falcioni, M. Paciello, G. Parisi, and B. Taglienti, Nucl.Phys. **B251**, 624 (1985). 23, 41

[25] M. Albanese *et al.* [APE Collaboration], Phys.Lett. **B192**, 163 (1987). 23, 41

[26] C. Morningstar and M. J. Peardon, Phys.Rev. **D69**, 054501 (2004), [hep-lat/0311018]. 24, 60

[27] J. Smit and J. C. Vink, Nucl.Phys. **B286**, 485 (1987). 26, 59

[28] M. Burkardt, D. B. Leinweber, and X.-m. Jin, Phys.Lett. **B385**, 52 (1996), [hep-ph/9604450]. 26, 59

[29] H. Fiebig, W. Wilcox, and R. Woloshyn, Nucl.Phys. **B324**, 47 (1989). 26

[30] G. Martinelli, G. Parisi, R. Petronzio, and F. Rapuano, Phys.Lett. **B116**, 434 (1982). 29, 59

[31] C. W. Bernard, T. Draper, K. Olynyk, and M. Rushton, Phys.Rev.Lett. **49**, 1076 (1982). 29, 59

[32] F. Lee, R. Kelly, L. Zhou, and W. Wilcox, Phys.Lett. **B627**, 71 (2005), [hep-lat/0509067]. 29, 59, 67

[33] F. X. Lee, L. Zhou, W. Wilcox, and J. C. Christensen, Phys.Rev. **D73**, 034503 (2006), [hep-lat/0509065]. 29, 59

[34] R. Gupta, D. Daniel, and J. Grandy, Phys.Rev. **D48**, 3330 (1993), [hep-lat/9304009]. 29, 36, 59, 72, 83

[35] B. Velikson and D. Weingarten, Nucl.Phys. **B249**, 433 (1985). 29, 36, 59, 63

[36] M. Chu, M. Lissia, and J. W. Negele, Nucl.Phys. **B360**, 31 (1991). 29, 36, 59, 63, 83

[37] M. W. Hecht and T. A. DeGrand, Phys.Rev. **D46**, 2155 (1992). 29, 36, 59, 62, 65, 90, 99

[38] D. Leinweber, W. Melnitchouk, D. Richards, A. Williams, and J. Zanotti, Lect.Notes Phys. **663**, 71 (2005), [nucl-th/0406032]. 32, 33, 41, 84

[39] D. B. Leinweber, Phys.Rev. **D51**, 6383 (1995), [nucl-th/9406001]. 32, 84

[40] C. Michael, Nucl.Phys. **B259**, 58 (1985). 33, 41, 84

[41] M. Luscher and U. Wolff, Nucl.Phys. **B339**, 222 (1990). 33, 41, 84

[42] C. McNeile and C. Michael [UKQCD Collaboration], Phys.Rev. **D63**, 114503 (2001), [hep-lat/0010019]. 33, 41

[43] M. Mahbub, A. O. Cais, W. Kamleh, B. Lasscock, D. B. Leinweber, *et al.*, Phys.Rev. **D80**, 054507 (2009), [0905.3616]. 33, 35, 43, 44

[44] M. Mahbub, A. O. Cais, W. Kamleh, B. G. Lasscock, D. B. Leinweber, *et al.*, Phys.Lett. **B679**, 418 (2009), [0906.5433]. 33, 35, 41

[45] M. S. Mahbub, W. Kamleh, D. B. Leinweber, P. J. Moran, and A. G. Williams [CSSM Lattice collaboration], Phys.Lett. **B707**, 389 (2012), 7 pages, 5 figures. Revised version with new results to appear in PLB, [1011.5724]. 33, 35, 41, 84, 86, 95, 107

[46] E. Salpeter and H. Bethe, Phys.Rev. **84**, 1232 (1951). 35

[47] D. S. Roberts, P. O. Bowman, W. Kamleh, and D. B. Leinweber, Phys.Rev. **D83**, 094504 (2011), [1011.1975]. 36, 83, 99

[48] D. S. Roberts, W. Kamleh, and D. B. Leinweber (2013), [1304.0325]. 37, 83, 84, 87

[49] C. Davies, G. Batrouni, G. Katz, A. S. Kronfeld, G. Lepage, *et al.*, Phys.Rev. **D37**, 1581 (1988). 37, 40, 60, 87

[50] F. D. Bonnet, P. O. Bowman, D. B. Leinweber, A. G. Williams, and D. G. Richards, Austral.J.Phys. **52**, 939 (1999), [hep-lat/9905006]. 37, 38, 87

[51] G. Martinelli and C. T. Sachrajda, Nucl. Phys. **B306**, 865 (1988). 41

[52] T. Draper, R. Woloshyn, W. Wilcox, and K.-F. Liu, Nucl.Phys. **B318**, 319 (1989). 41

[53] G. Martinelli and C. T. Sachrajda, Nucl.Phys. **B316**, 355 (1989). 41

[54] T. Draper, R. Woloshyn, and K.-F. Liu, Phys.Lett. **B234**, 121 (1990). 41

[55] D. B. Leinweber, R. Woloshyn, and T. Draper, Phys.Rev. **D43**, 1659 (1991). 41, 87

[56] D. B. Leinweber, S. Boinepalli, I. Cloet, A. W. Thomas, A. G. Williams, *et al.*, Phys.Rev.Lett. **94**, 212001 (2005), [hep-lat/0406002]. 41

[57] S. Boinepalli, D. Leinweber, A. Williams, J. Zanotti, and J. Zhang, Phys.Rev. **D74**, 093005 (2006), [hep-lat/0604022]. 41

[58] C. Alexandrou, G. Koutsou, J. Negele, Y. Proestos, and A. Tsapalis, Phys.Rev. **D83**, 014501 (2011), [1011.3233]. 41

[59] C. Alexandrou *et al.* [ETM Collaboration], Phys.Rev. **D83**, 045010 (2011), [1012.0857]. 41

[60] C. Alexandrou, PoS **LATTICE2010**, 001 (2010), [1011.3660]. 41

[61] Y. Aoki, T. Blum, H.-W. Lin, S. Ohta, S. Sasaki, *et al.*, Phys.Rev. **D82**, 014501 (2010), [1003.3387]. 41

[62] T. Yamazaki, Y. Aoki, T. Blum, H.-W. Lin, S. Ohta, *et al.*, Phys.Rev. **D79**, 114505 (2009), [0904.2039]. 41

[63] S. Syritsyn, J. Bratt, M. Lin, H. Meyer, J. Negele, *et al.*, Phys.Rev. **D81**, 034507 (2010), [0907.4194]. 41

[64] J. M. Zanotti, PoS **LATTICE2008**, 007 (2008), [0812.3845]. 41

[65] H.-W. Lin, S. D. Cohen, R. G. Edwards, K. Orginos, and D. G. Richards (2010), [1005.0799]. 41, 42

[66] S. Aoki *et al.* [PACS-CS Collaboration], Phys.Rev. **D79**, 034503 (2009), [0807.1661]. 44, 84, 86

[67] Y. Iwasaki (1983). 44

[68] J. Zanotti, D. Leinweber, W. Melnitchouk, A. Williams, and J. Zhang, Lect.Notes Phys. **663**, 199 (2005), [hep-lat/0407039]. 60

[69] M. Anselmino, E. Predazzi, S. Ekelin, S. Fredriksson, and D. Lichtenberg, Rev.Mod.Phys. **65**, 1199 (1993). 65

[70] C. Alexandrou, P. de Forcrand, and B. Lucini, PoS **LAT2005**, 053 (2006), [hep-lat/0509113]. 65

[71] C. Alexandrou, P. de Forcrand, and B. Lucini, Phys.Rev.Lett. **97**, 222002 (2006), [hep-lat/0609004]. 65

[72] T. DeGrand, Z. Liu, and S. Schaefer, Phys.Rev. **D77**, 034505 (2008), [0712.0254]. 65

[73] L. D. Roper, Phys.Rev.Lett. **12**, 340 (1964). 83, 84

[74] C. Alexandrou and G. Koutsou, Phys.Rev. **D78**, 094506 (2008), [0809.2056]. 83

[75] A. De Rujula, H. Georgi, and S. Glashow, Phys.Rev. **D12**, 147 (1975). 84

[76] R. Bhaduri, L. Cohler, and Y. Nogami, Phys.Rev.Lett. **44**, 1369 (1980). 84, 90

[77] M. Gockeler *et al.* [QCDSF Collaboration, UKQCD Collaboration, LHPC Collaboration], Phys.Lett. **B532**, 63 (2002), [hep-lat/0106022]. 84

[78] S. Sasaki, T. Blum, and S. Ohta, Phys.Rev. **D65**, 074503 (2002), [hep-lat/0102010]. 84

[79] W. Melnitchouk, S. O. Bilson-Thompson, F. Bonnet, J. Hedditch, F. Lee, *et al.*, Phys.Rev. **D67**, 114506 (2003), [hep-lat/0202022]. 84

[80] F. Lee, S. Dong, T. Draper, I. Horvath, K. Liu, *et al.*, Nucl.Phys.Proc.Suppl. **119**, 296 (2003), [hep-lat/0208070]. 84

[81] S. Basak, R. Edwards, G. Fleming, K. Juge, A. Lichtl, *et al.*, Phys.Rev. **D76**, 074504 (2007), [0709.0008]. 84

[82] J. Bulava, R. Edwards, E. Engelson, B. Joo, H.-W. Lin, *et al.*, Phys.Rev. **D82**, 014507 (2010), [1004.5072]. 84

[83] M. Mahbub, W. Kamleh, D. Leinweber, P. Moran, and A. Williams, PoS **LATTICE2011**, 127 (2011). 84

[84] M. S. Mahbub, W. Kamleh, D. B. Leinweber, P. J. Moran, and A. G. Williams, Phys.Rev. **D87**, 094506 (2013), [1302.2987]. 84, 85, 95

[85] J. Zanotti *et al.* [CSSM Lattice collaboration], Phys.Rev. **D68**, 054506 (2003), [hep-lat/0304001]. 108

[86] S. Nozawa and D. Leinweber, Phys.Rev. **D42**, 3567 (1990). 108